HAL
open science

# interaction of atomic and molecular hydrogen with amorphous water ice surfaces mimicking interstellar dust.

Elie Matar

## To cite this version:

Elie Matar. interaction of atomic and molecular hydrogen with amorphous water ice surfaces mimicking interstellar dust.. Astrophysics [astro-ph]. Université de Cergy Pontoise, 2009. English. NNT : . tel-00438534

**HAL Id: tel-00438534**

**https://theses.hal.science/tel-00438534**

Submitted on 3 Dec 2009

**HAL** is a multi-disciplinary open access archive for the deposit and dissemination of scientific research documents, whether they are published or not. The documents may come from teaching and research institutions in France or abroad, or from public or private research centers.

L'archive ouverte pluridisciplinaire **HAL**, est destinée au dépôt et à la diffusion de documents scientifiques de niveau recherche, publiés ou non, émanant des établissements d'enseignement et de recherche français ou étrangers, des laboratoires publics ou privés.

LAMAp
Université de Cergy-Pontoise

LERMA
Observatoire de Paris-Meudon

Thesis

# Interaction of Atomic and Molecular Hydrogen on Amorphous Water Ice Surfaces Mimicking Interstellar Dust

Elie Matar

Presented and Defended on *October 22nd 2009*

to obtain the grade of Docteur en Sciences

*Speciality*

Laboratory Astrophysics & Astrochemistry

Members of the jury:

| | | | |
|---|---|---|---|
| President: | Mrs. | Evelyne Roueff | LUTh/Observatoire de Paris |
| Examiner: | Mr. | Philippe Parent | LCPMR/Paris VI |
| Referees: | Mrs. | Anne Lafosse | LCAM/Paris XI |
| | Mrs. | Helen-Jane Fraser | Strathclyde/Glasgow |
| Supervisors: | Mr. | Jean-Louis Lemaire | LERMA, Paris/Cergy |
| | Mr. | François Dulieu | LERMA, Paris/Cergy |

*The two most common elements in the Universe are hydrogen and stupidity...*

*Harlan Ellison*

---

*Two things are infinite: the Universe and human stupidity; and I am not sure about the Universe.*

*Albert Einstein*

# Thank you...

My first thoughts go to my parents, without whom I would have never been able to write these few lines at the beginning of my PhD thesis. You have sacrificed a lot for my sake because you believed in me and continued encouraging me where other people thought that I would fail. Mom and dad I love you.

I wish to thank professors François Dulieu and Jean-Louis Lemaire for their mentorship and patience with me during the course of these last three years. They have spent a lot of their time helping me with all the administrative work I had to go through - and believe me, there were plenty to be done - and teaching me how to be an experimentalist and an astrophysicist at the same time. Thank you for all the scientific knowledge you brought me in this magical field.

My gratitude also goes to all the members of my jury: Evelyne Roueff, for accepting to preside the jury, to my reporters, Anne Lafosse and Helen J. Fraser; as well as Philippe Parent my examiner. Your remarks and comments allowed me to, on one hand, to improve this manuscript, and on the other hand, to expand my work by orienting me towards new directions.

This thesis is above all the fruit of a team work since it is tightly connected to FORMOLISM. Many thanks to all the Cergy team members of the LERMA, those who left us and those who are still part of the team. I will remain indebted to you and to the staff of the University of Cergy-Pontoise whom I got to work with and learn from during the course of these three years. Thanks to all the informaticians, admins, technicians, cleaning staff... who improve our comfort and our working conditions (without us even noticing) just by a "swoosh" of their magic wand.

I am sorry I have decided not to have a baby during the last three years, but at least I read Harry Potter... twice.

Special thanks to my two Italian colleagues, Emanuele and Mario, for all the memorable times spent in the lab, around lunch or a cup of coffee that usually included short Italian lessons.

I will never forget the "Grand Danois" Lars and the "chitchats" we used to have about Mr and Mrs "Ux is a good system" and their daughter Lin. Thank you for introducing me to the PhD Comics and for your helpful discussions in the LaTeX field. Lars, without you, this manuscript would have been written using Microsoft Word!

I would also like to thank Jean-Hugues Fillion for his help during the first 3 months of internship, my initiation with the YAG Laser, even if I did not use it very much, and for all his constructive remarks. I would like to thank Anouchah Momeni for turning the time spent around a user's guide, a dismantled turbo pump or a quatrz tube from dull to fun time.

Thanks to Hakima for introducing me to the Berber culture, and thanks to Henda for introducing me to the large variety of tunisian sweets.

My Parisian friends, French and ERAMSUS! Thank you for the great times that we spent together, at "La Plage", the Champs de Mars, Trocadéro, squatting in somebody's place and everywhere else. Lahoucine, Wahid, Malik, Bruno, Davide, Eleonora, Lenka, Kamil, Hilde, Randi, Matthias, Alex, Ottavia, Alba, Audrey, Salah, Elise, ... (I can keep on going for ever), it was a great pleasure meeting you, knowing you, learning different things from each and every one of you and spending all these unforgettable moments with you.

To my "Lebanese-Lyonese" friends: Johnny and Elie, my favorite roomates ever; thank you for the excellent moments we used to spend, in front of the TV, around the guitar singing and for introducing me to South Park... I am still addicted! Rami, Charbel, Celine, Joyce, Bassel, Amine, Maher, the friars of the antonin order of Chaponost and all the others: thank you for the precious moments we spent together.

I would also like to thank my "Bkassinian" friends in Lebanon for making my very short vacations unforgettable and worth every second of them: Maher, Majed el MIR, Lallas, Chadzi, Poxy, Rony and Franco you're the best friends a person can have.

My SWYA 2008 friends: Gerrit the great, Joey the joyful, Eamon the irish, Teresa and Carmen the spanish "chicas" thank you for the various drinking games in Blankenberge and for offering me a place to stay in Amsterdam when I needed one. I'm still waiting for your visit.

To all those friends who asked me: "So, what exactly is it that you do? Does that mean Astrology? My zodiac sign is Scorpio, what can you tell me about it?" Thank you for giving me the opportunity to explain what astrophysics is, for letting me explain what "the interstellar medium" is and what does hydrogen have to do with it all. Thank you for pretending that you weren't bored, that what I was saying was extremely interesting and that you're yawning because you didn't get much sleep last night.

Most importantly, I would like to thank you Charline for your time, patience and presence by my side for the last two years. These were the most

difficult years I went through, thank you for being who you are and for being here when I needed you... even if I didn't quite deserve it. Thank you from the bottom of my heart.

And how can I forget the biggest tiger of Rouen and the Basse-Normandie, Elgar Cigare, the most adorable, intelligent and coward cat I have ever seen in my whole life. Thank you for waking me up very late at night and very early in the morning and thank you for using my head as a pillow.

To all the persons who accompanied me and walked by my side during these last three years and to all those that I have forgotten, I say: Thank you...

Finally, I wish to express my gratitude to my Heavenly Father for making this a dream come true.

# Contents

**Thank you...** **v**

**Contents** **ix**

**List of Figures** **xiii**

**List of Tables** **xv**

**1**

**1 The interstellar medium** **3**
1.1 Introduction . . . . . 3
1.2 The composition of the interstellar medium . . . . . 3
1.3 Interstellar dust . . . . . 6

**2 Molecular hydrogen** **13**
2.1 Introduction . . . . . 13
2.2 Detection of $H_2$ . . . . . 13
2.3 Formation of $H_2$ . . . . . 14
2.3.1 The $H_2$ molecule . . . . . 14
2.3.2 Gas phase formation . . . . . 14
2.3.3 Gas-grain reactions . . . . . 16
2.4 Processes leading to surface $H_2$ formation . . . . . 17
2.5 Previous studies . . . . . 21

**3 The FORMOLISM set-up** **27**
3.1 The UHV main chamber . . . . . 27
3.2 Sample holder and cryogenic system . . . . . 29
3.2.1 The cryostat . . . . . 29
3.2.2 Temperature measurement and control . . . . . 31
3.3 Water ice formation on the sample holder . . . . . 32
3.3.1 Water vapour diffuser . . . . . 32
3.3.2 Growth of the ice . . . . . 33
3.4 Quadrupole Mass Spectrometer (QMS) . . . . . 34
3.4.1 Working principle . . . . . 34
3.4.2 Integration and use of the QMS . . . . . 35

3.5 Cold atomic and molecular beams . . . . . 37
3.5.1 Microwave plasma dissociation . . . . . 38
3.5.2 Triply differential pumping system . . . . . 38
3.5.3 Flux calibration of the beams . . . . . 41
3.5.4 Cooling system of the first beam . . . . . 41
3.5.5 Calibrating the Lakeshore 332 controller . . . . . 43
3.5.6 Residual pressure deposition mode . . . . . 45
3.6 REMPI 2+1 ionisation . . . . . 45
3.6.1 REMPI ionisation . . . . . 46
3.6.2 REMPI spectra . . . . . 47
3.7 Recent modifications . . . . . 48

**4 TPD technique and growth of water 51**
4.1 TPD experiments . . . . . 51
4.1.1 Introduction . . . . . 51
4.1.2 Desorption and TPD from a unique energy . . . . . 52
4.1.3 Specificity of molecular hydrogen on amorphous ice . . 54
4.1.4 Importance for the sticking . . . . . 56
4.1.5 Importance for the mobility . . . . . 56
4.2 Water ice substrates . . . . . 58
4.2.1 Introduction . . . . . 58
4.2.2 Growth and porosity . . . . . 58
4.2.3 Volume density . . . . . 62
4.2.4 Condition of the surface . . . . . 63
4.2.5 Interaction with the gas phase . . . . . 64
4.2.6 Procedures for growing ASW ices . . . . . 65
4.2.7 Probing the morphology of the ice . . . . . 68
4.3 Conclusion . . . . . 68

**5 Sticking of atomic and molecular hydrogen on icy grains 71**
5.1 Introduction . . . . . 71
5.2 The sticking process . . . . . 71
5.3 Previous works . . . . . 72
5.3.1 Theoretical . . . . . 72
5.3.2 Experimental . . . . . 73
5.4 The experiment . . . . . 74
5.5 Variation of the sticking coefficient with the beam temperature 79
5.6 The model . . . . . 81
5.6.1 Framework and hypotheses . . . . . 81
5.6.2 The sticking coefficient $S(G, v)$ . . . . . 81
5.6.3 The final sticking coefficient . . . . . 82
5.6.4 Mass dependence of the sticking coefficient . . . . . 83
5.6.5 Comparison with experiment . . . . . 84
5.7 Fitting the experimental data . . . . . 85

5.7.1 Testing the model on the sticking probabilities of H and D atoms from Buch & Zhang (1991) . . . . . 87
5.7.2 Using Buch and Zhang data in our experimental results 88
5.7.3 Final remark . . . . . 89
5.8 Conclusions . . . . . 90
5.9 Perspectives . . . . . 91
5.9.1 Sticking coefficients of $D_2$ and $H_2$ on *p*-ASW films . . . 91
5.9.2 Sticking coefficients of D and H atoms on *p*-ASW films 93
5.9.3 Precision and uncertainty of the measurements . . . . . 94

**6 Mobility of cold hydrogen atoms on icy dust grains 97**
6.1 Introduction . . . . . 97
6.1.1 The context . . . . . 97
6.1.2 Previous works . . . . . 97
6.2 Experiments . . . . . 99
6.2.1 Procedures . . . . . 99
6.3 The model . . . . . 107
6.4 Discussions . . . . . 110
6.4.1 Is atomic hydrogen mobile on icy grains? . . . . . 110
6.4.2 Consequence of the $O_2$+D reaction efficiency on water formation . . . . . 113
6.5 Some perspectives . . . . . 114
6.5.1 Thermal hopping *versus* tunnelling effect . . . . . 114
6.5.2 Infrared spectroscopy . . . . . 114

**7 Formation of molecular hydrogen and energy partitioning 115**
7.1 Introduction . . . . . 115
7.1.1 The energy partitioning problem . . . . . 115
7.1.2 The detection problem . . . . . 116
7.2 The Experiments . . . . . 117
7.2.1 Introduction . . . . . 117
7.2.2 Bare *np*-ASW ice . . . . . 118
7.2.3 $D_2$ saturated *np*-ASW ice . . . . . 122
7.2.4 *p*-ASW ice . . . . . 123
7.3 Conclusions . . . . . 125
7.3.1 From the experiments . . . . . 125
7.3.2 Consequences for astrophysics . . . . . 125
7.3.3 Further ideas . . . . . 127

**8 Conclusion 129**

**Bibliography 133**

**A Publications 145**

**B Resumé français** **153**

# List of Figures


1.3.1 Extinction effect . . . . . 7
1.3.2 Dust extinction curve . . . . . 8
1.3.3 ISO-SWS spectrum in the mid-IR range of the protostar W33A 9

2.2.1 Diagram of electronic and rovibrational excitation states of $H_2$ 15
2.4.1 Chemisorption and physisorption . . . . . 18
2.4.2 Different processes leading to $H_2$ formation on grains . . . . . 19
2.5.1 Different results of similar experiments of HD formation on water ice surfaces . . . . . 24

3.0.1 The FORMOLISM set-up. . . . . 28
3.1.1 Composition of the residual gas in the chamber. . . . . 30
3.2.1 Diagram of the cryostat. . . . . 30
3.2.2 Time-Of-Flight (TOF) mass spectrometer. . . . . 31
3.4.1 Quadrupole mass spectrometer . . . . . 35
3.4.2 QMS in low position in front of the surface. . . . . 36
3.5.1 Atomic beams . . . . . 40
3.5.2 Calibration of the $O_2$ beam. . . . . 42
3.5.3 Diagram of a PID controller. . . . . 43
3.5.4 Calibration of the PID controller. . . . . 44
3.6.1 Source of molecular hydrogen . . . . . 47
3.6.2 REMPI spectrum for molecular deuterium . . . . . 49
3.6.3 Excitation diagram for $D_2$, v= 2 . . . . . 49

4.1.1 Typical desorption profiles of TPD of orders 0, 1 and 2. . . . . 53
4.1.2 Typical TPD of molecular hydrogen . . . . . 55
4.1.3 Desorbing $D_2$ molecules as a function of $D_2$ exposed dose . . . 57
4.2.1 $H_2O$ TPD, phase transition . . . . . 60
4.2.2 Ballistic deposition simulations of $H_2O$ porous ice . . . . . 61
4.2.3 Example of $H_2O$ deposition to grow *np*-ASW ice . . . . . 66
4.2.4 Example of $H_2O$ deposition to grow *p*-ASW ice . . . . . 66
4.2.5 $D_2$ TPD profiles to probe the ice–Annealing effect . . . . . 67

5.4.1 A scheme of the first beam line. . . . . 75
5.4.2 A typical sticking experiment. . . . . 76
5.4.3 King and Wells experiment. . . . . 77

5.5.1 King and Wells experiment for several beam temperatures. . . 79
5.5.2 Variation of the sticking coefficients of $D_2$ and $H_2$. . . . . 80
5.6.1 Mass and temperature dependence between $S_{H2}$ and $S_{D2}$ . . . 84
5.7.1 Fit of experimental data obtained for $\Phi(x) = e^{-x^2}$ . . . . . 86
5.7.2 Fit of experimental data obtained for $\Phi(x) = 1/(1 + x^4)$ . . . 86
5.7.3 Sticking coefficient for H and D atoms from Buch & Zhang (1991) . . . . . 87
5.7.4 Experimental results for $H_2$ and $D_2$ sticking probabilities . . . 88
5.9.1 Integrated area of $D_2$ TPD profiles on *p*- and *np*-ASW . . . . 92
5.9.2 Integrated area of $D_2$ TPD profiles on *p*-ASW after irradiation of $D_2$ and D+D . . . . . 93

6.2.1 $D_2$ TPD profiles to probe the ice . . . . . 100
6.2.2 TPD profiles of $D_2$ and $O_2$ . . . . . 101
6.2.3 Normalised $O_2$ TPD integrated areas following different D exposures . . . . . 102
6.2.4 Normalised $D_2$ TPD integrated areas following different D exposures . . . . . 103
6.2.5 Overlap of the $O_2$ and D beams on the surface . . . . . 105
6.2.6 Comparision between $O_2$ TPD areas at 10 K and 25 K . . . . 106
6.2.7 $O_2$ TPD integrated areas for $O_2$ deposited after different D exposures . . . . . 108
6.2.8 $D_2$ TPD integrated areas for $O_2$ deposited after different D exposures . . . . . 108
6.4.1 Langmuir rejection effect of D atoms on *p*-ASW ice . . . . . 111

7.1.1 Ionisation threshold of excited $D_2$ molecules formed on the surface . . . . . 117
7.2.1 Normalised total $D_2$ and excited $D_2$ signals monitored during D irradiation of *np*-ASW. . . . . 119
7.2.2 Excited $D_2$ signals monitored during D irradiation of *np*-ASW. 122
7.2.3 Normalised total $D_2$ and excited $D_2$ signals monitored during D irradiation of *p*-ASW. . . . . 124
7.3.1 Morphological transformation of ASW ice from *p*- to *np*-ASW 128

# List of Tables

1.2.1 List of interstellar and circumstellar molecules . . . . . 5
1.2.2 Physical properties of the different phases of the ISM . . . . . 6
1.3.1 Column densities of molecular ices detected in W33A . . . . . 10

3.5.1 Characteristics of the differential pumping. . . . . 39

4.2.1 Different phases of crystalline ice . . . . . 59
4.2.2 The different names of ASW ice phases . . . . . 64

5.3.1 Theoretical hydrogen sticking coefficient for several teams . . . 72
5.8.1 Comparison between our sticking values and those of Buch & Zhang (1991) . . . . . 91

6.4.1 Comparison between the H atom diffusion values of several teams . . . . . 112

# Introduction

The space between stars is not empty. It is constituted of an extremely dilute mixture of gas and dust: the interstellar medium (ISM).

The most abundant species in the ISM is hydrogen, forming 70% of matter by mass. It can be found mostly in its atomic form in diffuse clouds and molecular form in dense clouds. Hydrogen is by far the most important species in the Universe. It is the basic constituent of three of the four molecules essential to life: water ($H_2O$), methane ($CH_4$), amine ($NH_2$) and carbon monoxide (CO).

The chain of chemical reactions that occur both in the gas phase and at the gas-surface interface leads to the formation of interstellar molecules (i.e., formation of CO), even complex ones. This formation, however, requires the presence of $H_2$, necessary to initiate the entire active and complex interstellar chemistry.

On the other hand, it is well known that molecular hydrogen does not form in the gas phase due to the extreme physical conditions (low $n_H$ density, low temperature) of the interstellar medium, but needs a catalyst to dissipate its excess in energy. The formation of $H_2$ occurs by the encounter of two hydrogen atoms on the surface of interstellar dust grains.

The physico-chemical processes that lead to $H_2$, HD or $D_2$ formation can also play a role in the formation and hydrogenation/deuteration of other more complex organic molecules. So the grain surface chemistry coexists with the gas phase chemistry and, in certain cases, seems to be more efficient or even dominant. Thus, in order to understand the formation of molecular hydrogen and of other molecules at the gas-surface interface, it is crucial to study and understand the physico-chemical processes that rule this formation, in particular the adsorption, sticking and mobility of atomic hydrogen, as well as the formation and desorption of molecular hydrogen on the surface of interstellar dust grains.

At the LERMA-LAMAp we are able to study these processes using the experimental set-up FORMOLISM (FORmation of MOLecules in the Inter-Stellar Medium) on surfaces. These surfaces can be either dry bare surfaces made of carbonaceous (*e.g.*, graphite) or siliceous (*e.g.*, SiO) material or ice covered surfaces. This work deals with amorphous solid water ice surfaces similar to interstellar grains under conditions close to those existing in the dense clouds of the ISM.

This thesis is divided into 9 chapters grouped in 3 sections. In section I, I will present the general characteristics of the ISM and the processes that lead to $H_2$ formation. Section II is the experimental section, including a detailed description of FORMOLISM, the growth of the different types of solid water ices and the temperature programmed desorption (TPD) technique. Section III deals with the experiments and their interpretations I have achieved during my three years of Ph.D. The three main topics are (1) the sticking of molecular and atomic hydrogen, (2) the mobility of cold atomic hydrogen and (3) the formation and de-excitation of molecular hydrogen.

# Chapter 1

# The interstellar medium

## 1.1 Introduction

Our perception and comprehension of the space extending between the stars of our Galaxy and other galaxies have been subject to radical changes through the last 50 years. Around 1950, observations had shown the presence of gas mainly composed of atomic hydrogen in addition to some atoms and ions (Na, K, $Ca^+$, $Ti^+$, Fe, ...) (Flower, 2007). This space is not "empty" as was to be thought. It is made of a mix of ions, atoms and molecules in the gas phase (see molecules in table 1.2.1) and of microscopic dust grains. This space is called the interstellar medium (ISM) and is composed of several regions of very different physical conditions (temperature, density, ...). The presence of dust grains have been emphasized by the light extinction phenomenon. The dust grains in the dense molecular clouds prohibit the light emitted by stars to reach us. Since the last 50 years, the construction of new ground based and spatial telescopes, as well as the evolution of the technology of receivers and detectors have allowed up to now the detection of more than 120 different molecules in the various phases of ISM and CSM (circumstellar medium).

## 1.2 The composition of the interstellar medium

The interstellar medium is mainly composed, by mass, of 70% of atomic and molecular hydrogen, 28% of helium and ∼2% of heavy elements such as O, C, N, Si and Fe the main constituents of dust that only represents ∼1% of the total mass (Lequeux, 2005). These elements are injected into the ISM either by the winds of massive stars (red giants), or ejected by the explosion of the external layer of a dying star (planetary nebulae) or by the explosion of a supermassive star (supernovae). Multiple environments control the ISM, dividing it schematically into five phases showing different physico-

chemical properties, namely (1) the molecular medium, (2) the cold neutral medium (diffuse atomic medium), (3) the warm neutral medium, (4) the warm ionised medium and (5) the hot ionised medium (from Tielens (2005)). The characteristics of these different phases are summarised in table 1.2.2.

**The molecular ISM:** The molecular gas is found in dense and confined regions gravitationally bound. These "molecular" clouds mainly contain $H_2$ and CO[1]. Molecular clouds may span several hundreds of parsecs in size and reach masses of the order of $10^6$ $M_\odot$ (in the case of giant molecular clouds). It is in the center of such clouds that matter is condensing to form the dense cores, the first step in the stellar formation cycle.

**The cold neutral ISM:** This phase is also known as the cold HI diffuse clouds($\sim$100 K). It is found in regions which have a typical size of $\sim$10 parsecs and a density of $\sim$50 cm$^{-3}$ and can be detected by observing the neutral hydrogen emission lines (HI).

**The warm neutral ISM:** This phase is detected by observing the 21 cm hydrogen emission line that corresponds to the transition between two hyperfine sublevels of the fundamental state of HI. This phase is lying in a large part of the space surrounding the cold neutral clouds. It has a temperature of around 8000 K and a density of $\sim$0.5 cm$^{-3}$.

**The warm ionised ISM:** This phase contains diffuse ionised gas. It is mainly observed in nebulae by looking at recombination lines like H$\alpha$. It has a very low density ($\sim$0.1 cm$^{-3}$) and a temperature of the order of 8000 K.

**The hot ionised ISM:** Its existence was first suggested by Spitzer in 1956. This very hot medium (between $10^5$ K and $10^7$ K) of extremely low density ($10^{-3}$ cm$^{-3}$) is observed via the diffuse X-ray emissions and the absorption of highly ionised oxygen (OVI, OVII, OVIII) lines visible in the UV. High ionisations and very high temperatures are due to the strong winds associated to supernovae explosions.

This schematic picture of the ISM does not exclude the fact that few of them may simultaneously coexist in complex regions like star forming regions, shocked regions, photon dominated regions (PDRs), Herbig-Haro objects and disks...

[1]Molecular clouds are detected via several CO (and its isotopomers such as $^{13}$CO and C$^{18}$O) rotational transitions: $J = 1 - 0$ at 2.6 mm, $J = 2 - 1$ at 1.3 mm and $J = 3 - 2$ at 0.87 mm.

| 2 atoms | 3 atoms | 4 atoms | 5 atoms | 6 atoms | 7 atoms | 8 atoms | 9 atoms | 10 atoms | 11 atoms | 12 atoms | 13 atoms |
|---|---|---|---|---|---|---|---|---|---|---|---|
| $H_2$ | $C_3$ | c-$C_3H$ | $C_5$ | $C_5H$ | $C_6H$ | $CH_3C_3N$ | $CH_3C_4H$ | $CH_3C_5N$ | $HC_9N$ | $C_6H_6$ ? | $HC_{11}N$ |
| AlF | $C_2H$ | l-$C_3H$ | $C_4H$ | l-$H_2C_4$ | $CH_2CHCN$ | $HC(O)OCH_3$ | $CH_3CH_2CN$ | $(CH_3)_2CO$ | $CH_3C_6H$ | $C_2H_5OCH_3$ ? | |
| AlCl | $C_2O$ | $C_3N$ | $C_4Si$ | $C_2H_4$ | $CH_3C_2H$ | $CH_3COOH$ | $(CH_3)_2O$ | $(CH_2OH)_2$ | $C_2H_5OCHO$ | $n$-$C_3H_7CN$ | |
| $C_2$** | $C_2S$ | $C_3O$ | l-$C_3H_2$ | $CH_3CN$ | $HC_5N$ | $C_7H$ | $CH_3CH_2OH$ | $CH_3CH_2CHO$ | | | |
| CH | $CH_2$ | $C_3S$ | c-$C_3H_2$ | $CH_3NC$ | $CH_3CHO$ | $H_2C_6$ | $HC_7N$ | $CH_3C_5N$ | | | |
| $CH^+$ | HCN | $C_2H_2$ ? | $H_2CCN$ | $CH_3OH$ | $CH_3NH_2$ | $CH_2OHCHO$ | $C_8H$ | $(CH_3)_2CO$ | | | |
| CN | HCO | $NH_3$ | $CH_4$ | $CH_3SH$ | c-$C_2H_4O$ | l-$HC_6H$ ? | $CH_3C(O)NH_2$ | $(CH_2OH)_2$ | | | |
| CO | $HCO^+$ | HCCN | $HC_3N$ | $HC_3NH^+$ | $H_2CCHOH$ | $CH_2CHCHO$? | $C_8H^-$ | | | | |
| $CO^+$ | $HCS^+$ | $HCNH^+$ | $HC_2NC$ | $HC_2CHO$ | $C_6H^-$ | $CH_2CCHCN$ | $C_3H_6$ | | | | |
| CP | $HOC^+$ | HNCO | HCOOH | $NH_2CHO$ | | $H_2NCH_2CN$ | | | | | |
| SiC | $H_2O$ | HNCS | $H_2CNH$ | $C_5N$ | | | | | | | |
| HCl | $H_2S$ | $HOCO^+$ | $H_2C_2O$ | l-$HC_4H$ ? | | | | | | | |
| KCl | HNC | $H_2CO$ | $H_2NCN$ | l-$HC_4N$ | | | | | | | |
| NH | HNO | $H_2CN$ | $HNC_3$ | c-$H_2C_3O$ | | | | | | | |
| NO | MgCN | $H_2CS$ | $SiH_4$ | $H_2CCNH$ ? | | | | | | | |
| NS | MgNC | $H_3O^+$ | $H_2COH^+$ | $C_5N^-$ | | | | | | | |
| NaCl | $N_2H^+$ | c-$SiC_3$ | $C_4H^-$ | | | | | | | | |
| OH | $N_2O$ | CH3 | HC(O)CN | | | | | | | | |
| PN | NaCN | C3N- | | | | | | | | | |
| SO | OCS | $PH_3$ ? | | | | | | | | | |
| $SO^+$ | $SO_2$ | HCNO | | | | | | | | | |
| SiN | c-$SiC_2$ | HOCN ? | | | | | | | | | |
| SiO | $CO_2$ | | | | | | | | | | |
| SiS | $NH_2$ | | | | | | | | | | |
| CS | $H3^+$ | | | | | | | | | | |
| HF | $H_2D^+$,$HD_2^+$ | | | | | | | | | | |
| SH | SiCN | | | | | | | | | | |
| HD | AlNC | | | | | | | | | | |
| FeO ? | SiNC | | | | | | | | | | |
| $O_2$ | HCP | | | | | | | | | | |
| $CF^+$ | | | | | | | | | | | |
| SiH ? | | | | | | | | | | | |
| PO | | | | | | | | | | | |
| AlO | | | | | | | | | | | |

*Table 1.2.1: List of the interstellar and circumstellar molecules observed untill the year 2009. In red are molecules that have been detected by their ro-vibration spectrum, (*) denotes those that have been detected by electronic spectroscopy and (?) denotes tentative detections that have a reasonable chance to be correct but remain uncertain. From http://www.astro.uni-koeln.de/cdms/molecules.*

| Medium | $n$ ( cm$^{-3}$) | T (K) | $M$ ($10^9$ M$_\odot$) | Main tracers |
|---|---|---|---|---|
| Molecular | $10^2 - 10^6$ | 10 | 1.3 | CO |
| Cold neutral | 50 | 80 | 2.2 | HI absorption |
| Warm neutral | 0.5 | 8000 | 2.8 | HI emission |
| Cold ionised | 0.1 | 8000 | 1.0 | HI, H$\alpha$ |
| Hot ionised | $10^{-3}$ | $10^6$ | – | X, UV rays |

*Table 1.2.2: Physical properties of the different phases of the Galactic ISM (Tielens, 2005).*

## 1.3 Interstellar dust

Dust is present everywhere in the interstellar medium. It was first discovered by William Herschel around 1784 as he noted its existence by observing regions in the night sky deprived of stars. Gradually, various observations showed that these dark regions of the interstellar medium are composed of dust grains of microscopic sizes, varying from a few nanometers to $\sim$1 $\mu$m (Williams & Herbst, 2002). The presence of dust is brought out by the observation of its different effects on starlight (Draine, 2003):

• **Extinction or reddening:** Dust grains absorb photons and diffuse them in directions other than that of the line of sight. The absorption and diffusion, put together, form what we call the visual "extinction" ($A_V$), and is closely linked to the chemical composition, form, size of dust particles and to the inverse of the wavelength (fig. 1.3.2). Since blue light is more strongly diffused and then attenuated than red light in the optical wavelength regions, interstellar extinction is often referred to as "reddening" (fig. 1.3.1).

• **Absorption and emission bands:** Interstellar dust appears to be opaque and obscure in the visible, but absorbs and emits in the near and far infrared as well as in the UV (fig. 1.3.2).

• **Polarization:** Light reaching us from reddened stars is often linearly polarised. This polarisation may arise from differential extinction by non-spherical dust grains partially aligned in the interstellar magnetic field.

• **Depletion** is a flaw in the abundance of certain chemical elements in the gas phase revealing a condensation into the solid phase.

At first, dust was believed to be composed of metals, a hypothesis that was ruled out afterward by observing that the abundance of metals was highly insufficient. Observations of absorption and emission lines helped distinguishing four different types of dust:

• **Aromatic hydrocarbons:** they consist of carbonaceous compounds that present aromatic cycles and $\pi$ bonds. They are detected via the depletion of carbon, the aromatic emission bands (C-H and C-C modes linked to an aromatic nuclei), the extinction in the UV range, and more particularly the

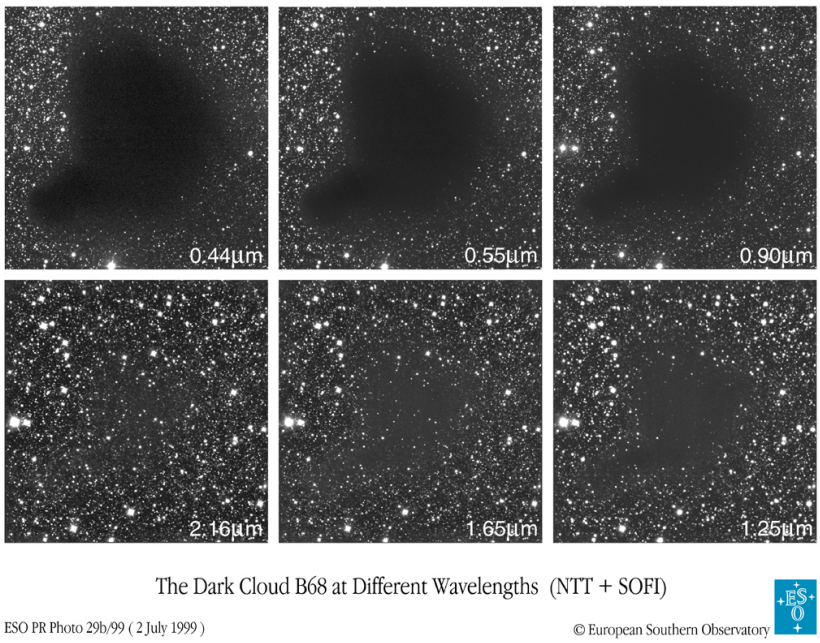


*Figure 1.3.1: The sky area of the globule Barnard 68, imaged in six different wavebands, clockwise from the blue to the near-infrared spectral region. It is evident that the obscuration caused by the cloud diminishes dramatically with increasing wavelength. Since the outer regions of the cloud are less dense than the inner ones, the apparent size of the cloud also decreases, as more background stars shine through the outer parts. ESO PR photo 29b/99 (1999).*

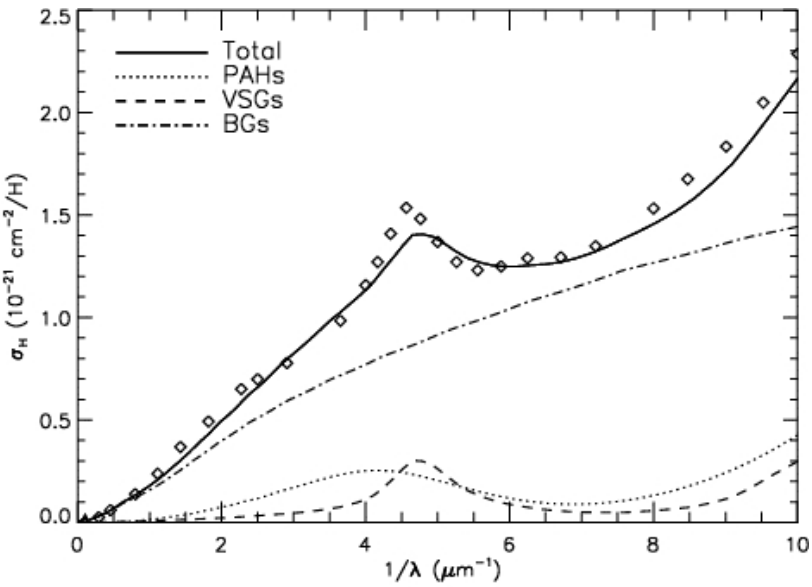


*Figure 1.3.2: Dust extinction curve and the contribution of the different possible constituants of interstellar dust grains. PAHs: Polycyclic Aromatic Hydrocarbons (size ranges 0.4–1.2 nm), VSGs: Very small (carbonaceous) grains (1.2–15 nm) and BGs: Big (silicates) grains (15–110 nm). (Compiègne et al., 2008)*

extinction excess at 2175 Å indicating the presence of graphitic materials. These compounds form small grains, the smallest being molecules of $\sim$ 10-1000 carbon atoms, comprising aromatic cycles, called PAH (Polycyclic Aromatic Hydrocarbons).

• **Hydrogenated amorphous carbon:** It contains saturated and non-saturated aliphatic chains, that can be bound to produce a solid macromolecular phase. It is characterized by the extinction bands attributed to C-H bonds (IR absorption at 3.4 $\mu$m) and by the depletion of carbon.

• **Silicates and metallic oxides:** They are essentially composed of Si, O, Mg and Fe that appear by depletion. They are refractory materials of mainly amorphous nature in the ISM. Crystalline grains are also present in the circumstellar environments and in the ejecta of supernovae. They are also detected via extinction bands, in particular that attributed to SiO. They might present magnetic inclusions and have non-spherical shapes indicated by their effects on the polarization of light in the visible and the IR ranges.

• **Ices:** They are present as mantles on the carbonaceous or silicate grains described above in cold and dense regions of the ISM. They are composed of molecular species that are condensed and/or form on the surface of the grains ($H_2O$, CO, $CO_2$, $CH_4$, $CH_3OH$, $NH_3$...). Several absorption bands in the IR range characteristic of incorporated molecules certify their amorphous nature, like for example the IR spectra of W33A observed by ISO-SWS

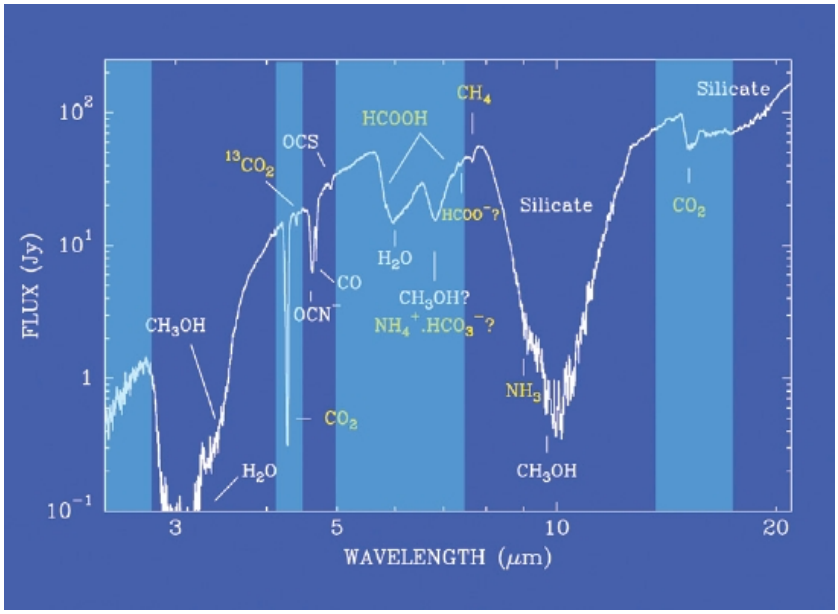


*Figure 1.3.3: ISOSWS spectrum of the deeply embedded massive YSO W 33A. Various absorption features due to silicate grain cores and icy mantles are indicated. Regions which cannot be observed from the ground are shaded. (from van Dishoeck et al., 2003)*

(fig. 1.3.3, van Dishoeck et al. (2003)). The column densities derived from these observations are shown in table 1.3.1. $H_2O$ is the most abundant constituant of interstellar ices.

The interstellar grains have a life cycle linked to that of the stars. Bare grains are formed in the atmospheres of evolved stars. We therefore detect the different consituents in crystalline form (Molster et al., 1999), like olivine and pyroxene (Mg- and Fe-rich silicates), and even diamond. These materials evolve during their stay in the ISM by different processes: photolysis, sputtering, coagulation,... due to shockwaves (supernovae explosions or star formation), collisions (turbulence), cosmic and UV rays. This results in the predominance of the amorphous phase, with a distribution of grains sizes typically of 5 nm to 0.5 $\mu$m (Draine, 2003) and where the biggest ones, formed by aggregation, have a porous nature (Jones, 2001).

Grains play an important role in the dynamics of the ISM, by shading it from stars light and heating it by photoelectric effect. They are also catalysts for chemical reactions, especially that of $H_2$, whose formation cannot be explained without the presence of the grains.

In molecular clouds, the ice mantles are exposed to the surrounding gas, composed of atoms and molecules (mainly H and $H_2$). The grain surface is therefore the birthplace of a heterogeneous chemistry, allowing the formation of new species. Cosmic ray or UV irradiations can contribute to enrich and

W33A Spectral Features

| $\lambda$ ($\mu$m) | FWHM ($cm^{-1}$) | $\tau$ | Species | $N$ ($10^{17}$ $cm^{-2}$) | $N/N(H_2O)$ *100 | Reference |
|---|---|---|---|---|---|---|
| 3.0 | 335 | 5.5(1.5) | $H_2O$ | 110(30) | 100 | 1 |
| 3.477 | 80.7 | 0.290(0.040) | HAC | ... | ... | 2 |
| 3.53 | 29 | 0.27(0.05) | $CH_3OH$(pure) | 11.9(2.2) | 10.8(2.0) | 2 |
| | 29 | 0.07(0.02) | Polar | 2.7(0.8) | 2.5(0.7) | 2 |
| 3.95 | 115.3 | 0.5 | $CH_3OH$ | 18.5 | 16.8 | 3 |
| 4.27 | 20 | >5 | $CO_2$ | 14.5(1.3) | 13.2(1.2) | 4 |
| | | | (Polar) | 12.3 | 11.2 | 4 |
| | | | (Nonpolar) | 2.2 | 2.0 | 4 |
| 4.38 | 9.5 | 0.225(0.015) | $^{13}CO_2$ | 0.274(0.021) | 0.249(0.019) | 5 |
| 4.5 | 700 | 0.1(0.05) | $H_2O$ | 70(40) | 64(36) | 1 |
| 4.62 | 24.7 | 1.3 | XCN | 6.9 | 6.3 | 6, 7 |
| 4.67 | 7.64 | 1.30(0.05) | CO | 8.9(0.5) | 8.1(0.5) | 8 |
| | | 0.68(0.05) | (Polar) | 6.6(0.5) | 6.0(0.5) | 8 |
| | | 0.79(0.05) | (Nonpolar) | 2.3(0.2) | 2.1(0.2) | 8 |
| 4.78 | 15 | <0.02 | $^{13}CO$ | <0.25 | <0.23 | 9 |
| 4.91 | 23 | 0.14 | OCS | 0.2 | 0.2 | 10 |
| 5.81 | 21 | 0.14(0.07) | $H_2CO$ | 3.45(1.7) | 3.1(1.6) | 9 |
| 5.85 | 65 | 0.32(0.07) | HCOOH | 4.12(0.9) | 3.7(0.8) | 9 |
| 6.02 | 172 | 0.49(0.07) | $H_2O$ | 110 | 100 | 11 |
| 6.0 | 420 | 1.12(0.07) | Organic residue | ... | ... | 11 |
| 6.2 | 60 | 0.22(0.07) | PAH? | ? | ? | 11 |
| 6.85 | 79 | 1.07(0.07) | Organics/$NH_4^+$ | ... | ... | 11 |
| 7.243 | 19 | 0.10(0.02) | HCOOH | 7.8 | 7.1 | 12 |
| | | | $HCONH_2$ | 6.3 | 5.7 | 12 |
| 7.414 | 15 | 0.10(0.03) | $HCOO^-$ | 0.93 | 0.85 | 12 |
| | | | $CH_3HCO$ | 10.8 | 9.82 | 12 |
| 7.631 | 27.7 | 0.082(0.005) | $SO_2$ | 1.74(0.90) | 1.58(0.82) | 13 |
| 7.676 | 10.4 | 0.120(0.005) | $CH_4$ | 1.7(0.2) | 1.5(0.2) | 13 |
| 8.90 | 34 | 0.1 | $CH_3OH$ | 15 | 14 | 1 |
| 9.0 | 68 | 0.45(0.10) | $NH_3$ | 17(4) | 15(4) | 1 |
| 9.7 | 295 | 7.84(0.12) | Silicate | ... | ... | 14 |
| 9.75 | 30 | 0.9(0.2) | $CH_3OH$ | 15(4) | 14(4) | 1 |
| 13.3[a] | 240 | [1.2] | $H_2O$ | [110] | [100] | 9 |
| 15.24 | 27.4 | 0.58(0.01) | $CO_2$ | 14.5(1.3) | 13.2(1.2) | 4 |
| | | | (Polar) | 12.3 | 11.2 | 4 |
| | | | (Nonpolar) | 2.2 | 2.0 | 4 |
| 18 | 200 | 1.20(0.02) | Silicate | ... | ... | 9 |

*Table 1.3.1: Column densities of molecular ices detected in W33A (Gibb et al., 2004). Emission features are present at 3.8195 $\mu$m ($H_I$ 166), 3.9075 $\mu$m ($H_I$ 155), and 4.0523 $\mu$m (Br$\alpha$).*

[a] *Calculated based on 3 $\mu$m feature.*

*References. (1) Gibb et al. (2000); (2) Brooke et al. (1999); (3) Dartois et al. (1999); (4) Gerakines et al. (1999); (5) Boogert et al. (2000); (6) Whittet et al. (2001); (7) Demyk et al. (1998); (8) Chiar et al. (1998); (9) Gibb et al. (2004); (10) Palumbo et al. (1997); (11) Gibb & Whittet (2002); (12) Schutte et al. (1999); (13) Boogert et al. (1996); (14) Willner et al. (1982).*

complexify this content by inducing additional chemical reactions. The new molecular species are then released into the gas phase during the heating of the ice mantle when stars are forming. The role of this heterogeneous chemistry on the surface of dust grains is therefore primordial to explain the chemical composition of the ISM.

# Chapter 2

# Molecular hydrogen

## 2.1 Introduction

Other than being the chief constituent of cold interstellar clouds, molecular hydrogen is by far the most important species in the interstellar medium since it is a key intermediary in the hydrogenation and formation of most gas phase species. It is an important coolant of molecular gas that has been heated to temperatures of a few hundred degrees or more by events such as the passage of a shock wave or excited by the strong UV radiation of a nascent star in photon dominated regions (PDRs). Even when partially dissociated, at temperatures of the order of 1000 K, $H_2$ may still dominate the cooling, owing to the high intrinsic elemental abundance of hydrogen (Flower, 2007).

At temperatures $\leq$30 K, on the other hand, molecular hydrogen is considered to be mostly a heating agent of the medium by means of two processes: photodissociation and formation. After the photodissociation of an $H_2$ molecule, the fragments will carry away some of the photon energy as a kinetic energy, heating the gas. After (re)formation of an $H_2$ molecule, the newly formed species may be left in a rovibrationally excited state. It may de-excite by losing a certain amount of its excess energy in the dust grain. In both cases, collisional de-excitation can then heat the gas. If rovibrationally excited $H_2$ radiates in the IR, then it contributes to the cooling of the medium.

## 2.2 Detection of $H_2$

Molecular hydrogen is among the most difficult molecules to detect. Even the lowest excited energy levels, those corresponding to molecular rotation, are too far above the ground state (near infrared) to be easily populated (the first $v" = 0$–$J" = 0$ level is lying at 60 cm$^{-1}$ (Silvera, 1980)). In addition, $H_2$ consists of two identical hydrogen atoms and therefore lacks a permanent electric dipole moment. A rotationally excited molecule must then radiate through a so called forbidden quadrupole transition.

Cold $H_2$ at T≤30 K, maps the molecular clouds in galaxies but remains difficult to observe, being detectable only by means of ultraviolet electronic absorption lines in the Lyman and Werner ($B^1\Sigma_u^+ - C^1\Pi_u$) bands from above the earth's atmosphere. Furthermore, a background continuum ultraviolet source, such as a hot star, is necessary for such observations. As scattering and absorption by dust are pronounced at short wavelengths (absorption of 95% of radiation), such observations are limited by the extinction along the line of sight through the molecular cloud towards the star.

Molecular hydrogen was first detected in absorption in the UV part of the spectrum, through the $X^1\Sigma_g^+ - B^1\Sigma_u^+$ (Lyman) or $C^1\Pi_u$ (Werner) electronic bands (transitions towards the other states need photons of energy >13.6 eV) by means of a sounding rocket (Carruthers, 1970). It has since been observed at much higher spectral resolution by the Copernicus (Spitzer et al., 1973) and the FUSE (Shull et al., 2000) satellites. $H_2$ has also been observed in the far infrared by the ISO satellite by detecting transitions in the electronic ground state between different rovibrational excitations[1], and through atmospheric windows in the near infrared, the most intense are mainly observed in the $K$-band [1-0 S(0, 1, 2 & 3), 1.957 to 2.223 $\mu$m]. Thus, electronic and rovibrational transitions of $H_2$ have all been observed in the interstellar medium.

The collisions generated by the shock waves or the turbulence of the medium can participate to the rovibrational excitation (and the de-excitation) of hydrogen molecules.

## 2.3 Formation of $H_2$

### 2.3.1 The $H_2$ molecule

Hydrogen exists predominantly in its 1s ground state, and collisions between hydrogen atoms can proceed along either of the two potential energy curves (fig. 2.2.1), in which the electronic spins are either parallel (triplet state) or anti-parallel (singlet state). As the individual electronic orbital angular momenta are zero, the resultant angular momentum $l$ and its projection $m_l$ on the internuclear axis of the quasi-molecule are also zero; the corresponding molecular states are denoted $^3\sum$ (repulsive state) and $^1\sum$ (attractive state).

### 2.3.2 Gas phase formation

After the recombination of two hydrogen atoms, the newly formed molecule must lose energy in order to stabilize. In the gas phase, as long as the density and temperature are high enough, this is possible by means of

[1]These quadrupole transitions have a very low probability and are therefore only observable due to the high abundance of $H_2$ on the line of sight of observations.

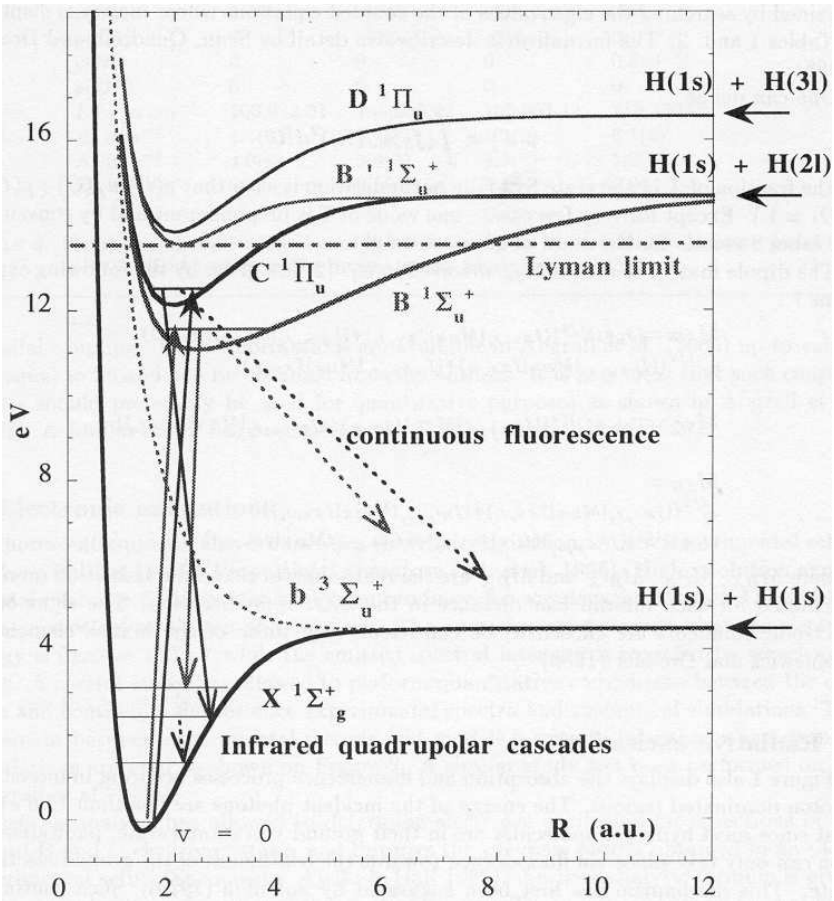


*Figure 2.2.1: Diagram of electronic and rovibrational exitation states of $H_2$ (Roueff et al., 2000). Two transitions correspond to an electronic excitation by UV towards the levels B and C are shown, as well as the de-excitation channels from these levels via UV and IR emission to the ground level. Two possible dissociation channels are also represented (dashed arrows)*

two processes:

**Radiative association of two hydrogen atoms**, via two different reactions

$$\mathrm{H} + \mathrm{e}^- \rightarrow \mathrm{H}^- + h\nu \tag{2.1}$$

$$\mathrm{H}^- + \mathrm{H} \rightarrow \mathrm{H}_2 + \mathrm{e}^- \tag{2.2}$$

(Field, 2000), and

$$\mathrm{H} + \mathrm{H}^+ \rightarrow \mathrm{H_2}^+ + h\nu \tag{2.3}$$

$$\mathrm{H_2}^+ + \mathrm{H} \rightarrow \mathrm{H}_2 + \mathrm{H}^+ \tag{2.4}$$

(Stahler & Palla, 2004).

The formation of molecular hydrogen may have occured by these reactions in the early Universe, before dust grains were formed.

**Three-body collisions**, via the formation reactions

$$\mathrm{H} + \mathrm{H} + \mathrm{H} \rightarrow \mathrm{H}_2 + \mathrm{H} \tag{2.5}$$

$$\mathrm{H} + \mathrm{H} + \mathrm{H}_2 \rightarrow 2\mathrm{H}_2 \tag{2.6}$$

(Field, 2000), where the third body allows the evacuation of the excess energy. However, three-body processes are very improbable at interstellar densities since they need a density $n_H > 10^8$ cm$^{-3}$ to be efficient (Palla et al., 1983).

### 2.3.3 Gas-grain reactions

The contribution of the different formation routes occurring in the gas phase do not explain the observed abundances of molecular hydrogen in the interstellar medium. An alternative and still the only efficient route for $H_2$ formation in interstellar clouds is through gas-grain reactions (Hollenbach & Salpeter, 1971). The interstellar dust grain acts as a catalyst, playing the role of the third body in a three-body reaction:

$$\mathrm{H} + \mathrm{H} + grain \rightarrow \mathrm{H}_2 + grain + 4.48\ eV. \tag{2.7}$$

Early estimates of the rate of $H_2$ formation on the grain (Hollenbach & Salpeter, 1971) suggested that most of hydrogen would be expected to be in its molecular form in dense molecular clouds[2].

The total formation rate of $H_2$ per unit volume can be expressed as:

$$\left.\frac{dn_{\mathrm{H}_2}}{dt}\right|_{form} = R_f n_H = \frac{1}{2}\sigma v_H \times \mathcal{R} \times n_H\ s^{-1} \tag{2.8}$$

[2]In dense quiescent clouds, $n_H$ is about $10^3$ cm$^{-3}$, The grain size is typically $\sim 0.1\ \mu$m and $T_{grain}$=$T_{gas}$=10 K.

where $\sigma v_H$ is the atom-grain collision frequency, typically 2 $10^{-16}$ $cm^3s^{-1}$, given by the product of the collision cross-section $\sigma$ and the mean velocity of hydrogen atoms $v_H$. $n_H$ is the atom density in the medium and $\mathcal{R}$ is the formation efficiency, often equal to

$$\mathcal{R} = SR \tag{2.9}$$

where $S(T, T_S)$ is the sticking probability of an atom with temperature T colliding with the grain surface of temperature $T_S$, and $R$ the probability that an atom encounters another one to form an $H_2$ molecule[3].

Observations allow us to obtain a constraint on the formation rate of molecular hydrogen. In diffuse clouds, the very efficient photodissociation of $H_2$ imposes a formation rate $R_f = 3\ 10^{-17}$ $cm^3s^{-1}$ (Jura, 1975), deducing a formation efficiency $\mathcal{R} = 0.3$. The same formation efficiency is found in molecular clouds, where $H_2$ is the most abundant and is photodissociated by cosmic rays. This is imposed by the low density of H atoms.

## 2.4 Processes leading to surface $H_2$ formation

**The adsorption process:** Adsorption is the process by which a gas phase species becomes trapped on a surface. There are two kinds of adsorption: physical adsorption or physisorption and chemical adsorption or chemisorption. Physisorption is due to weak Van der Waals interactions between approaching gas phase species and the surface of the grain. It does not have an effect neither on the electronic structure of the gas phase species nor on that of the surface. In general, the well depths of physisorption sites are in the range 0.01–0.2 eV at a distance of a few angstroms. Chemisorption on the other hand is characterized by a strong interaction between the gas phase species and the surface. This type of interactions includes chemical bonds of the ionic or covalent variety, depending on the species involved. The well depths of chemisorption sites are ∼1 eV (fig. 2.4.1).

In molecular clouds, where dust grains are covered with icy mantles, the number of chemisorbed sites on the grain surface is very low. So, generally, gas phase H atoms will be adsorbed only in physisorption sites in dense molecular clouds.

**The formation process:** The formation of molecular hydrogen on the surfaces of interstellar dust grains may occur via two main mechanisms. The Eley-Rideal (ER), or "prompt", and the Langmuir-Hinshelwood (LH), or "diffusion", modes of formation. In the former case, the collision of an H atom from the gas phase with an atom which is already physisorbed to the grain surface leads to the formation of $H_2$ and its immediate release into the gas phase. In the latter case, the second H atom migrates across the grain surface until it encounters and reacts with another H atom, releasing the molecule.

[3]R is also noted as $\eta$ (Tielens, 2005) or $\gamma$ (Gould & Salpeter, 1963).

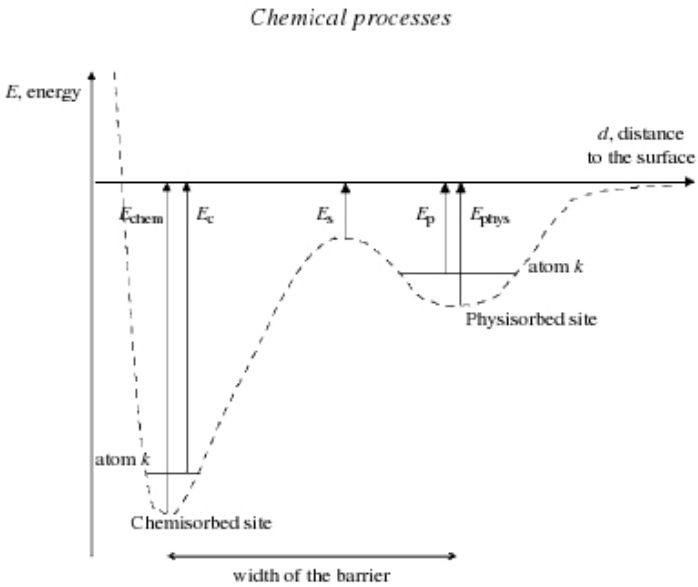


*Figure 2.4.1: The interaction between an adsorbate and a surface as a function of the distance to the surface. Two types of sites can be recognized: physisorbed sites due to van der Waals interaction (binding energy, $E_{phys}$) and chemisorbed sites involving shared electrons (binding energy, $E_{chem}$). The actual binding energies of a species, $E_p$ and $E_c$, take the zero-point energy into account. The two types of sites are separated by a saddle point with energy, $E_s$ (from Tielens (2005)).*

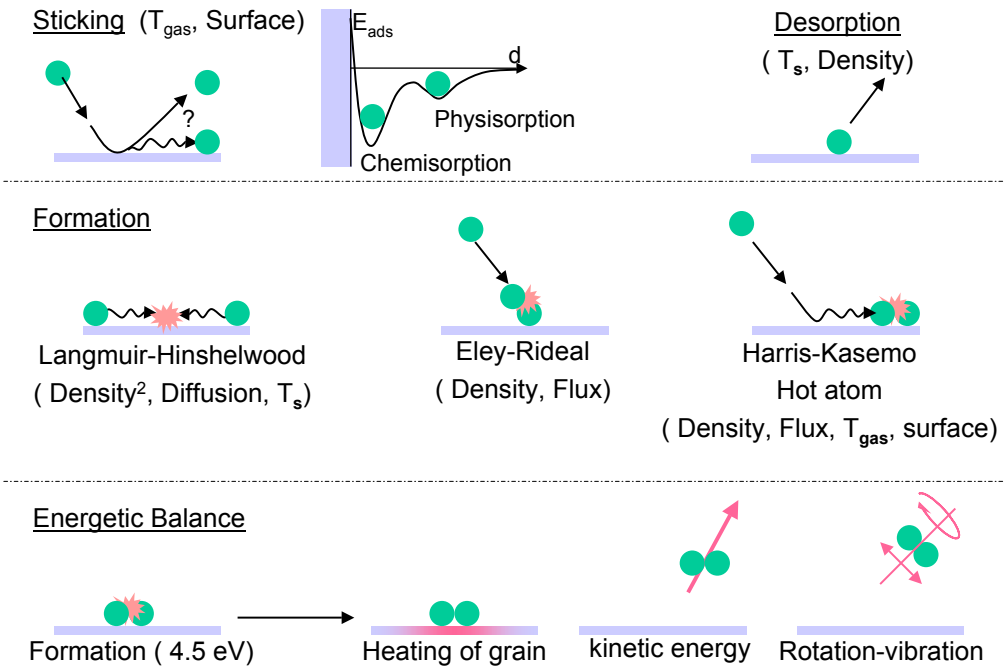


*Figure 2.4.2: Different processes leading to $H_2$ formation on the surface of interstellar dust grains. Separated into three steps: the adsorption of the atoms (sticking, chemisorption and physisorption), The formation reaction (Eley-Rideal or diffusion) and the energy partitioning (local heating, kinetic or rovibrational energy). The different parameters on which these processes depend are also shown ($T_{gas}$, $T_{surface}$, flux, density and surface morphology).*

The ER mechanism depends on both the density of adsorbed atoms and on the flux and temperature of the gas, while the LH depends on the adsorption energy of atoms as well as on the gas and surface temperatures.

Several teams have demonstrated by calculations (Sha et al., 2002; Morisset et al., 2005) and by interpretations of experimental results (G. Vidali's team - Syracuse) that, under the conditions of dark interstellar clouds ($T_{grain}$ = 10–20 K), the LH mechanism is the most efficient route to $H_2$ formation.

For a hydrogen atom to form $H_2$ on a surface, first it should stick on it then either encounters directly another H atom coming from the gas phase (ER), or diffuses on the surface until it finds another H atom already adsorbed on the surface and reacts with it (LH), or desorbs before encountering any other atom. Figure 2.4.2 shows schematically the different steps and processes leading to the formation of molecular hydrogen on interstellar dust grains, with the addition of a third mechanism that will be introduced later on.

**The sticking process:** The probability for an atom from the gas phase to hit the surface of the grain and stick on it is defined by the sticking coefficient or sticking probability $S$. Several definitions exist for this quantity. In this thesis the sticking coefficient is defined as the probability of an incident species to thermalise to the temperature of the surface (Govers et al., 1980). This probability depends on several parameters such as the kinetic energy of the incident atom, the surface temperature, its morphology and the adsorption energy which is the binding energy of the atom on the surface.

**The prompt desorption** of atoms, that takes place spontaneously due to the thermal activity, limits the residence time of atoms on the grains and can prevent the surface from reaching a sufficient density of adsorbed atoms to allow the formation reaction. This process depends, in general, on the temperature and morphology of the surface and on the adsorption energy of atoms.

**The diffusion of atoms:** This process enables the atoms to migrate on the surface where they can encounter other adsorbed atoms and react with them. They can also reach sites of greater adsorption energy which increases their residence time on the grains. There are several types of diffusion:

1. The thermal hopping (LH) that we previously mentioned.

2. The Harris-Kasemo or "hot atom" mechanism: an atom with a high kinetic temperature (few hundred degrees K) lands on the surface and experiences several jumps losing a small amount of its energy within each jump before it thermalises to the surface temperature. This mechanism depends on the kinetic temperature of the gas, the atom density on the surface and the morphology of the surface.

3. The tunnelling or quantum diffusion that makes possible the passage of

an atom from a physisorbed site to a chemisorbed one (diffusion length ∼60 Å and diffusion time ∼1.7 ps (Takahashi et al., 1999b)). This diffusion does not depend neither on the kinetic temperature of the gas nor on the surface temperature.

## 2.5 Previous studies

All the processes leading to the formation of molecular hydrogen on the surface of dust grains are still not very clear and not well understood. The nature of the grain (silicate, carbonaceous, ice,...), its structure (amorphous, porous or crystalline), its physico-chemical state (magnetism, neutral or ionic,... ) and the conditions of the medium (gas and grain temperatures, radiation) are parameters that we do not yet fully understand the effects. Also a very important information but yet uncertain is the partition of the binding energy of $H_2$ (4.48 eV) following the reaction, between translational, vibrational and rotational modes of the molecule and excitation of the phonon spectrum of the grain. Both experimental and theoretical works are continuing in an attempt to elucidate these issues.

The publications of Gould & Salpeter (1963) then Hollenbach & Salpeter (1971) are the founders of the theory of $H_2$ formation via gas-grain reactions. They placed the theoretical ground works on the subject by estimating the formation rate by emphasizing the importance of the residence time of atoms on the surface.

The publication by Pirronello et al. (1997b) presents an introduction on the advances in this subject in the 80's and the 90's. It suggests the use of an experimental set-up built by G. Vidali at the University of Syracuse (USA) to study the efficiency of the formation reaction. They have used an ultrahigh vacuum apparatus and two atomic beams, H and D, to study the efficiency of the reaction by measuring the amount of HD formed at surfaces in the range 6–30 K typical for the physisorption of hydrogen. They have studied the formation efficiency on surfaces of astrophysical relevance: silicates (Pirronello et al., 1997a,b), amorphous carbon (Pirronello et al., 1999), water ice (Perets et al., 2005) and CO ice (Vidali et al., 2004). In parallel, they have developed a model to fit their experimental data, thus allowing them to extract the key parameters: adsorption energy, diffusion barrier, re-capture of the formed molecules (Biham et al., 1998; Katz et al., 1999).

The conclusions of these works depend on the considered surface, however we can extract the following relevant information. H and D atoms stick by physisorption on the cold surfaces (∼10 K). When the surface is heated, desorption of HD is observed at a temperature depending on the nature of the surface. They interpret their results by assuming that atoms are likely immobile on the surface at 10 K and that it is necessary to heat the surface

(as induced by the TPD process) to lead to their mobility and then activate the formation right before the desorption takes place. Thus the mechanism involved is that of Langmuir-Hinshelwood thermally activated, and efficient in the grain temperature range 10–20 K.

In parallel, theoretical studies concerning the processes involved in the formation were also developed. The sticking of atomic hydrogen on water ice has been studied by Buch & Zhang (1991); Masuda et al. (1998) and most recently by Al-Halabi et al. (2002), who showed that the sticking coefficient on a surface at 10 K is almost unity for a gas temperature equal to 50 K and decreases to become zero at temperatures higher than 500 K. Sticking on graphite was also studied recently (Sha et al., 2005). The formation mechanisms were also discussed theoretically. Takahashi et al. (1999b) used Classical Molecular Dynamics (CMD) calculations to study the efficiency of sticking, mobility and formation of $H_2$ on amorphous ice. These calculations also predicted that the newly formed molecules are in a rovibrationally excited state (Takahashi et al., 1999a). Sha et al. (2002) demonstrated by DFT[4] calculations that the ER formation mechanism on graphite has an important cross-section (6 to 10 Å$^2$) but can only be the major formation route in media where the gas is sufficiently hot ($T > 1000$ K) so that the formation from physisorbed atoms via the LH mechanism becomes improbable and requires that atoms have sufficient kinetic energy to become chemisorbed. They also show that in this case, the molecules are formed in an excited state ($v \approx 5-8$ and $j \approx 3-8$). Morisset et al. (2005) in another theoretical approach found that the probability of forming $H_2$ via LH by physisorbed atoms on graphite is very high and that these molecules are released in an excited states (typically $v \approx 6-14$ and $j \approx 6-14$).

Despite the fact that theoretical works on this subject are progressing, it is of course necessary to continue the experimental investigations in order to validate their results. Three other teams in the world are oriented towards this kind of research. The S.D. Price team in London (University College London, UK), the team of A. Luntz and A. Baurichter at the University of South of Denmark (Syddansk Universitet, Odense) now led by L. Hornekær in Aarhus (iNano group) who studied the recombination of hydrogen on graphite by STM techniques (Hornekaer et al., 2006) and finally, our team led by Jean-Louis Lemaire at the University of Cergy-Pontoise and the Observatoire de Paris-Meudon. The principle of experiments is similar to that developed first at Syracuse mainly using thermally programmed desorption (TPD). Some teams use rovibrational laser excitation spectroscopy of the formed molecules to measure the populations in each rovibrational quantum state, and some preliminary results were obtained (Perry & Price, 2003; Creighan et al., 2006). Other than these four groups, some teams also contribute in an indirect way

[4]Density Functional Theory, a part of the non-relativistic quantum theory

to the experimental study of molecular hydrogen formation on surfaces. We can cite the studies on hydrogenation as well as the UV photodissociation of $H_2O$ (Yabushita et al., 2008a,c), PAHs (Joblin, 2004) and carbonaceous chains (Mennella, 2008a,b) that can be a source of $H_2$. Worth to mention the Aarhus team (Denmark) for its recent results on the recombination of hydrogen on graphite (Hornekaer et al., 2006) studied *in situ* by means of STM (Scanning Tunnelling Microscopy).

Concerning the experimental studies conducted on water ices at very low temperature, the different mechanisms ruling the formation on several possible types of ices are still not well understood. In fact, the Danish team (Hornekær et al., 2003) showed that the conclusions of the Syracuse team on ice surfaces can be questioned. They have demonstrated that if the desorption of molecules is thermally activated, the recombination of two hydrogen atoms can certainly occur at 10 K. They also underlined the major role that plays the morphology of the ice surface, whose porosity favours the re-capture of the newly formed molecules, thus complicating the processes that take place in a laboratory experiment. The disagreement on the interpretations arises from the differences in the experimental conditions used by each team. Beams fluxes and their temperatures, as well as the exposure times sould be taken into account in order to compare the experiments (Perets et al., 2005). We can also notice that water ice is a complex surface and that the conditions in which it was prepared should be better and more precisely defined in order to compare the results of the different experiments. Figure 2.5.1, for example, show the differences between the desorption profiles of molecular hydrogen on surfaces that are in principle similar.

**The present work** is an additional and new contribution to the study of the interaction and formation of molecular hydrogen on amorphous water ice surfaces under astrophysically relevant conditions.

Several experiments have been conducted on this subject by means of an apparatus constituted of the totality of diagnostics that can be found on the experimental set-ups used by the international teams previously mentioned. The surfaces used in this study are porous and non-porous amorphous water ices that can be found covering the dust grains in the dense molecular clouds of the interstellar medium. The choice of this type of surfaces was motivated by the uncertainty that persists in the interpretations of the experimental studies of the other teams. These surfaces are relatively easy to produce in the laboratory in a chamber under ultra-high vacuum conditions and are very easily reproducible. And most importantly, some properties can be controlled and varied, such as the thickness and the porosity of the ice leading to various binding energies that are of primordial importance for the formation of molecular hydrogen on the grains.

This thesis work gives additional and important information on the pro-

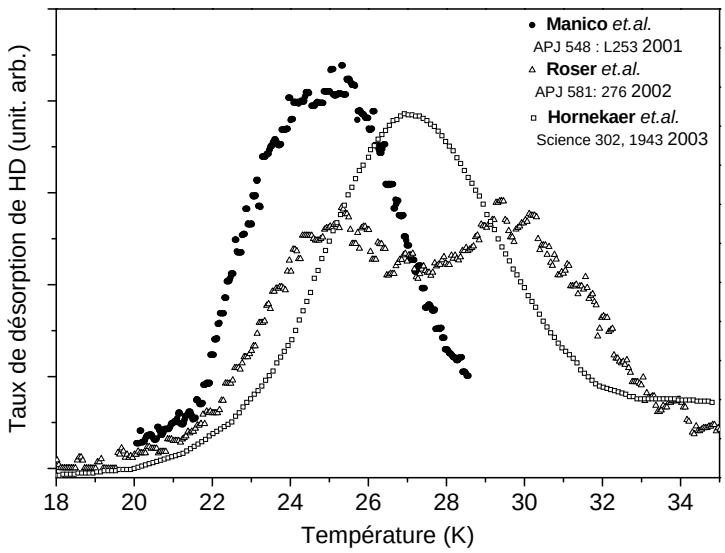


*Figure 2.5.1: Different results of similar experiments of HD formation on water ice surfaces. Manicò et al. (2001): 1200 layers of water formed at* 10 *K and exposed to* 18 *min of H and D; Roser et al. (2002): 1200 layers of water* 10 *K and exposed to* 4 *min of H and D; Hornekær et al. (2003):* 2000 *layers of water deposited at* 10 *K and exposed to* 10 *min of H and D. These results were obtained for similar heating ramps.*

cesses that lead to the formation of molecular hydrogen on icy dust grains. As a first part, our experimental set-up FORMOLISM is presented in detail, along with the analysis methods that we used during this thesis and the growth of the different water ice substrates. In the second part I will give a detailed description of the experiments I have conducted on the sticking of atomic and molecular hydrogen, the mobility of atomic hydrogen and finally the formation of molecular hydrogen on amorphous water ices under dense clouds conditions. I will emphasize the importance of the morphology of this ice which can explain the de-excitation of the newly formed $H_2$ molecule and the partitioning of the energy released upon its formation.

# Chapter 3

# The FORMOLISM set-up

FORMOLISM (FORmation of MOLecules in the ISM) is an instrument specially built to study reactions and interactions of different types of atoms and molecules with surfaces under conditions relevant to astrophysics (very low temperature (∼8 K) and very low atomic and molecular densities). It is composed of an ultra-high vacuum (UHV) stainless steel chamber schematically drawn in figure 3.0.1 and a copper sample holder that can be controlled in temperature in the range 8 K - 800 K. Two beam lines attached to the chamber and directed towards the sample holder are used to introduce the atomic or molecular gases. The interacting and desorbing species in the chamber are detected via a quadrupole mass spectrometer (QMS) or a time-of-flight (TOF) mass spectrometer coupled to a UV excitation laser beam.

## 3.1 The UHV main chamber

The background pressure in the chamber is around $10^{-10}$ mbar corresponding to a mean density of $10^6$ cm$^{-3}$, composed mainly of molecular hydrogen at 300 K. Even if it is the best value that can be reached in the laboratory, this density is still higher than that found in dense cores estimated to be $10^4$ cm$^{-3}$ (Williams & Herbst (2002)).

The UHV chamber is a non-magnetic stainless steel cylinder of 120 cm in height with a diameter of 30 cm (MECA2000). The base pressure is obtained via a molecular turbo pump 1000 l s$^{-1}$, a titanium sublimation pump and an ionic pump (for more efficient pumping in the $10^{-10}$ mbar range). The UHV is maintained to keep the surface clean and prohibit residual water molecules that are in the chamber to be adsorbed on it (at a base pressure of 1 $10^{-10}$ mbar it takes $\sim$ 5000 minutes to grow 1 ML of water).

The quality of the vacuum is always affected by the desorption of the previously and successively adsorbed species. This desorption is compensated by pumping and both determine the limiting value of the vacuum. This source of pollution is expressed by what is called the "baking" desorption rate, which is of the order of 5.0 $10^{-10}$ mbar l s$^{-1}$ cm$^{-2}$ before baking (Baouche, 2004).

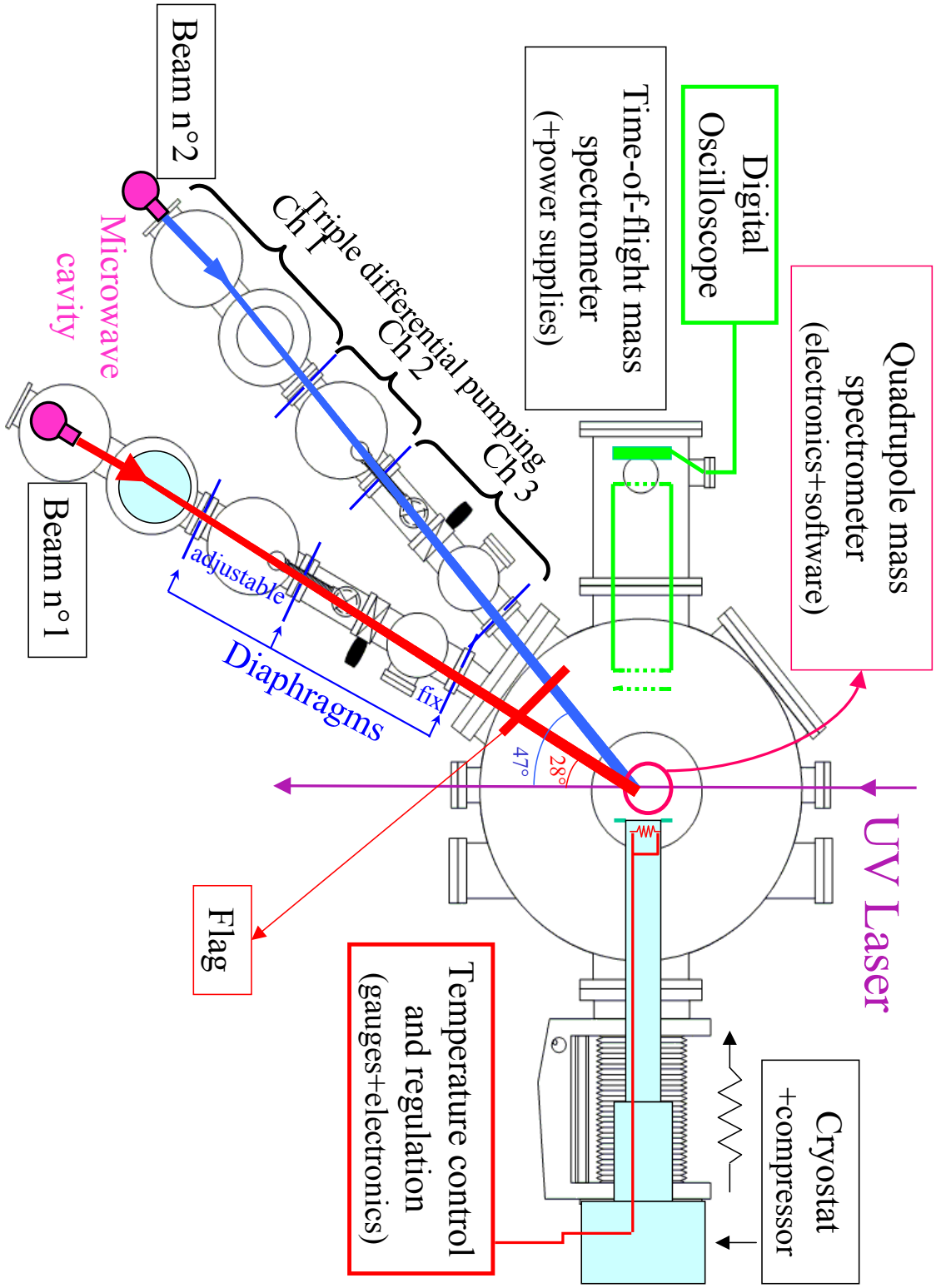


*Figure 3.0.1: The FORMOLISM set-up.*

Baking consists on heating at quite a high temperature (usually around 100°) the UHV chamber to temporarily increase the baking desorption rate of the inside wall of the chamber in order to remove a large amount of the adsorbed species after each opening of the experimental set-up. When cooling down back to room temperature, the desorption rate is reduced and the base pressure is then lowered. Before the baking operation, the minimum pressure obtained with turbo molecular pump in the chamber is $\sim 2\ 10^{-9}$ mbar. A usual procedure is to heat the chamber for 5 days to a maximum temperature of 100°C. In any case the mechanical parts of the cryostat cannot be higher than 80°C. An automat, driving sectorised heating wires under the control of thermocouples, allows the regulation and the control of the heating rate for the most fragile parts (windows, bellows,...). Before the heating phase, we cover the apparatus with isolating aluminium foil and progressively increase the temperature until we reach 100°C and maintain it for three days. When we stop the heating, the temperature decreases gradually to stabilize at room temperature ($\sim$20°C) and the base pressure is then lower than $\sim 10^{-10}$ mbar. The automat is controlled via a homemade Labview designed software. The whole baking procedure takes about 7 days. Figure 3.1.1 shows the species present in the UHV chamber before and after baking and recorded with the QMS. One can see that nitrogen almost completely disappear and that the water partial pressure is reduced by a factor of 100.

## 3.2 Sample holder and cryogenic system

### 3.2.1 The cryostat

The sample holder is mounted on a 800 K interface, mounted itself on the second stage of a cryo-cooler (fig. 3.2.1). The cryostat is a Arscryo DE204 model that works on He gas circulation, coupled to a APD:HC-4 compressor. The cryostat enables to reach a primary temperature of 4.2 K. The thermal transfer is caused by the compression and relaxation cycle of a piston following the Gifford-McMahon scheme, allowing to attain a typical cooling power of 0.4 W at 10 K. The cryostat includes two stages (fig. 3.2.1). The 800 K interface, situated between stage 2 and the sample holder, contains a ruby crystal acting as a thermal switch. It allows the sample holder to be heated up to 800 K.

The sample holder is a OFHC (Oxygen-Free High Conductivity) polished copper cylinder (now it is gold plated for the purpose of IR spectroscopy) screwed on the 800 K interface. A very thin disc of silver foil insures a good thermal conductivity between these two elements. A thermal shield attached to the base of the cryostat (stage 1) isolates the upper stages from the thermal radiations of the environment. It is composed of a nickel-coated copper cylinder and a homemade cover as shown in figure 3.2.1. The internal part of the cover is made of copper and the external one is made of stainless

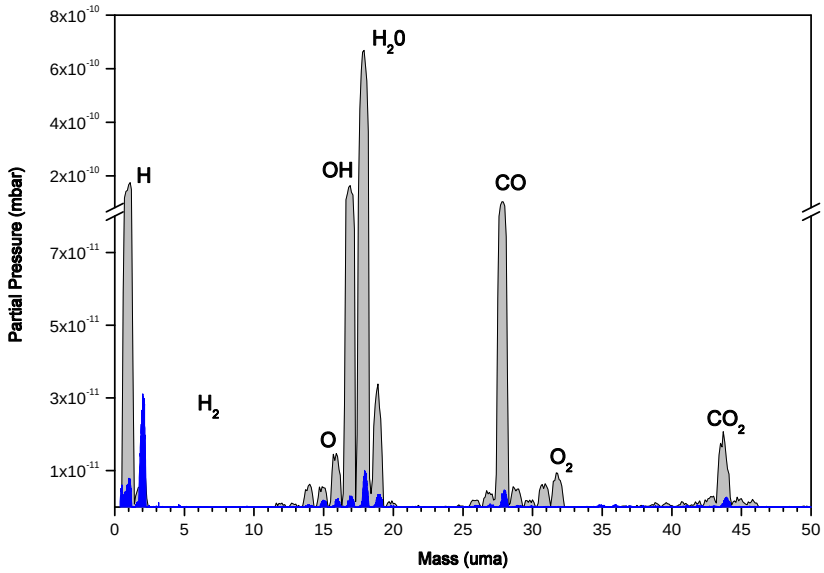


*Figure 3.1.1: Residual gases in the UHV chamber before (gray) and after (blue) baking. Some species disappear as well as their fractions that are formed by cracking in the head of the QMS. The main peaks are those of hydrogen (M=1, 2), $H_2O$ and OH (M=18,17), nitrogen (M=14), oxygen (M=32,16) and carbon dioxide (M=44,28).*

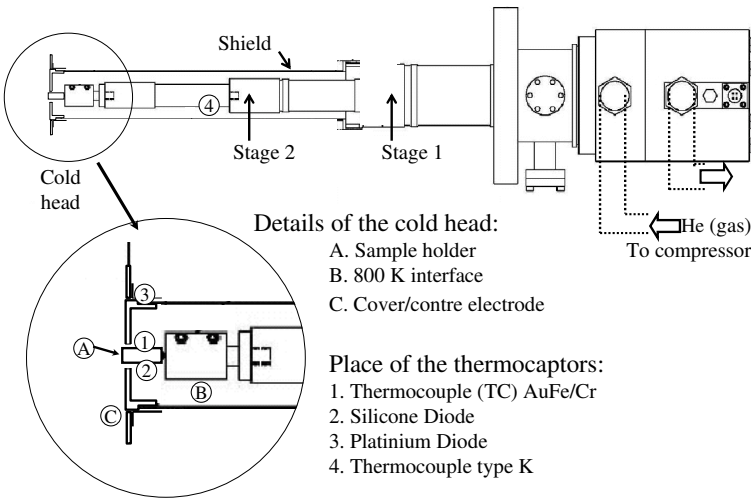


*Figure 3.2.1: Scheme of the cryostat and details of the cold head.*

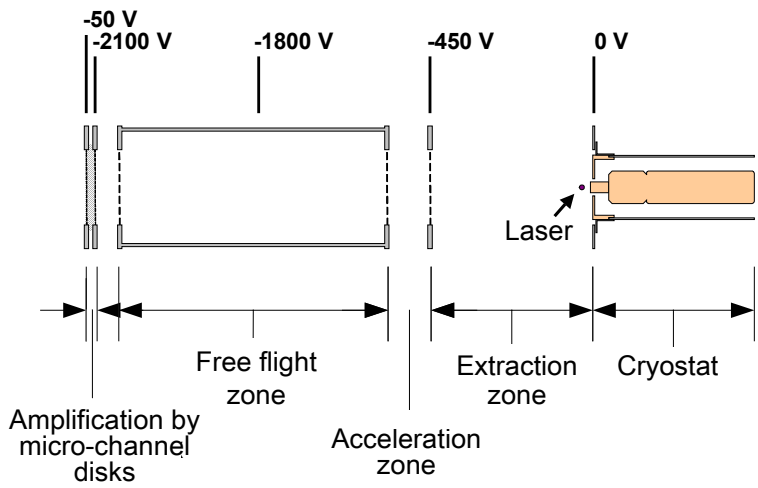


*Figure 3.2.2: Time-Of-Flight (TOF) mass spectrometer. The head of the cryostat acts as a counter-electrode related (connected or bound) to the mass. The voltages are indicative and are adjusted to improve the signal intensity and the mass dispersion (scattering).*

steel decoupled by ceramic pieces from the main body (see fig. 3.2.1). This cover also plays the role of a counter-electrode to the Time-Of-Flight (TOF) mass spectrometer (cf. fig. 3.2.2).

Despite the fact that the temperature at the bottom of the second stage is 4.2 K, the final temperature of the sample holder is never lower than 8 K due to the successive losses due to the 800 K interface, the thermal shield extension and particularly to the necessity to have an open geometry that exposes the surface of the sample holder to IR radiations inside the UHV chamber.

The whole set is mounted on a translation stage that allows us to move back and forth the sample holder with respect to the centre of the chamber in order to allow a better positioning of the QMS, of the capillary water vaporiser or of the laser beam.

### 3.2.2 Temperature measurement and control

Three different types of sensors measure the temperatures on the cryostat assembly: a KP-type thermocouple (Au 0.07%–Fe/Chromel), a K-type thermocouple (Nickel–Chromium/Nickel–Aluminium) and a silicone diode (DT 470) (fig. 3.2.1). A heating resistance is attached to the 800 K interface. The three sensors and the resistance are connected to a Lakeshore

340 temperature controller in order to regulate the temperature of the sample holder. Calibrations of the sensors are done by measuring the Ar and $N_2$ sublimation temperatures (Schlichting & Menzel, 1993). The controller used allows the tuning of the temperature of the sample holder thanks to a Proportional-Integral-Derivative (PID) servomechanism that controls the power of the heating resistance and that will be described in detail in a following section. A homemade Labview program drives the Lakeshore 340 via a computer interface.

This program allows the following procedures:

- control the PID parameters depending on the temperature range of the sample holder,
- control and regulate the heating ramps to obtain a linear heating ramp,
- monitor and record the temperature measured by the sensors during the whole time of the experiments,
- adjust the heating power settings in order to get a linear increase of $T$ on large temperature ranges, if required.

## 3.3 Water ice formation on the sample holder

Various ice substrates are obtained by condensation of water vapour on the sample holder. Depending on the kind of ice we would like to grow, two different methods are used: either slow deposition by background pressure or fast deposition (see Chapter 4 section 2 for more details). For the latter case, a specific device is part of FORMOLISM for this purpose: a water vapour diffuser or vaporiser.

### 3.3.1 Water vapour diffuser

Purified liquid water is contained in a stainless steel or a glass bottle of $\sim$100 cm$^{-3}$. The purification of 100 cm$^{-3}$ of demineralised water consists in three solidifiction-fusion cycles in order to remove all the impurities by pumping them out of the bottle. The water bottle is connected to a 100 l.s$^{-1}$ turbo pump and a pressure gauge. The bottle delivers the saturating water vapour pressure of about 20 mbar which feeds the UHV chamber via a Varian low rate leak valve[1]. Water is diffused into the chamber via a micro-capillary array at the end of a 30 cm and 4 mm ID stainless steel tube. This allows a homogeneous diffusion of water vapour into the chamber. The valve-diffuser system is mounted on a translation stage allowing several vertical positions. When the QMS or the TOF mass spectrometer are operating, the diffuser is placed in a high position so that it does not perturb their electric fields. It can also be placed directly in front of the surface. Both high and low

[1] A precisely adjustable piston made of an optically flat sapphire closing a captured metal gasket. It allows leak rates down to $10^{-10}$ Torr.

positions can be used to deposit water vapour on the surface to grow the ice films.

### 3.3.2 Growth of the ice

The properties of the ice grown from the gas phase will be discussed in detail in a following chapter. These properties depend on the incident angle of molecules, the surface temperature during deposition and other changes in temperature that the ice might be subject to after deposition. We can grow the ice in two different deposition modes: the background deposition mode (high position) where the diffuser is far from the surface and the direct deposition mode (low position) where the diffuser is facing the surface.

In the background deposition mode, water vapour fills the entire volume of the UHV chamber before reaching the surface. Thus the pressure in the chamber increases and the distribution of the incidence angles of water molecules meeting the surface is fully isotropic.

The deposited quantity of water is calculated by measuring the base filling pressure signal during the entire deposition time. This method is applicable for all species that have a residual partial pressure in the chamber, in particular to evaluate the quantities of exposed $H_2$. The flux, or condensation rate, can be calculated readily from the kinetic theory of gases. Following the reasoning of Hertz, Knudsend and Langmuir, this flux is determined by the number of molecules in the gas-phase which collide per unit time with the surface (of unit area):

$$f = \frac{1}{4}\bar{v}n$$

where $n$ is the density of molecules (per unit volume) and $\bar{v} = \sqrt{8\mathrm{kT}/\pi m}$ is the average velocity of the considered gas-phase species. The density $n$ of molecules can be replaced by the pressure using the Clapeyron-Mendeleev equation:

$$n = \frac{P}{k_B T}$$

By substitution, we obtain

$$f = \frac{P}{\sqrt{2\pi m k_B T}}$$

known as the Hertz-Knudsen equation (L'vov, 2007).

A computer program calculates the molecular flux from the pressure gauge signal and applying a correction factor to take into account the detection efficiency for the specific species considered. It integrates in fact the number of molecules that hit the sample holder from the beginning of exposure and thus allows the surface density measurement. Surface densities are expressed in monolayers (ML). One monolayer corresponds to a complete atomic layer and is usually defined as 1 ML $=10^{15}$ molecules.cm$^{-2}$.

The sticking probability of water molecules at low temperatures (10–120 K) is close to unity (Tielens, 2005). So in order to grow 1 ML of water on the surface, we should set the $H_2O$ partial pressure in the chamber to $\sim$1.0 $10^{-8}$ mbar for about 5 minutes. Taking into account that water molecules are adsorbed on the walls of the UHV chamber, thus deteriorating the vacuum limit, only small amounts of water can be deposited on the surface using the background deposition.

The direct deposition mode is used to deposit large amounts of water molecules on the surface of the sample holder. This mode consists on positioning the capillary vaporiser 20 mm in front of the surface. The micro-capillary array has a surface of 1 cm in diameter and is composed of hundreds of water vapour sources each of them delivering the gas with an angular aperture of 45°. Between the micro-capillary array and the sample holder, the local pressure during the growth of water is estimated to $10^{-6}$ mbar while the residual pressure in the chamber stays around $10^{-9}$ mbar. This means that the distance travelled by molecules is very short compared to the mean free path ($\sim$1 m at $10^{-6}$ mbar). As a consequence, the contribution of water to the pressure in the chamber is limited because most water molecules that are diffused by the micro-capillary system hit the surface of the sample holder or the cryoshield.

The advantage of the direct deposition mode is the growth of several ice monolayers in a couple of minutes. By comparing the water TPDs of the two deposition modes, we have estimated that by direct deposition we grow $\sim$0.33 ML per second while the pressure in the chamber is maintained at $2.10^{-9}$ mbar.

## 3.4 Quadrupole Mass Spectrometer (QMS)

The QMS is manufactured by Hiden company, model 51/3F (mass range 1 to 50, triple filter). It measures the amount of gas species present in the UHV chamber with its ionizing head, selecting specific masses or scanning a given mass range by adjusting the radio frequency collection field as described below in more details.

### 3.4.1 Working principle

Figure 3.4.2 shows how a QMS works. The QMS is composed of an ionisation head, an ion travel zone delimited by four electrodes and an ion detector. The species are ionised by the electrons emitted by a filament and then accelerated towards the travel zone where they are filtered and selected by mass. The mass filtering is obtained by applying a DC and an AC radio frequency voltages on a set of four electrodes. Only ions with a given $Z/m$ are selected and guided by resonance with the oscillating voltage to the ion detector. The other ions are expelled from the travel zone and are neutralised

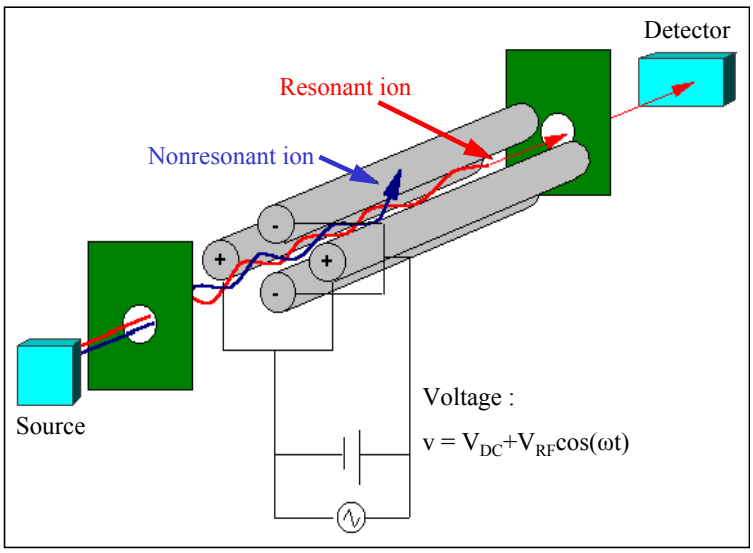


*Figure 3.4.1: Working principle of the mass filter in the quadrupole mass spectrometer.(Tissue, 2000)*

on the four electrodes. In fact, our model contains a triple filtering system to increase the resolution. The ion detector is a channeltron that, with a maximum voltage of 3000 V, creates secondary electronic avalanches after the impact of an ion. Partial pressures are detected up to $10^{-14}$ Torr. This kind of detector has to work with pressures lower than $10^{-6}$ Torr. The output current of the channeltron is then converted into a digital signal led to a discriminator and a counter and the signal is then expressed in counts per second (cps).

**The main characteristics of the QMS:**

**- Measurement** range from 1 to 50 uma (a 1 to 300 uma is also available in our laboratory).

**- Resolution** for two adjacent peaks of the same intensity, intermediate minimum of 0.5%.

**- Dynamic** of $10^7$ cps. Allows to measure partial pressures up to some $10^{-15}$ mbar.

**- Electron ionising energy** of 10 eV to 200 eV, adjustable via software.

**- Measurement frequency** is about 4 Hz.

### 3.4.2 Integration and use of the QMS

The QMS is used for three purposes: (1) to analyse the residual gas in the UHV chamber, (2) to characterize the dissociation in atomic and molecular

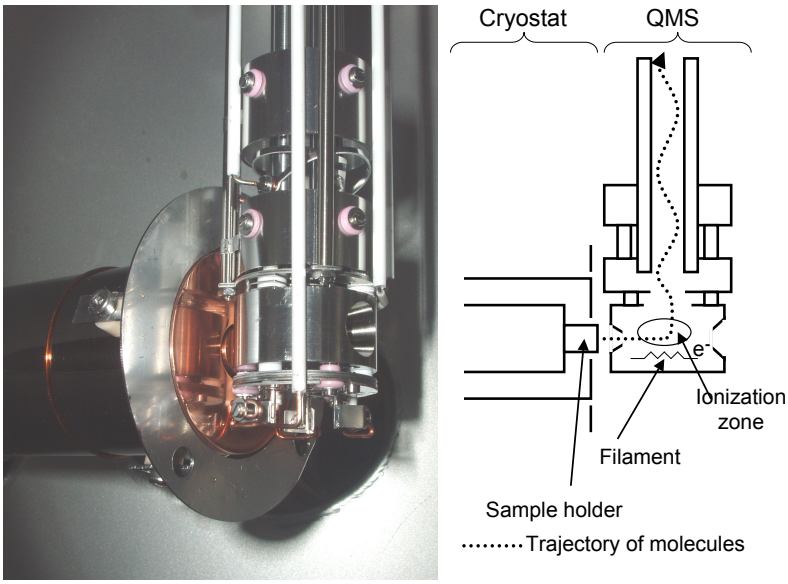


*Figure 3.4.2: QMS in low position facing the surface to detect species desorbing from the surface of the sample holder. The diagram on the right shows the different parts of the photograph. A portion of the surface of the sample is visible behind the QMS. The exit hole of the QMS is on the right, the entrance hole is seen by reflexion on the polished copper surface of the thermal shield. The long white parts are ceramic tubes surrounding the wires that release the acceleration and ionization voltages.*

beams and (3) to measure the desorption rate of species that were adsorbed on the surface. The QMS can be translated vertically and rotated. In its high position it serves to analyse the gases present in the chamber and in its low position, it can either face one of the beams in order to characterize it and its dissociation rate or face the surface to measure the desorption rate (cf fig. 3.4.2).

The QMS is installed directly in the UHV chamber and without differential pumping. The ionising filament in the head stays turned on during the time of the experiments to avoid consecutive degassing when switching it on. An outgassing procedure during which the filament is strongly heated allows to considerably limit the impact of this source of pollution.

The ionisation head is a partially open volume, only accessible by an inflow and an outflow diaphragms (fig. 3.4.2). Until September 2008, the entrance hole external diameter is 5.5 mm and the internal diameter is 1.5 mm with an angle of $\pm 13°$ and the exit hole external diameter is 9.7 mm and the

internal diameter is 6.0 mm with an aperture of ±12°. Since February 2009, the entrance characteristics are similar to the exit ones. When the QMS is facing one of the beam lines, it collects now the entire beam (3.3 mm in diameter). It is then used to measure the flux and the dissociation rate. When facing the surface, at a distance of 2-3 mm, it collects directly the molecules that desorb from a ∼75 $mm^2$ surface, about ten times bigger than the surface initially exposed to the beam. The new head configuration allows a better evacuation of the gas, avoiding any confinement that can increase the residual pressure in the head of the QMS. In any case, the contribution of the residual gas of the chamber in the measured signal has to be taken into consideration. In practice, the correction applied to $H_2$ signal is constant since the presence of this gas is due to permanent desorption from the walls of the UHV chamber. The other hydrogen sources are transient, either those resulting from translation motions in the chamber (surface, QMS, ...) or from valve openings, or those that are of interest to us such as desorptions from the surface. Signals, in general, have a very short lifetime, typically some 100 ms, thanks to the high pumping capacity in the chamber[2].

The electronic system of the digitalized signal of the QMS is controlled by a software provided by Hiden. It allows to record sequentially several masses or to record a defined mass only or to scan a selected continuous range. Setting and dwelling times may be adjusted by software. The shortest time between measurements is about 100 ms. The simultaneous recording of an external signal on the auxiliary entry is also possible. This option is used to monitor the temperature of the surface measured by the Lakeshore controller during TPD experiments. This software is used in "profile" mode to scan continuously a given mass range, analysing the residual gas in the chamber as shown in figure 3.1.1.

## 3.5 Cold atomic and molecular beams

Two atomic beam lines were developed for FORMOLISM, adapting the device described in Walraven & Silvera (1982). They allow to expose the surface to two different species simultaneously (e.g. $D/D_2$ and $O/O_2$). Each beam line is composed of three stages of differentially pumped chambers separated by diaphragms. In the first stage of each beam line there is a dissociation system that will be described in the following subsection. The beams can be molecular (dissociation turned off) or a mix of atoms and molecules (dissociation turned on), because the dissociation rate is never

[2] A rough calculation is proposed here: the surface of the turbo pump represents typically $1/100^{th}$ of the chamber's surface. Molecules are evacuated after a trajectory equal to 100×the size of the chamber, ∼100 m, which is done in 50 ms for a hydrogen molecule. This time is in fact a bit longer because the pump is not ideal.

100%[3]. In both beam lines, atoms and molecules can be cooled down to ∼25 K by passing through an aluminium nozzle screwed to the end of a cryostat.

### 3.5.1 Microwave plasma dissociation

The atoms (H, D and O) are obtained by dissociating the corresponding molecular beams. For that, we use a Surfatron provided by SAIREM (fig.3.5.1). The two components are an adjustable microwave cavity and a microwave power supply delivering 300 W at 2.45 GHz. The microwave cavity is traversed by a quartz tube (ID 4 mm) through which the molecular beam passes at a pressure ranging from 0.3 to 3 mbar. The impedance adaptation of the microwave cavity is done by two elements: the coupler and the plunger. This adaptation is tuned so that the power reflected by the Surfatron towards the microwave generator stays at the minimum. Microwaves transfer energy to the gas by exciting and ionising the species. They create a plasma in which electrons are accelerated. The dissociative electronic excitation of $H_2$, $D_2$ or $O_2$ produce atoms in the discharge zone. At the pressures used, the large number of collisions, especially on the walls of the tube, favours the recombination of molecules after being dissociated. To limit this spontaneous reformation, the quartz tube is air-cooled and the metallic parts are water-cooled. The gas is then directed into a Teflon tube through an aluminium nozzle (1st beam line) or directly from the quartz tube (2nd beam line) (see fig.3.5.1).

The dissociation rates that we obtain are generally between 50 and 80% for $D_2$ and 50–70% for $H_2$. The measurement of the dissociation rate is made by comparing the signals of the molecules measured with the QMS when the discharge is turned on and off. This method assumes implicitly that the amount of gas passing through the beam line is not modified when the discharge is turned on and off. This hypothesis can be justified by the two following facts: i) before and after the discharge, the pressure ratio that determines the gas outflow is conserved, ii) the gas exiting the discharge is cooled by collision before its expansion into the first chamber.

### 3.5.2 Triply differential pumping system

The principle of the beam lines is to select among the different species exiting the tube the ones that have a trajectory enabling them to reach the surface (very small solid angle ∼8 $10^{-6}$str). For this, the beam passes through three aligned diaphragms (see fig. 3.0.1, 3.5.1 and tab. 3.5.1). Each diaphragm (see diameters in tab. 3.5.1 ) leads to a separately pumped chamber, the last leading to the UHV chamber. The pressure, therefore, decreases

[3]It is due to the fact that recombination occurs on the tubing or on the successive diaphragms.

| Parameters | Tube | Chamber 1 | Chamber 2 | Chamber 3 | UHV chamber |
|---|---|---|---|---|---|
| Pressure (mbar) | 1 | $10^{-4}$ | $10^{-6}$ | $10^{-8}$ | $10^{-10}$ |
| Mean free path[a](m) | $10^{-5}$ | $10^{-1}$ | 1 | $10^{2}$ | $10^{4}$ |
| Travelled distance (cm) | $45^{1}$ $10^{2}$ | 2 | $33^{1}$ $40^{2}$ | 48 | 25 |
| Internal exit hole diameter (mm) | 4 | 2.5 | 2.5 | 2.5 | $3.3 \times 5.4^{1,b}$ $3.3 \times 4.0^{2,b}$ |
| Pumping speed ($l.s^{-1}$) | ∅ | 500 | 100 | 100 | 1000 |

[a]Mean free path for a collision cross section of 1 Å$^2$ and a temperature of 300 K.
[b]Vertical and horizontal axes of the elliptic intersection of the beam with the surface.

*Table 3.5.1: Characteristics of the differential pumping. Indexes 1 and 2 refer to beam 1 and 2 respectively. Incidence angles are respectively 62° and 43° for beam 1 and 2. The grazing angles are shown on fig. 3.0.1.*

gradually from ∼1 mbar in the tube to $10^{-10}$ mbar in the main chamber. The characteristics of the three chambers (stages) of each beam line are given in table 3.5.1.

The beam exiting the tube into the first chamber is effusive according to the Knudsen criteria $K_n = \frac{\lambda}{D}$, where $\lambda$ is the mean free path, D the diameter of the aperture. At this stage, the pressure in the tube is slightly higher than that in the first chamber ($10^{-4}$ mbar). $\lambda$ is therefore of the order of some centimetres, while D = 4 mm. Which means that we work in a regime where $K_n \geq 1$, an effusive regime. The temperature of the gas in the beam is therefore close to that of the tube.

When using the beam, an inevitable diffusion exists out of the third chamber into the UHV chamber through the last diaphragm. A negligible rise in pressure in the main chamber is then observed and is about 2 $10^{-11}$ mbar.

The diagrams in fig. 3.5.1 show the difference between the two beam lines. The absence of the elbow in the second beam line enables to widely reduce the recombination of atoms when the discharge is turned on. This allows us to work with slightly higher pressures and to obtain a better flux. On the other hand, the straight-line geometry enables the light emitted by the plasma to irradiate the surface, which is avoided in the first beam line.

In addition, a rotatable flag is placed in the main chamber just after the d3 diaphragm (fig. 3.0.1). This flag is used to avoid a direct irradiation of the sample by either of the beams but having in the main chamber the corresponding background pressure.

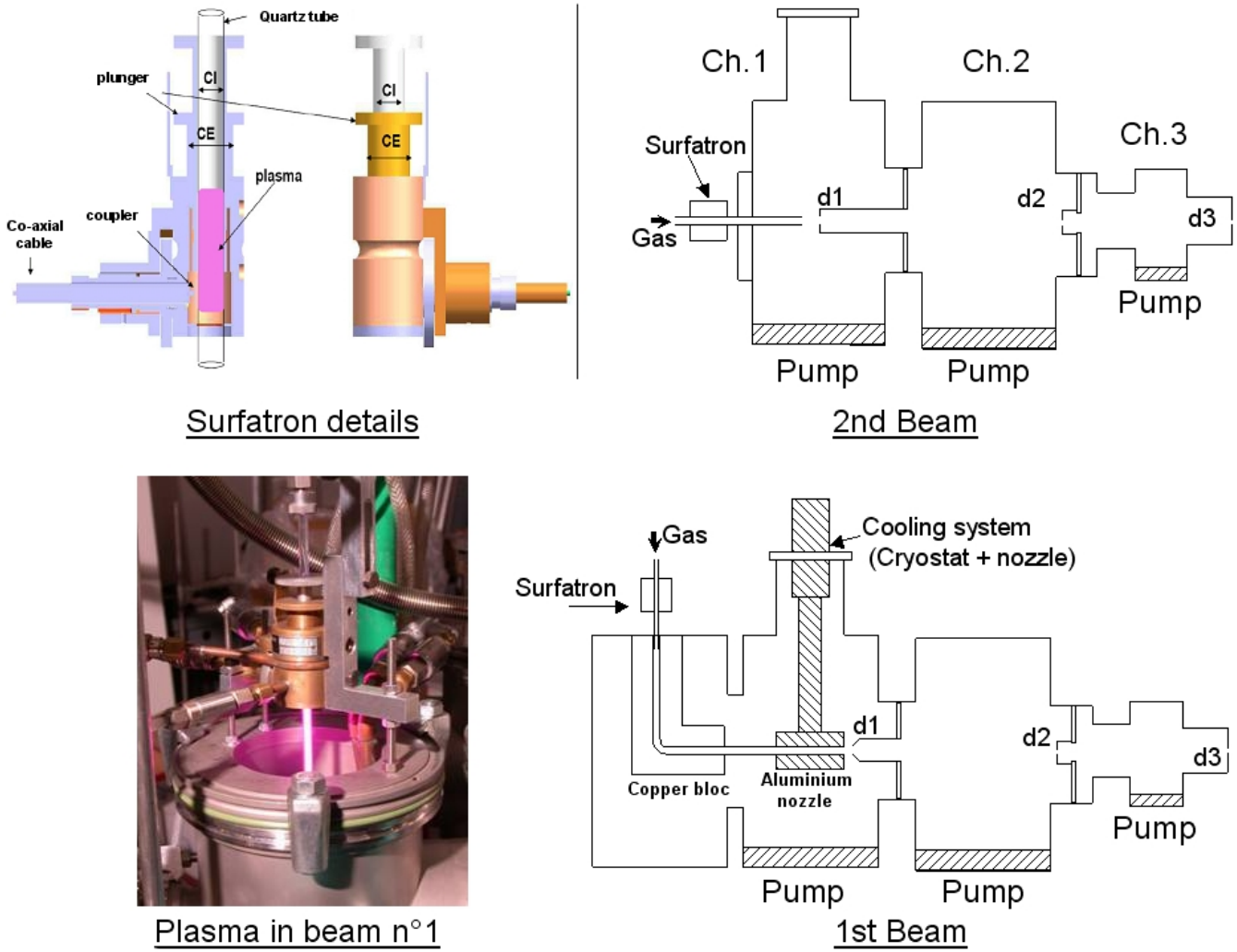


*Figure 3.5.1: Atomic beams. The drawing of Surfatron is shown in the top-left corner. The photograph show the microwave discharge in beam 1 during $H_2$ dissociation. The first and the second beams are represented top-right and bottom-right corners respectively. The second beam is shorter and is completely linear. The first beam, as well as the second one if necessary, can be cooled down via an aluminium nozzle attached to a cryostat.*

### 3.5.3 Flux calibration of the beams

The fluxes of the molecular beams are estimated to be $10^{12}$ cm$^{-2}$.s$^{-1}$ for the first beam line and $10^{13}$ cm$^{-2}$.s$^{-1}$ for the second beam line, with an error of ∼30%. The flux is measured using two methods, either a direct one or by comparing direct beam measurement to measurement where the gas is introduced into the chamber by residual pressure (background). The residual pressure is easily measured using the pressure gauge of the UHV chamber or the QMS and it corresponds to a flux of molecules, the gas being at room temperature inside the chamber.

The first method consists on measuring the signal with the QMS facing the beam. This signal is then compared to that obtained when the gas is introduced into the chamber by background when the above mentioned flag stops the beam.

The second method is less direct. It uses the adsorption/desorption processes on the surface. When the beam reaches the cold surface of the sample holder, molecules can be adsorbed. It is then possible to detect the amount of adsorbed molecules with the QMS by heating the surface to activate their desorption. An example with $O_2$ is shown on figure 3.5.2. The comparison of the amount of adsorbed molecules after direct beam deposition to that measured after background deposition enables us to find the pressure of the beam on the surface and therefore to find the flux.

Those two methods are complementary. The second one presents the advantage of measuring the effective flux on the surface. The error of 30% previously mentioned reflects the disagreement between the two methods.

### 3.5.4 Cooling system of the first beam

Figure 3.5.1 shows the cryogenic system in the first chamber of the first beam line. It is constituted of an Arscryo DE202 cryostat that can reach 10 K. An aluminium nozzle is attached at the end of the cryostat, in which molecules pass and cool down by hitting its walls. The aluminium combines the advantages of a good thermal conductivity and a low recombination rate of hydrogen on its surface due to the presence of an external layer of $Al_2O_3$ that gives the surface properties similar to Pyrex (Toennies et al., 1979) (Koch & Steffens, 1999). The minimum temperature that can be reached is ∼23 K. It can be controlled in the range $23 - 350$ K via a Lakeshore 332 temperature controller and read with a silicone diode (DT 470) attached to the nozzle.

The rotational temperature of the molecules in the beam can be determined by measuring the population of the different rovibrational states of $D_2$ using REMPI spectroscopy (see Amiaud (2006) for more details). This temperature can be a good indicator of the kinetic temperature. Another method to measure the kinetic temperature would be by adding a chopper associated to a fast pressure gauge to obtain the velocity distribution of species.

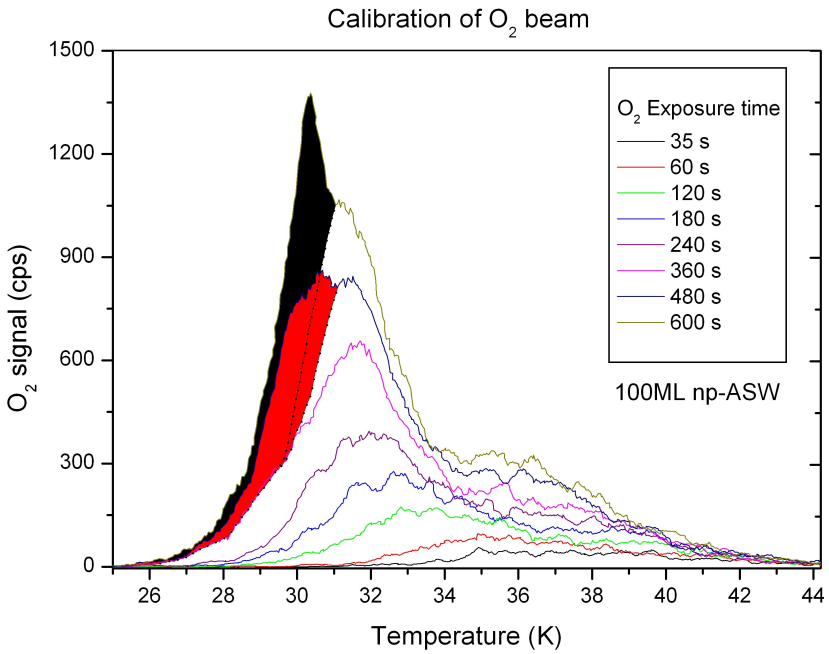


*Figure 3.5.2: Calibration of the $O_2$ beam. The saturation coverage is determined by a simple TPD method done on non-porous amorphous ice. We expose a compact ice surface to varying times of $O_2$ and we do a TPD after each dose (Kimmel et al., 2001a). When the multilayer peak in the O2 TPD profile starts to show up (see shaded shoulders of TPD traces), this means that we have saturated the first monolayer layer and we are starting to populate the second monolayer.*

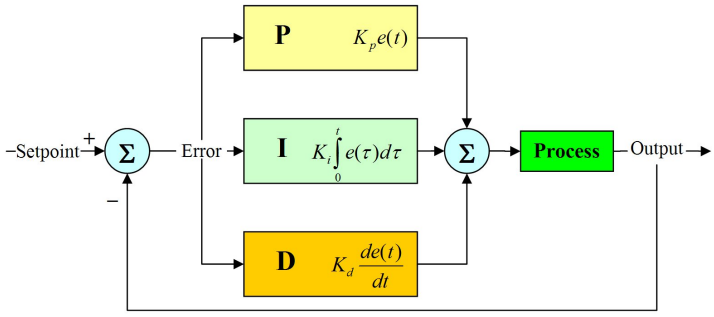


*Figure 3.5.3: A block diagram of a PID controller.*

### 3.5.5 Calibrating the Lakeshore 332 controller

During my thesis I have spent around two months to calibrate the temperature controller of the first beam line in order to conduct experiments that require cold beams of atomic and molecular hydrogen and deuterium. The Lakeshore 332 works using a PID (proportional-Integral-Derivative) controller that attempts to correct the error between the measured process temperature and a desired set-point by calculating and then outputting a corrective action that can adjust the process accordingly, to keep the error minimal. A block diagram of a PID controller is shown in figure 3.5.3. The three action parameters involved in the tuning of the controller are the proportional (P), the integral (I) and the derivative (D). Their sum constitutes the manipulated variable, in our case the temperature T. Hence:

$$\mathrm{T(t)} = \mathrm{P}_{out} + \mathrm{I}_{out} + \mathrm{D}_{out}$$

**The proportional term ($\mathbf{P}_{out}$)** sometimes called gain, makes a change to the output that is proportional to the current error value e(t). The proportional response can be adjusted by multiplying the error by a constant $K_P$, called the proportional gain. The proportional term is given by:

$$\mathrm{P}_{out} = K_P \mathrm{e(t)}$$

**The integral term ($\mathbf{I}_{out}$)** also called reset, is proportional to both the magnitude of the error and its duration. Integrating the error over time gives the accumulated offset that should have been corrected previously. The accumulated error is then multiplied by the integral gain $K_I$ and added to the controller output. The magnitude of the contribution of the integral term to the overall control action is determined by $K_I$. The integral term is given by:

$$\mathrm{I}_{out} = K_I \int_t^0 \mathrm{e}(\tau)\mathrm{d}\tau$$

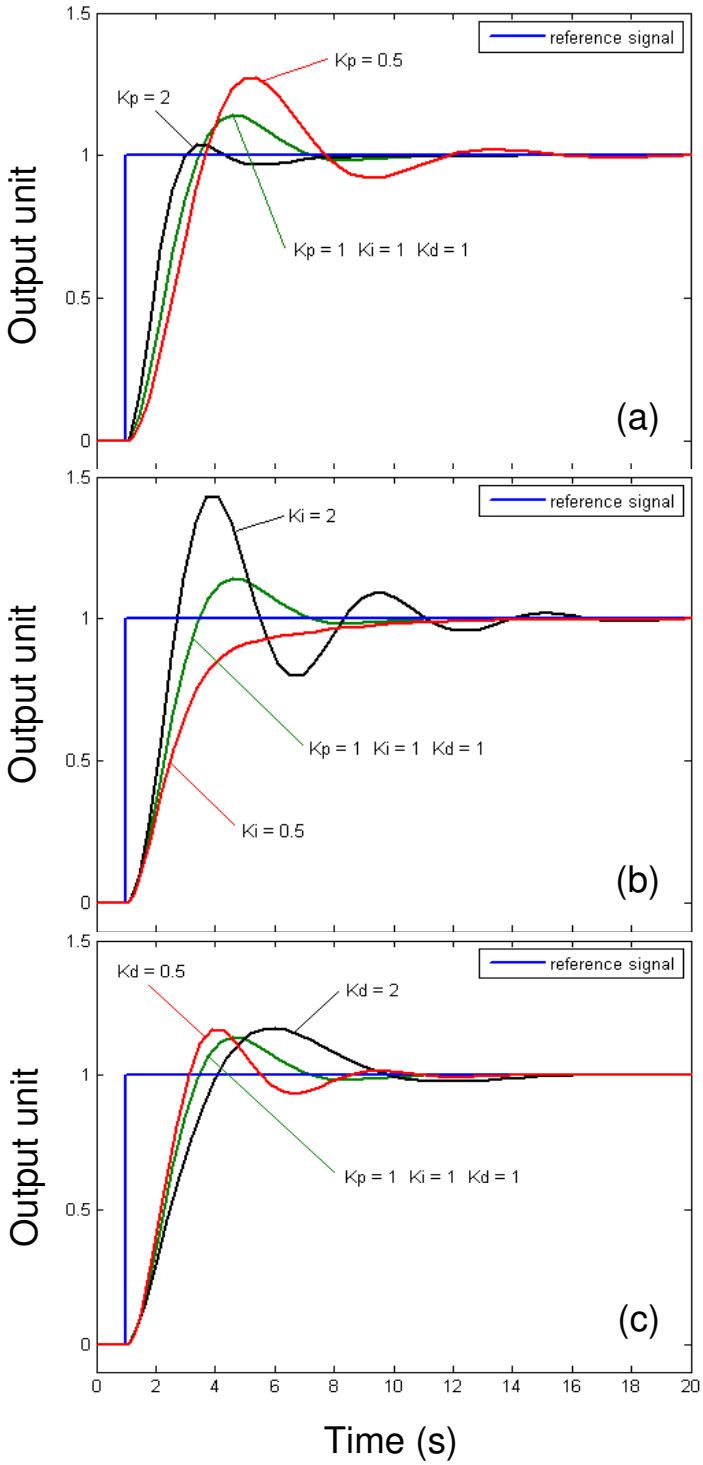


*Figure 3.5.4: Calibration of the PID controller in response to a reference signal. Plot of the output variable, in our case the temperature $T$ of the beam, as a function of time, (a) for three values of $K_P$ ($K_I$ and $K_D$ held constant); (b) for three values of $K_I$ ($K_P$ and $K_D$ held constant) and (c) for three values of $K_D$ ($K_P$ and $K_I$ held constant).*

Where $\tau$ is a dummy variable.

**The derivative term ($D_{out}$):** The rate of change of the process error is calculated by determining the slope of the error over time (i.e., its derivative with respect to time) and multiplying this rate by the derivative gain $K_D$. The derivative term is given by:

$$D_{out} = K_D \frac{de(t)}{dt}$$

These three terms, $P_{out}$, $I_{out}$ and $D_{out}$ are summed to calculate the temperature output of the PID controller. The final form of the PID algorithm is:

$$T(t) = K_P e(t) + K_I \int_t^0 e(\tau) d\tau + K_D \frac{de(t)}{dt}$$

Larger values of $K_P$ typically mean faster response since the larger the error (fig. 3.5.4 (a)), the larger the proportional term compensation. An excessively large $K_P$ will lead to process instability and oscillation. The integral term accelerates the movement of the process towards set-point and eliminates the residual steady-state error that occurs with a proportional-only controller. Large values of $K_I$ imply that steady-state errors are eliminated more quickly (fig. 3.5.4 (b)). The derivative term slows the rate of the output. Larger values of $K_D$ decrease overshoot, but slows down transient response and may lead to instability due to signal noise amplification in the differentiation of the error (fig. 3.5.4 (c)).

### 3.5.6 Residual pressure deposition mode

The beam lines are equipped with a by-pass system that introduces gas directly into the three chambers and particularly into the second chamber. This system allows to introduce into the UHV chamber a controlled residual pressure of a specified gas to deposit on the surface of the sample holder. This mode of deposition is called *residual pressure* or *background* deposition mode. The pressure obtained by this mode in the main chamber is higher than what can be obtained through the jets only (in fact through 2 diaphragms instead of 3).

## 3.6 Resonance Enhanced Multiphoton Ionisation (REMPI 2+1)

The goal of this diagnostic is to measure the rovibrational populations of molecules desorbing from the surface. For this purpose, a UV laser beam passes through two $MgF_2$ windows parallel to the surface of the sample holder. This beam is focalised ($f \sim 350$ mm) several mm away from the surface, to better probe the molecules desorbing from the surface. The molecules

present in the focalisation zone are ionised by REMPI then detected with the TOF mass spectrometer positioned in front of the surface. The molecules are selectively ionised by resonance depending on the chosen wavelength and on their quantum state.

### 3.6.1 REMPI ionisation

The energy necessary to ionise a hydrogen molecule from the ground state is 15.42 eV. This energy corresponds to a photon with a wavelength $\lambda = 80$ nm. But for $\lambda$<200 nm the air constituents like $N_2$ and $O_2$ absorb the UV and impose to create and propagate the UV light under vacuum (VUV). To circumvent this difficulty, it is possible to overcome the ionisation threshold by using the simultaneous absorption of 3 photons of wavelengths greater than 200 nm and that are very weakly absorbed in the air. The absorption cross sections of three photons are however very small ($\sim 10^{-83}$ cm$^6$) and impose of intense laser power.

For certain values of $\lambda$, the cross section of the process is highly increased. These wavelengths are those of which the energy of two photons corresponds to the energy necessary to a transition towards an excited electronic state (see fig. 2.2.1. These wavelengths are called resonant. For parity reasons, this intermediate level is reached by the absorption of two photons (cross section $\sim 10^{-48}$ cm$^4$). Taking into account the flux of photons necessary to perform the absorption or the first two photons, the absorption step of the third photon is saturated. The complete process, called REMPI 2+1, has the same efficiency of the two photons process.

The two photons excited electronic state for $\lambda$ ranging from 200 to 300 nm is that of the double minimum called E,F. The transitions are called E,F(v',J')←X(v",J"), where the vibrational and rotational quantum numbers are (v",J") for the starting state X and (v',J") for the finish state E,F.

The principle characteristics of the process are the following:

- The selection rules are $\Delta$ J=J'−J"= −2, −1, 0, 1 or 2. Only the transitions corresponding to the branch Q ($\Delta$J= 0) are observed, the others being 30 times weaker (Pozgainer et al., 1994).
- Ionisation is selective with respect to v" and J". This means that the number of created ions for a resonant wavelength depends on the population of the starting state X(v",J").
- The ionisation probability of a molecule depends on the square of the laser intensity. To increase the ionisation efficiency, the laser is therefore focalised in the detection zone.

The intensity of the signals depends on the number of molecules present in the ionisation zone, on their rovibrational state and on the laser intensity and its focalisation.

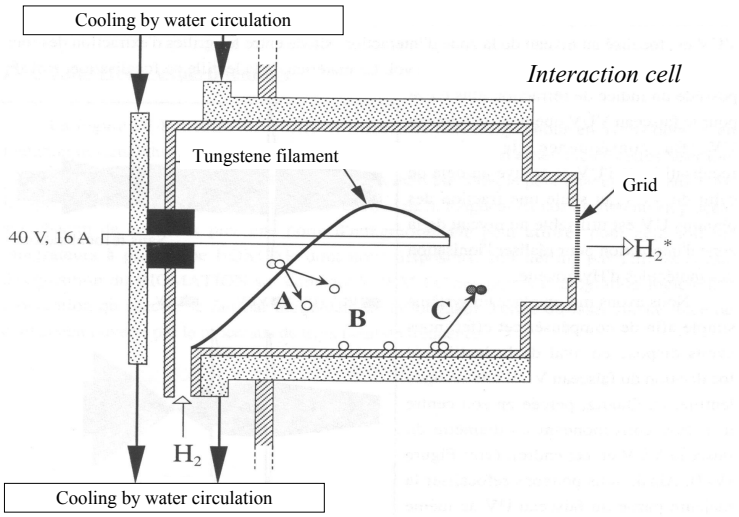


*Figure 3.6.1: Source of molecular hydrogen. The Tungstene filament is heated following Joule's law. Molecules hitting the filament are either rovibrationally excited or dissociated. The formed atoms recombine on the walls of the source at 290 K and form excited molecules (Malmasson, 1994).*

## 3.6.2 REMPI spectra

### Experiments

The spectral lines of molecular hydrogen corresponding to the transitions E,F(v',J')←X(v",J") are very distant from each other. In the UV range, the first rotational lines are distant of 0.2 nm whereas those of the vibrational lines are distant of ∼7 nm. Their width is determined by the resolution of the laser which is typically equal to 2 pm. Since the signals coming from the surface can be quite weak, it is essential to place the laser at the exact wavelength of the transition, ±5 pm. We used an additional set-up to locate the $H_2$ and $D_2$ rays in order to prepare for future experiments.

This set-up is under secondary vacuum and is composed of a TOF mass spectrometer and a lamp that excites the incoming molecules before they reach the mass spectrometer (fig. 3.6.1). The source was developed during the thesis of Malmasson (1994). It is constituted of a very hot tungsten filament (T>1000 K) that excites molecules in high rotational and vibrational states via two mechanisms: direct excitation by collision with the filament and dissociation by collision with the filament (A) followed by recombination on the cold walls of the source (B and C).

**REMPI spectrum E,F(0,J')←X(2,J")**

Figure 3.6.2 shows a typical example of a REMPI spectrum (2+1) for vibrationally excited $D_2$ molecules. We observe the Q branch in the first five rotational levels, which allows us to characterise the distribution of the rotational population of level v=2.

**Determination of populations:**

The multiphotonic probabilities of transition are intrinsically quasi-identical from one line to another in the same Q branch (Hönl-London factors $\approx 1$) (Rinnen et al., 1991; Pozgainer et al., 1994). We can therefore obtain the relative population of each level, on condition to correct the measured amplitudes of the laser intensity variations from a ray to another. This correction is applied by dividing the amplitude of each line by $I^{\alpha}$ where $I$ is the laser intensity measured when recording the spectrum. The order $\alpha \approx 1.6$ of the transition was measured at the maximum of each line by varying the laser intensity.

If the probed molecules are in thermodynamic equilibrium, the population distribution is that of Boltzmann

$$N(v,J) = \frac{g_n(2J+1)e^{-E_{v,J}/k\mathrm{T}}}{\sum_{v,J} N(v,J)}$$

where $E_{v,J}$ is the energy of the level (v,J)
and $g_n$ the degeneration of the same level

It is then possible to attribute a temperature by drawing an excitation diagram; by calculating $\log\left[N(v,J)\sum N(v,J)/(g_n(2J+1)\right]$ as a function of E(v,J), we obtain a straight line with a slope equal to $-E/kT$ (figure 3.6.3). The measured temperature (362 K) can seem surprising at the beginning since it is close to the ambient temperature while the detected molecules are in vibrational state v=2 which corresponds to a vibrational temperature greater than $10^4$ K. One should keep in mind that the excitation lamp does not produce a gas in thermodynamic equilibrium. Consequently, we observe a mechanism of collisional de-excitation on the cold walls of the lamp, more efficient for rotational de-excitation than for vibrational de-excitation. This experiment with the lamp was only used as a source of excited molecules to adjust the laser wavelength with respect to the REMPI transitions.

## 3.7 Recent modifications

Mid 2009, after the repairing of the QMS, changes have been brought to its implementation. It is still installed on a rotatable stage but off-axis so that it could be used facing the sample while depositing gases. Cuts have been made on the side of the QMS head solid block to allow beam 2 not to hit

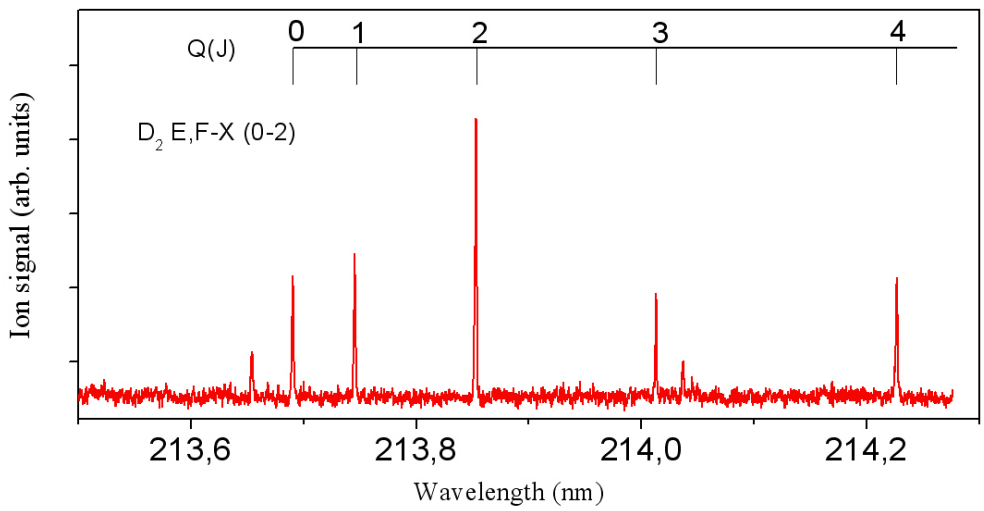


*Figure 3.6.2: REMPI spectrum for molecular deuterium. $D_2$ spectrum obtained with the lamp at hign temperature at a pressure of $10^{-6}$ mbar.*

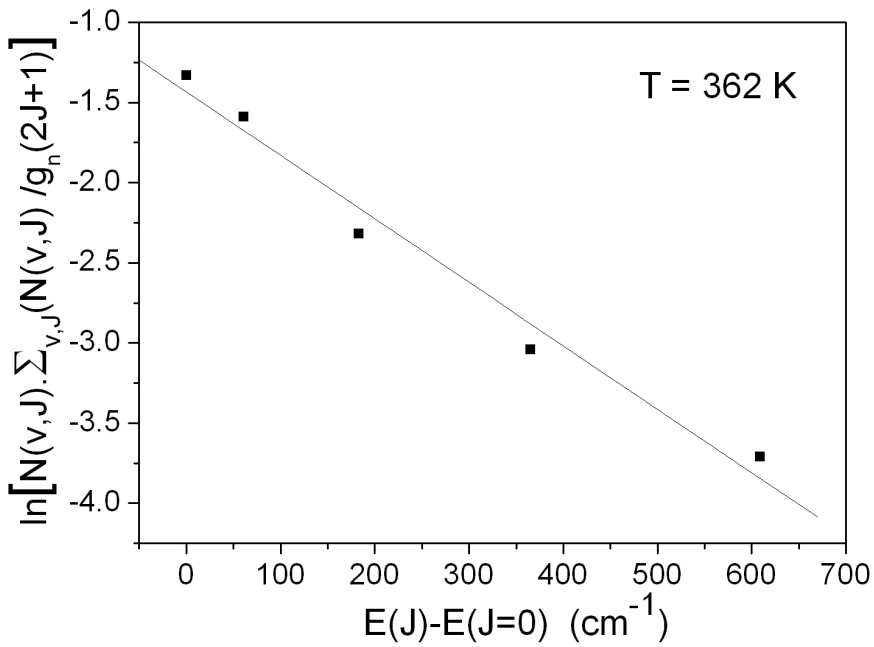


*Figure 3.6.3: Excitation diagram for $D_2$, v= 2. A linear function fit of the measured points gives a rotational temperature of 362 K.*

it. In addition, as indicated in figure 3.4.2, the entrance and exit apertures of the QMS head are now identical. Dissociation rates of the beam can still be monitored, rotating the stage as before.

End of 2009 a Fourier Transform Reflection Absorption InfraRed Spectrometer (FT-RAIRS) has been implemented on FORMOLISM and is now being tested. A Brucker Tensor 27 Commercial Spectrometer used in remote detection mode is connected to the main chamber through KBr windows by means of two boxes containing the optics and the detector. The copper sample is identical except that it is now gold-plated for infrared reflection. Some of the experiments I will present in the following chapters would be completed by the use of the RAIRS.

This is a great advantage but at the expense of the minimum QMS to sample distance now fixed at $\sim$5 mm.

# Chapter 4

# TPD technique and growth of solid water ice films

## 4.1 TPD experiments

### 4.1.1 Introduction

The Temperature Programmed Desorption (TPD) technique was first described by Redhead (1962), but was first applied to study catalytic reactions of Ethylene on alumina surfaces by Amenomiya & Cvetanovic (1963) who became later on the pioneers of the technique. This technique is also referred to as Thermal Desorption Spectroscopy (TDS). It uses either quadrupole or TOF mass spectroscopy.

TPD experiments consist, after deposition of atomic or molecular species, reacting or not, onto a well defined surface, on increasing the temperature of the surface by imposing a linear heating ramp. When the surface reaches a specific temperature, called the desorption temperature (different for each adsorbed species), the energy transferred to the adsorbed species causes it to desorb into the gas phase. During the heating phase, a QMS is placed near the surface to record the mass spectra of one or several desorbing species.

The TPD technique is an important method for determining the kinetic parameters of desorption processes of molecular species. Since each species has its unique desorption temperature range, the TPD spectra provide information on the adsorption energies of species on a given surface. It also give us information on the amounts of adsorbed molecules on the surface from the intensity of the TPD peaks and the total amount of adsorbates is given by measuring the area under the TPD profiles since this area is proportional to the specific surface of the ice. As we will show it later on, the adsorption energy range is highly dependent on the substrate as well as on the amount or the number of layers deposited.

If the desorption temperature of a certain species is already known, any change in the shape of the TPD spectrum or in the shift of the maximum desorption temperature provides information on the morphology of the surface.

For example in our case, the desorptions of $H_2$ or $O_2$ from an ice surface tell us if the ice is crystalline or amorphous, if it is non-porous amorphous or porous amorphous and if it presents a high or a low porosity (*cf* subsection 4.2.7).

TPD experiments might also trigger diffusion and reactions between species present on the surface, right before the desorption process takes place. New molecules can then be detected.

The following examples are $H_2$ desorption equations for three different routes:

$$\text{Ex. 1:} \quad {H_2}^{ads} \xrightarrow{desorption} {H_2}^{gas}$$

$$\text{Ex. 2:} \quad 2\,H^{ads} \xrightarrow{associative\,des.} {H_2}^{gas}$$

$$\text{Ex. 3:} \quad 2\,H^{ads}_{immobile} \xrightarrow{diffusion} 2\,H^{ads}_{mobile} \xrightarrow{formation} {H_2}^{ads} \xrightarrow{desorption} {H_2}^{gas}$$

The first example is an elementary desorption, in which adsorbed molecules are released into the gas phase. The second example shows an associative desorption that corresponds to the $H_2$ formation reaction on the surface. Such reaction can be composed of sub-processes detailed in the third example. In this case, the TPD induces a diffusion process that makes atoms mobile on the surface; it is followed by a reaction between atoms; and it might end with the recapture process of molecules for which the desorption process does not immediately follow the formation (depending on the morphology of the surface). The TPD experiment is therefore an "indirect" tool to study the reaction mechanisms taking place on the surface.

### 4.1.2 Desorption and TPD from a unique energy

The dynamics of desorption from a surface follows an Arrhenius Law described by the Polanyi-Wigner equation which expresses the desorption rate $r$:

$$r(N, E_{\mathrm{a}}, \mathrm{T}) = -\frac{\mathrm{d}N}{\mathrm{d}t} = AN^n \mathrm{e}^{-E_{\mathrm{a}}/k_B \mathrm{T}} \tag{4.1}$$

The different terms being:

| | |
|---|---|
| $E_{\mathrm{a}}$ | the adsorption energy |
| $N$ | the total number of adsorbates on the surface |
| $n$ | the order of the desorption kinetics |
| $A$ | the efficiency factor of the desorption |
| T | the temperature of the surface |
| $k_B$ | the Boltzmann constant |

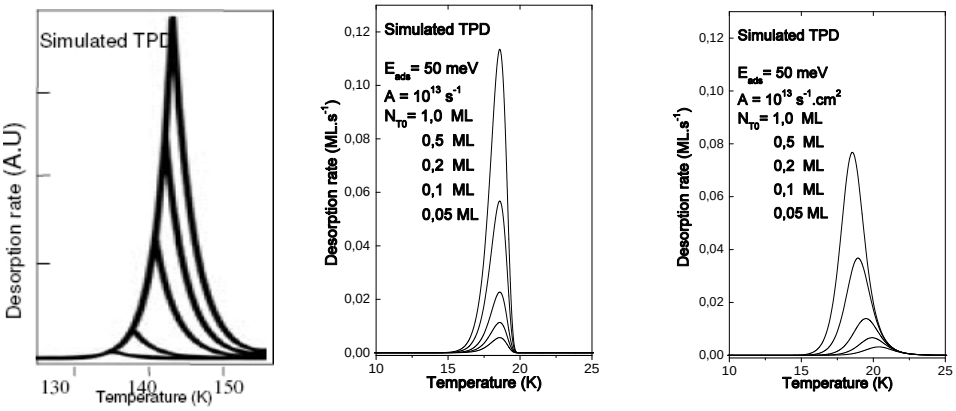


(a) Zero order TPD (b) First order TPD (c) Second order TPD

*Figure 4.1.1: Typical desorption profiles of TPD of orders 0, 1 and 2.*

One should note that the term $r/N^n$ is a desorption frequency and therefore represents the inverse of the residence time $\tau_{des}$ on the surface. Energies here are positive towards the bottom of the adsorption wells, the zero energy corresponding to a free particle. In calculations, this scale inversion is compensated by the $-$ sign that precedes the energies.

During a TPD, the desorption is caused by the linear rise of the temperature. Time and temperature scales are then related by:

$$\mathrm{T} \quad = \quad \mathrm{T}_0 + \beta t \quad \text{with } \beta = \frac{\mathrm{dT}}{\mathrm{d}t} \tag{4.2}$$

In general, all our temperature programmed desorptions are done with a heating ramp $\beta$=10 K/min.

In practice, species that desorb are detected with the QMS. The signal intensity is proportional to $r$ because we are in an efficient pumping regime ($\frac{\mathrm{d}N}{\mathrm{d}t} \ll v_{pump}$) (See chapter 3).

The order $n$ corresponds to the number of reactants necessary to activate the desorption. It corresponds, in general, to stoechiometric coefficients in the desorption equations. Figures 4.1(a), 4.1(b) and 4.1(c) show TPDs of zero, first and second order kinetics.

The zero order reflects desorption kinetics independent of the amount of available adsorbates. This regime corresponds to the multilayer desorption of an adsorbate, where the number of surface elements ready to desorb is almost constant during a relatively long period of time. The exponential growth predominates and allows reaching desorption rates of several ML.s$^{-1}$ before reaching the last layer.

The first order corresponds to the desorption of an adsorbate whose coverage rate is lower or equal to one monolayer. First order TPDs of different adsorbed quantities present maxima aligned at the same temperature.

The second order corresponds to an associative desorption. This desorption requires the encounter of two adsorbed species. This encounter has a probability that depends on the coverage rate squared. The maximum of a second order TPD shifts towards low temperatures when the adsorbate quantity increases. This feature, resulting from the combination of the two effects involved in TPDs, the increase of the reactivity with the temperature and the decrease of the number of reactants present on the surface during desorption, can be illustrated by calculations. Noticing that at temperature $\mathrm{T}_m$ of the desorption maximum $\mathrm{d}^2N/\mathrm{d}t^2 = 0$, the adsorption energy $E_a$ is obtained by differenciating the equation 4.1:

$$E_a = k\mathrm{T}_m^2 \frac{A}{\beta} n N^{n-1} e^{-E_a/k_B \mathrm{T}_m} \tag{4.3}$$

For a unique adsorption energy $E_a$ and a second order kinetics ($n = 2$), the increase of $N$ implies therefore a decrease of $\mathrm{T}_m$.

If the efficiency factor $A$ is known, it is possible to calculate the adsorption energy, if it is unique, from equation (4.3). The energy appears however in both members of the equality. It is therefore necessary to state hypothetically a value for this energy and find the convergence towards a value confirming this equality using an iterative method (Attard & Barnes, 1998).

But in general the hypothesis of a unique energy is not confirmed. It is a particular case for the adsorption of molecular hydrogen on ice surfaces where the energy depends on the coverage. More complex analysis methods should then be put in place.

### 4.1.3 Specificity of molecular hydrogen on amorphous ice at low temperatures

Figure 4.1.2 shows the desorption of molecular hydrogen from a porous amorphous water ice substrate exposed to increasing doses. The way the tails of the curves join up together at higher temperatures with a shift of the desorption maximum towards low temperatures when the initial coverage increases recalls a second order dynamics. It is however difficult to justify a second order desorption mechanism for the desorption of molecules that were simply adsorbed on the surface from the gas phase. There exist associative adsorption mechanisms of $H_2$ on copper for example (Michelsen & Auerbach, 1991), that lead to an associative desorption of second order, but the adsorption energies are in this case typically of the same order of the molecular binding energy, around some eV, and imply then a temperature $> 900$ K. Another explanation for the curves in figure 4.1.2 should then be found, referring more realistically to a first order desorption.

First order desorption is characterised by a narrow peak whose maximum increases vertically with the dose. To interpret the molecular hydrogen TPDs as a signature of a first order desorption, we should consider a distribution

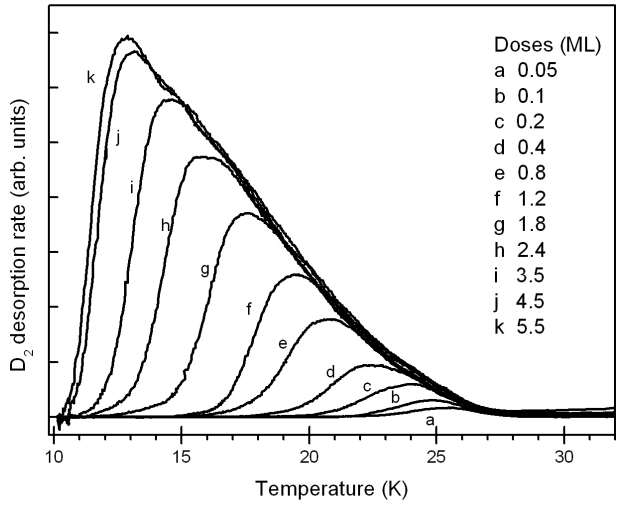


*Figure 4.1.2: Typical TPD of molecular hydrogen adsorbed on a porous amorphous water ice substrate of* 10 *ML prepares at 10 K. Desorption of growing doses of* $D_2$ *from right to left* $(0,05 - 5,5$ *ML).*

of binding energies and not a unique binding energy (Amiaud, 2006). The desorption energy $E_a$ and the efficiency factor $A$ depend then on the amount of adsorbates $N$ and equation 4.1 can be re-written as follows:

$$r(N, \mathrm{T}) = -\frac{\mathrm{d}N}{\mathrm{d}t} = A(N)N\mathrm{e}^{-\frac{E_\mathrm{a}(N)}{k\mathrm{T}}} \tag{4.4}$$

It is then the shape of the function $E_a(N)$ that determines the general profile of the desorption. We can distinguish two regimes when looking at the desorption curves of molecular hydrogen in figure 4.1.2: on the one hand, the starting front lines whose form, specific to the adsorbed dose, is very steep at high doses, tend towards a limit corresponding to a saturation, and is very soft when the dose decreases; on the other hand, the desorption tails are superposed, whose form is independent of the dose and seem to characterise the surface.

The inverse problem, consisting on finding the function of the adsorption energy distribution $E_a(N)$ from a TPD, is not trivial. We can already notice that, in particular, several values of the parameters $[A(N),\ E(N)]$ can obviously give the same desorption rate than in equation 4.4.

Amiaud (2006) has developed an original inversion method in his Ph.D. thesis. It is based on a model in which desorption takes place from an energy distribution of several adsorption sites. The originality comes from the fact that the distribution of molecules in the different adsorption sites depends on Fermi-Dirac statistics dependent on the temperature. The idea of using a set of adsorption sites is suggested by the amorphous nature of the surface and

the large number of possible geometries for the water molecules to interact with their neighbors on the surface of the sample. The reason for using a statistical description resides in the importance of the diffusion of molecules that are exploring systematically a large number of sites on the surface before desorption. A very simple estimation of the number of diffusion hops before desorption can be found as follows: the mean diffusion time is given by the Langmuir law:

$$\tau_{diff} = \left(Ce^{-E_{diff}/k_B\mathrm{T}}\right)^{-1} \tag{4.5}$$

where $C$ is the efficiency factor and $E_{diff}$ is the diffusion barrier. By assuming that $E_{diff} = E_a/3$, and that $C = A$, we can estimate that the number of hops before desorption is equal to

$$n = \frac{\tau_{des}}{\tau_{diff}} = e^{2E_a/3k_BT} \tag{4.6}$$

At T= 10 K, considering $E_a = 30$ meV, the number of hops is $n = 10^9$. We conclude therefore that molecules are very mobile on the surface, and that there is a permanent redistribution of molecules during desorption.

The desorption curve derived from the model can then be adjusted to fit the experimental curve by a least squares method, which allows to obtain physical parameters and quantities that describe the experimental results.

### 4.1.4 Importance for the sticking

In figure 4.1.2, we irradiate a *p*-ASW ice surface to increasing doses of $D_2$. The TPD profiles obtained give us an idea of the coverage rate of the surface and the sticking coefficient of molecules. In figure 4.1.3 we plot the areas under each TPD profile as a function of the $D_2$ exposition dose. We obtain the proportion of molecules that stuck onto the surface before the heating ramp. Figure 4.1.3 is divided into two parts, a linear increase and then a plateau. The first part indicates that the amount of molecules that were previously stuck onto the surface is proportional to the amount of molecules that the surface was exposed to. We then deduce that in the range of doses 0.05–3 ML, the $D_2$ sticking coefficient is constant. The plateau at the end is explained by the saturation of the surface. In fact, as the amount of molecules present on the surface increases, the adsorption energy of the available sites decreases, thus decreasing the residence time of molecules on the surface (see Chapter 4 for more details). This gives us also information on the saturation coverage of the surface which is reached for a dose of ∼3 ML of $D_2$ on *p*-ASW ice surfaces (∼0.45 ML on *np*-ASW)

### 4.1.5 Importance for the mobility

The TPD technique was also used to prove the mobility of cold atomic deuterium on *p*-ASW ice surfaces (This will be presented and discussed in full

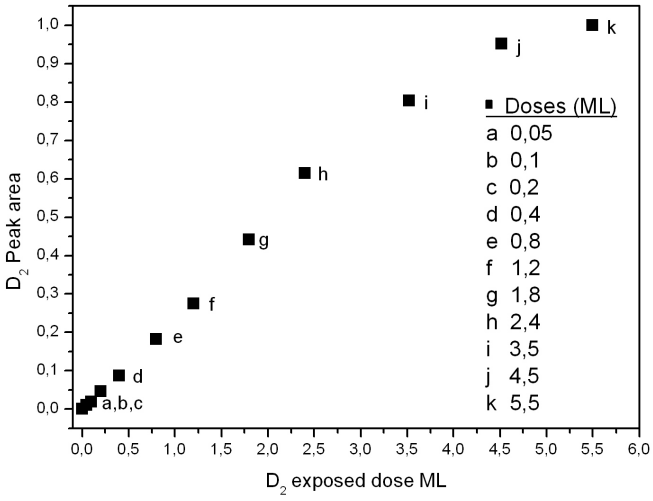


*Figure 4.1.3: Area under the $D_2$ TPD profiles of fig. 4.1.2 as a function of the $D_2$ exposed dose (0.05-5.5 ML).*

details in chapter 5). As a summary, by observing the decrease of the area under each $O_2$ TPD profile for increasing doses of D atoms we concluded that the amount of $O_2$ available on the surface is decreasing before the heating phase. This is explained by the consumption of $O_2$ molecules by D atoms on the surface of the ice.

## 4.2 Water ice substrates

### 4.2.1 Introduction

Water ice exists in a large number of phases (Table 4.2.1), depending on the temperature and the pressure under which it is formed. Here I will briefly present three different types of water ice structures:

- The most common form of water ice is the hexagonal crystalline ice, found everywhere in the biosphere. All ices grown in general at a temperature higher than ∼160 K present a hexagonal crystalline structure.
- The cubic crystalline form is a metastable variant of water ice, where the oxygen atoms are arranged in a diamond structure. This ice is formed between 130–160 K. It is occasionally present in the upper atmosphere.
- The amorphous ice has no crystalline structure. It exists in two forms: compact (non-porous) or porous. Other nomenclatures exist in the literature: high-density amorphous (HDA) and low-density amorphous (LDA) ice. Amorphous ice can be formed either by extremely quick cooling of liquid water or by depositing water vapour on very cold substrates under ultra-high vacuum conditions.

In the following sections, I will discuss in detail the characteristics in volume and surface of amorphous water ice, the previous works done by some teams on the subject and the method we have chosen to grow such ice films in our laboratory. I will finish this chapter with the importance of hydrogen in probing the ice surface morphology.

### 4.2.2 Growth and porosity

In FORMOLISM at LERMA-LAMAp laboratory, amorphous ice is obtained under ultrahigh vacuum by slow deposition of water vapour (typically $< 0,5$ MLs$^{-1}$) on a cold surface. This amorphous ice might present a porous structure if the temperature of the surface is lower than 120 K, cubic crystalline if it is between 120 K et 160 K and hexagonal crystalline above 160 K. These transitions are clearly visible on a water TPD curve by the appearance of bumps that interrupt the exponential growth of the zero order desorption (fig. 4.2.1).

Amorphous ice can have different porosities depending on the deposition flux, the temperature of the sample-holder and the deposition technique (Mayer & Pletzer, 1986; Pletzer & Mayer, 1989; Martin et al., 2002b,a). The work of Kimmel et al. (2001a,b) proposes a description of the ice like a molecular assembly that presents cavities linked to each other and open to the outside. The construction of these cavities can be explained by the following mechanism: when a water molecule is added to the structure subject

*Table 4.2.1: The different phases of crystalline ice (Petrenko & Whitworth, 2002). Two amorphous forms also exist, namely high-density and low-density ASW, but they are not listed here. (See text).*

Structures of the crystalline phases of water

Parameters are at the temperature $T$ and pressure $p$ stated. All densities given are for $H_2O$

| Ice | Crystal system | Space group | Proton order? | Molecules per cell | $T$ (K) | $p$ (GPa) | Density (Mg m$^{-3}$) | Cell parameters (Å) | Reference |
|---|---|---|---|---|---|---|---|---|---|
| Ih | Hex. | $P6_3/mmc$ | N | 4 | 250 | 0 | 0.920 | $a=4.518$, $c=7.356$ | Röttger *et al.* (1994) |
| Ic | Cubic | Fd3m | N | 8 | 78 | 0 | 0.931 | $a=6.358$ | Kuhs *et al.* (1987) |
| II | Rhomb. | $R\bar{3}$ | Y | 12 | 123 | $0^{\dagger}$ | 1.170 | $a=7.78$, $\alpha=113.1°$ | Kamb (1964) |
| III | Tetrag. | $P4_12_12$ | N | 12 | 250 | 0.28 | 1.165 | $a=6.666$, $c=6.936$ | Londono *et al.* (1993) |
| IV | Rhomb. | $R\bar{3}c$ | N | 16 | 110 | $0^{\dagger}$ | 1.272 | $a=7.60$, $\alpha=70.1°$ | Engelhardt and Kamb (1981) |
| | | | | | 260 | 0.50 | 1.292 | | Lobban *et al.* (1998) |
| V | Monocl. | A2/a | N | 28 | 98 | $0^{\dagger}$ | 1.231 | $a=9.22$, $b=7.54$, $c=10.35$, $\beta=109.2°$ | Kamb *et al.* (1967) |
| | | | | | 223 | 0.53 | 1.283 | | Kamb *et al.* (1967) |
| VI | Tetrag. | $P4_2/nmc$ | N | 10 | 225 | 1.1 | 1.373 | $a=6.181$, $c=5.698$ | Kuhs *et al.* (1984) |
| VII | Cubic | Pn3m | N | 2 | 295 | 2.4 | 1.599 | $a=3.344$ | Kuhs *et al.* (1984) |
| VIII | Tetrag. | $I4_1/amd$ | Y | 8 | 10 | 2.4 | 1.628 | $a=4.656$, $c=6.775$ | Kuhs *et al.* (1984) |
| IX | Tetrag. | $P4_12_12$ | Y | 12 | 165 | 0.28 | 1.194 | $a=6.692$, $c=6.715$ | Londono *et al.* (1993) |
| X | Cubic | Pn3m | n/a | 2 | 300 | 62 | 2.79 | $a=2.78$ | Hemley *et al.* (1987) |
| XI | Ortho. | $Cmc2_1$ | Y | 8 | 5 | 0 | 0.934 | $a=4.465$, $b=7.858$, $c=7.292$ | Line and Whitworth (1996) |
| XII | Tetrag. | $I\bar{4}2d$ | N | 12 | 260 | 0.50 | 1.292 | $a=8.304$, $c=4.024$ | Lobban *et al.* (1998) |

$^{\dagger}$Samples recovered at low temperature.

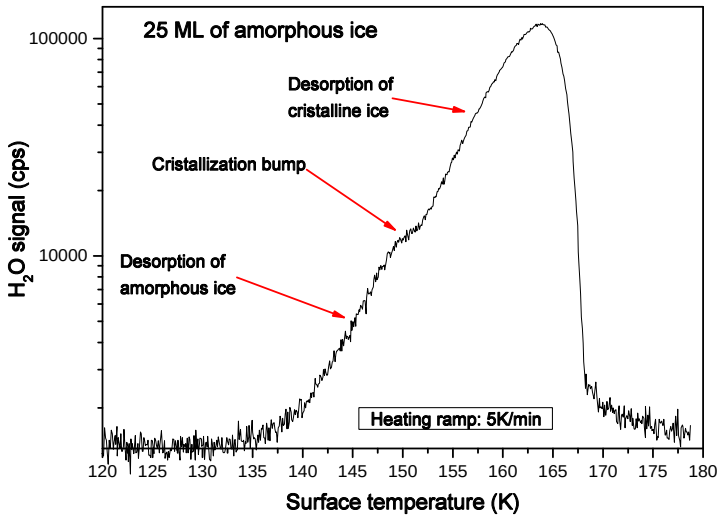


*Figure 4.2.1: TPD of a porous amorphous water ice on a logarithmic scale. The desorption is interrupted and marks a plateau (or break) during the phase transitions*

to a low thermal activity, its movement is rapidly blocked and then it cannot leave the impact zone in order to fill the gaps of the structure.

This description lies on TPD experiments done on water ice formed by a molecular beam whose incidence angle is well defined. By confronting these results with ballistic simulations, they show the effect resulting from the variation of the incidence angle. A normal incidence favours uniform distribution of molecules on the surface and produces a non-porous ice. An oblique incidence favours the aggregation of molecules on the unevenness of the structure. They, therefore, create pillars and walls that lead to the formation of cavities and therefore the growth of a porous ice. Below 90 K, Kimmel et al. (2001a,b) prove that the background deposition technique, corresponding to a set of random incidence angles, builds an ice that presents very high porosity (Fig. 4.2.2). This porosity is all the more high as the temperature is low. It is in particular very high around 10 K and can then present an apparent surface as thick as some thousands of $m^2$ for 1 g of water deposited on 1 $m^2$. The residual pressure deposition is the technique that we have often used.

The degree of porosity of an initially porous ice can also be modified. The apparent surface of the ice decreases when the temperature of the surface increases. This effect is explained by the collapse of the pores and by the diffusion of water molecules. Is is also possible to prepare an ice film by deposition at a high temperature ($>$ 100 K), which avoids the formation of

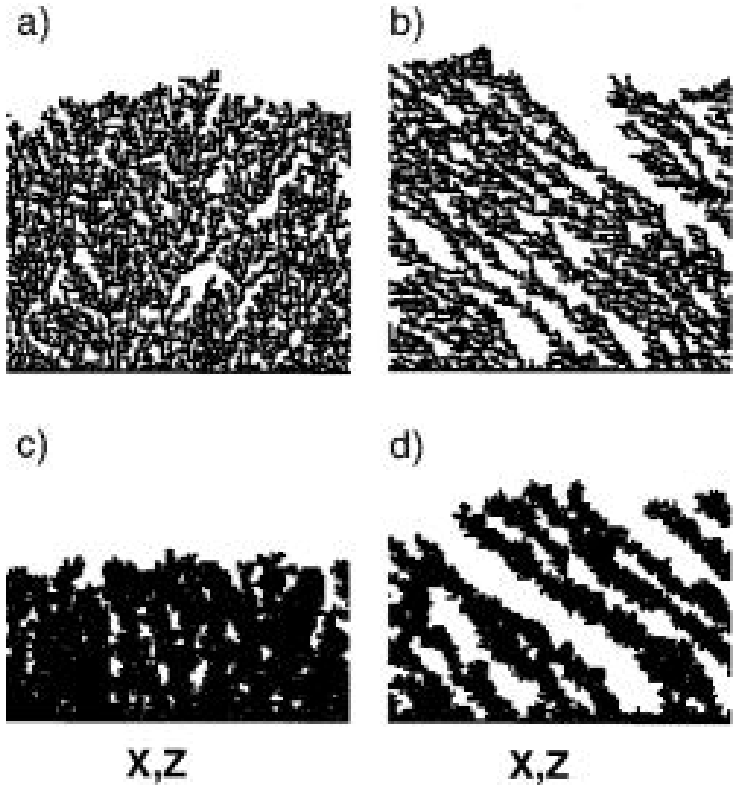


*Figure 4.2.2: Two-dimensional ballistic deposition simulations of 50 ML films. (a) θ=0°, no annealing. (b) θ=70°, no annealing. Large, angular pores develop in the film due to the shadowing effect. (c) θ=0°, eight annealing steps. (d) θ=70°, eight annealing steps. Annealing eliminates many of the smaller pores, but the large pores associated with the shadowing remain (Kimmel et al., 2001b).*

pores, then cool down the surface to a low temperature (10 K) and thus obtain a non porous structure. Nevertheless, the two methods are not perfectly equivalent and the obtained structures, even if non-porous, will not be necessarily identical, because, at the same temperature, the diffusion of molecules is more efficient during the construction of the ice than the diffusion that can take place in the core of an already formed structure. In fact, it is proved that pores can still subsist in an ice structure prepared at 20 K and then annealed to 120 K (Kimmel et al., 2001a).

### 4.2.3 Volume density

**Optical measurements** The average density of porous ices has been deduced from optical interference measurements (Dohnalek et al., 2003). These measurements confirm the interpretation of Kimmel et al. (2001a,b) by showing that the average density decreases when the effective interaction surface with the gas increases. This corresponds to an increase of the empty space in the thickness of the ice.

**Measurements by X-ray diffraction** On the other hand, slow electron and X-ray diffraction methods allow to measure the density following the criteria of the mean difference between the closest oxygen atoms. This method measures a density that we can qualify as intrinsic. When water vapour is deposited at 77 K on an inert surface, the ice formed has a density of $0,94 \pm 0,03$ g.cm$^{-3}$ and is called low-density ice (LDI) (Narten et al., 1976; Mayer & Pletzer, 1986). A different high-density (1.1±0.1 g.cm$^{-3}$) amorphous (HDI) form was first obtained by Narten et al. (1976) by depositing water vapour at ∼10 K. Their X-ray diffraction experiments showed that the increased density of this form of ice, with respect to the low-density amorphous ice, was due to the presence of water molecules at distances between those of the first and second nearest neighbour at the interstitial site of the solid structure. These two characteristics are similar to those of the high-density amorphous ice formed by compression of the hexagonal ice (Jenniskens et al., 1995). However, these ices are not equivalent (Guillot & Guissani, 2003, 2004). Between 38 K and 68 K, the high-density amorphous ice undergoes an irreversible transition towards a form whose diffraction figure is similar to those of the low-density amorphous ice (Jenniskens et al., 1995).

The high-density amorphous ice is potentially more important than low-density ice in astrophysics, because infrared spectra of water vapour deposited on low-temperature substrates provide the best fit to the 3.07 $\mu$m observed ice band (Jenniskens et al., 1995).

Experiments on the morphological differences between ASW and crystalline ices were done by Vichnevetski et al. (2000). They measured the electron-stimulated desorption of metastable molecular nitrogen from $N_2$ condensed on the ice and related the variation of the signal detected to the vari-

ation in density of $N_2$ molecules at the surface of a porous water film. By growing their ice at 20 K, they obtained an amorphous water ice sample that contains a large number of pores (diameter range ∼15–20 Å (Langel et al., 1994; Mayer & Pletzer, 1986)).

**Molecular dynamics** Molecular dynamics calculations confirm these X-ray measurements (Jenniskens et al., 1995; Guillot & Guissani, 2004). They describe the amorphous ice as a random network of hydrogen bonds, in which, some stay dangling, contrary to the cubic ice structure where 4 water molecules are arranged by a tetrahedral configuration of hydrogen bonds. Moreover, these calculations indicate that at very low temperatures, a $5^{th}$ water molecule is added in the nearest neighbouring and thus creates an additional distortion and additional dangling OH bonds.

### 4.2.4 Condition of the surface

The X-ray measurements mentioned above are only sensitive to the volume properties of the ice. Other measurements have been carried out by Parent et al. (2002) to study the surface properties by the PSD-NEXAFS (Photon Stimulated Desorption-Near-Edge Xray Absorption Fine Structure) technique. This work was done by comparing the total electron yield (TEY) spectrum which is bulk sensitive, with the total ion yield (TIY) spectrum which is sensitive to the surface structure. Their results indicated that when the ice is grown at 38 K, it has a dense network of cylindrical pores of 20 Å of diameter separated by 6 Å. These authors also find that at this temperature (38 K) the bulk of the ice has a high-density amorphous structure, and is subject to structural transformation from HDI to LDI when annealed to 55 K. But the bulk structure stays unchanged (no measurable change in the intermolecular O–O distance) after that, when annealed from 55 K to 147 K.

However, they find that the surface suffers structural rearrangement more than the bulk when annealed. The surface becomes smoother and the number of OH bonds increases. Contrary to the bulk, the surface is subject to morphological change when annealed from 38 K to 147 K (the bulk from 38 K to 55 K only). At the surface of the ice film, the $H_2O$–$H_2O$ intermolecular distance increases from 2.77 Å to 2.80 Å. This means that at 147 K, the structure of the surface can be quite different from that of the bulk of the ice film.

Worth to note that, in 2006, the same authors published an article in which they demonstrate that HDI is not the natural form of water ice at low temperatures. HDI is, in fact, the form that takes LDI when it is irradiated (Laffon et al., 2006).

Studies ranging from molecular dynamics simulations on water clusters to infrared spectroscopy experiments allow us to learn more on the ice

*Table 4.2.2: The different names of ASW ice phases grown at different surface temperatures.*

| $T_s$ (K) | 0 K | 10 K | 38 K | 70 K | 120 K | 147 K |
|---|---|---|---|---|---|---|
| Ice morphology | High Density Ice (HDI) | | Low Density Ice (LDI) | | | Crystalline ice |
| | Highly porous ice | | Porous ice | | Non-porous ice | Crystalline ice |

surface condition. Water aggregates simulated by molecular dynamics (Buch, 1992) reproduce, on the one hand, the intrinsic properties stated earlier. They reveal, on the other hand, the properties of the surface. The structure of a $(H_20)_{450}$ aggregate simulated at 10 K shows a very irregular surface that presents an important proportion of molecules that are not entirely coordinated. IR spectroscopy analysis, sensitive to the dangling OH bonds on the surface (Buch & Devlin, 1991; Devlin & Buch, 1995) strengthen this point of view. Performed at a low temperature on $H_2$ saturated ice surfaces (Rowland et al., 1991; Hixson et al., 1992), they reveal a high abundance of bi- or tri-coordinated molecules on the surface. In these experiments, the analysed surface is the effective surface of interaction with $H_2$, including the pores that can be accessible from the gas phase via diffusion.

The nomenclatures found in the literature are not always clear, and misunderstanding might arise from the several names that can have the different phases of amorphous solid water ice (Table 4.2.2). Intuitively, high-density ice makes us think that it is compact (non-porous) amorphous ice, but in fact is porous. And inversely, low-density ice makes us think that it is porous but in fact is non-porous amorphous solid water ice. To remove all misunderstanding, we will use the nomenclatures porous and non-porous ASW for ices grown at 10 K and 120 K respectively in all the following chapters of this PhD thesis.

### 4.2.5 Interaction with the gas phase

Several TPD experiments showed that the ice structure can adsorb and trap a large variety of gas[1]. The most volatile species (Ar, $H_2$, CO, $N_2$, $O_2$, $CH_4$) principally desorb below 60 K. Yet two other desorption signatures are observed, at temperature independent of the considered gas, the first at 140 K and the second at 160 K. These signatures are attributed to the release of gas pockets trapped in the pores that were closed during the annealing. At 140 K, the crystallisation causes the evacuation of the gas by a phenomenon

[1]Bar-nun et al. (1985); Bar-Nun et al. (1987); Laufer et al. (1987); Notesco & Bar-Nun (1997); Collings et al. (2003, 2004)

called *molecular volcano*. At 160 K, the remaining gas is released during the desorption of the ice itself.

This capacity to trap gases is highly dependent on the porosity and on the intensity of the adsorption bond of the gas concerned. It is demonstrated that molecular hydrogen is particularly very faintly adsorbed on the surface, that it diffuses efficiently on the sample (Rowland et al., 1991) and that it desorbs before the surface temperature reaches 30 K. Thus it leaves the sample almost completely before the pores close due to the irreversible transition that takes place between 38 and 68 K. It does not involve, during the annealing, neither a *molecular volcano* nor a co-desorption.

In conclusion, if the amorphous structures of water ice at low temperature are often separated into two categories (improperly designated by *low*- and *high-density*), this classification does not permit to characterise precisely the surface condition that plays a predominant role in our gas-surface interaction studies. In particular, the volume reconstruction of the ice starting from 35-40 K naturally leads to a continuous reconstruction of the surface condition with the temperature, until its crystallisation. The use of molecular hydrogen, that desorbs entirely below, constitutes therefore an excellent tool to probe the surface of amorphous ice at very low temperatures by the TPD technique without affecting too much the structure of the ice sample obtained at 10 K (*cf.* section 4.2.7).

### 4.2.6 Procedures for growing ASW ices

Before studying, in the following chapters, the interaction and the formation of molecular hydrogen on amorphous water ice surfaces, one should first know and control the morphology of the ice surface. As explained above, molecular hydrogen constitutes an excellent probe of the characteristics of amorphous ice. In this section I will describe in detail the procedures that we follow in our laboratory to grow porous and non-porous ASW ices substrates and how molecular deuterium is used to probe their porosity.

#### Non-porous (*np*-) ASW

After making sure that the base pressure in the UHV chamber is stable ($10^{-10}$ mbar) and that the temperature of the sample holder is set to 120 K, we place the capillary vaporiser 20 mm in front of the surface of the sample and we introduce water vapour into the chamber measuring a partial pressure of $\sim$2 $10^{-9}$ mbar. In general, for experiments that should be done on non porous ice surfaces, we grow 100 or 150 ML of *np*-ASW at a speed of $\sim$0.33 ML.s$^{-1}$. After that we close the valve, put the vaporiser in its initial position and wait for the base pressure in the UHV chamber to go down to $10^{-10}$ mbar ($\sim$15 min) before cooling down the surface temperature to 10 K and start our experiments. The *np*-ASW deposition can be monitored using the QMS (fig. 4.2.3).

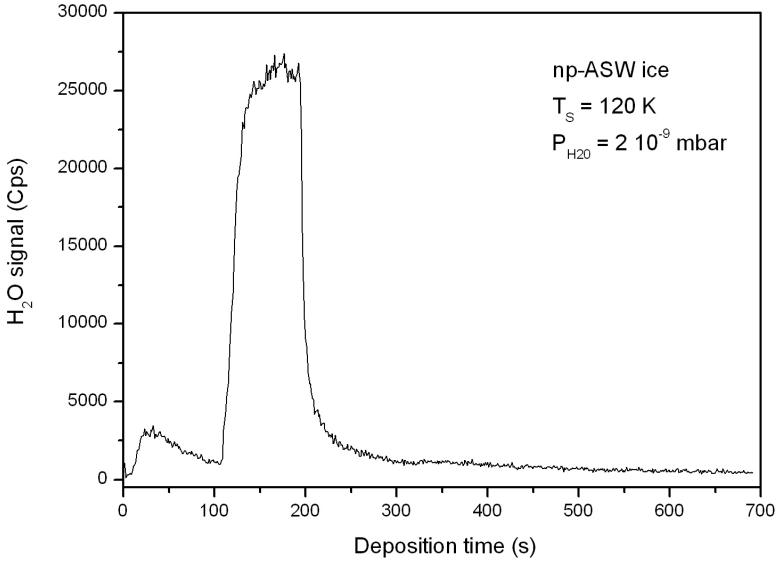


*Figure 4.2.3: Example of $H_2O$ deposition to grow np-ASW ice. In general, the deposition time depends on the number of monolayers that we want to grow. The surface temperature is set to 120 K and the $H_2O$ partial pressure in the chamber to $\sim$2 $10^{-9}$ mbar.*

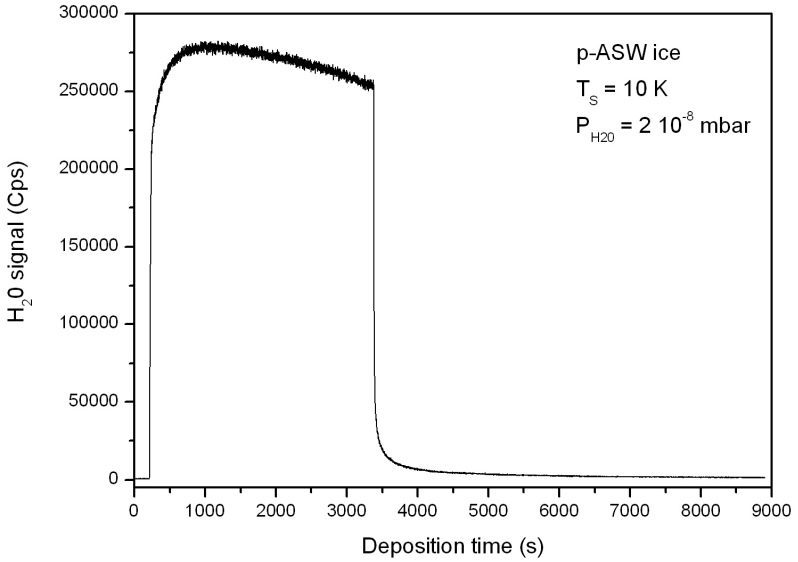


*Figure 4.2.4: Example of $H_2O$ deposition to grow p-ASW ice. The deposition time depends on the number of monolayers that we want to grow (monitored by a software applet connected to the pressure gauge). The surface temperature is set to 10 K and the $H_2O$ partial pressure in the chamber to $\sim$2 $10^{-8}$ mbar.*

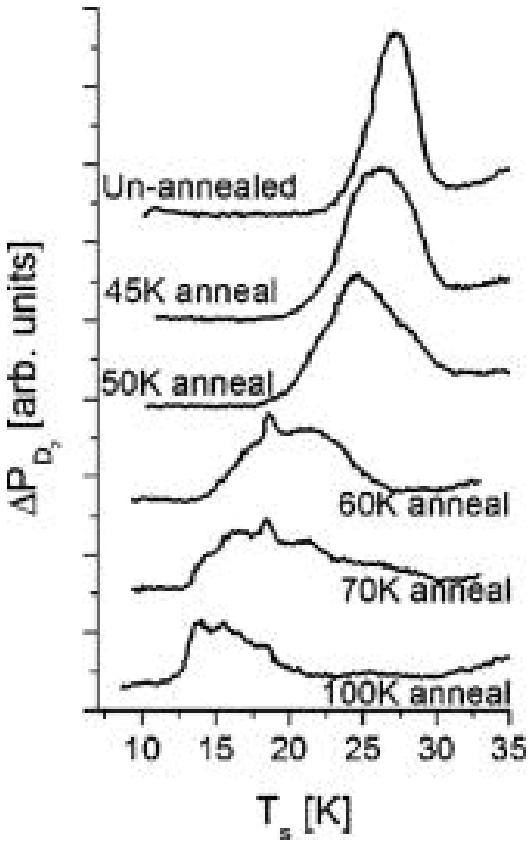


*Figure 4.2.5: TPD spectra of 1.2 ML of $D_2$ from 2000 ML ASW films grown at 10 K and subsequently annealed to the stated temperatures. The employed ramp rate is 0.5 K/s. The same amount of $D_2$ (1.2 ML) deposited on ∼2000 ML of p-ASW ice films grown at 10 K and annealed to different temperatures. We see that even if the ice was grown highly porous (at 10 K), its porosity is reduced considerably depending on the annealing temperature. From Hornekær et al. (2005).*

**Porous ($p$-) ASW**

- **Background deposition**
  As explained above, to grow a $p$-ASW ice substrate, the temperature of the sample holder is set to 10 K and the vaporiser is located in its remote position. Water vapour is introduced into the UHV chamber with a partial pressure of $\sim$2 $10^{-8}$ mbar enabling to grow $\sim$1 ML every 5 minutes. After growing the selected number of $p$-ASW monolayers the valve is closed and we wait for the base pressure to reach $\sim 10^{-10}$ mbar again ($\sim$1 hour). The $p$-ASW ice monolayers are counted by a software applet connected to a pressure gauge and the evolution in time of the deposition is recorded with the QMS (fig. 4.2.4).

- **Direct deposition**
  We can also grow $p$-ASW ice substrates by the direct deposition method that we normally use to grow $np$- asw ice. We work under the same residual $H_2O$ vapor pressure ($\sim$2 $10^{-9}$ mbar) in the chamber and the close vaporiser position. The only difference is that the surface temperature is held at 10 K. We use this method when we want to grow very thick $p$-ASW ice films (250 ML) which would require a too long time with the background deposition method (*cf* Chapter 5).

### 4.2.7 Probing the morphology of the ice

The ice surface, maintained at 10 K, is exposed to a certain amount of $D_2$. The deposited quantity is measured the same way it is done for the water deposition, by integrating the pressure measured in the chamber with the software applet. After the deposition, the QMS is positioned in front of the surface. This operation takes $\sim$1 minute during which the temperature of the surface is maintained at 10 K. The surface is then heated following a linear heating ramp of 10 K/min up to 32 K. During the heating phase, the QMS is set to record the desorption signal of $D_2$ (4 uma).

For each water ice structure, $D_2$ desorption has a unique TPD profile and a unique desorption temperature as can bee seen in figure 6.2.1. The higher the porosity, the higher the desorption temperature. This is a normal behaviour since highly porous ice has more binding sites with higher binding energies. This leads to molecules staying longer on the surface, and thus delaying their desorption to higher surface temperature. In general, we characterise the porosity of the ASW ice by comparing the $D_2$ TPD profile from $p$-ASW to that of $D_2$ desorbing from $np$-ASW ice films grown at 120 K.

## 4.3 Conclusion

In the first part of this chapter I have discussed the TPD technique and its importance as a diagnostic for the sticking and the mobility of hydrogen

on amorphous water ice surfaces. The second part deals with the different characteristics of amorphous water ice, in volume and surface. I have also discussed the methods we use in the LERMA-LAMAp to grow *p*- and *np*-ASW ice films and the importance of hydrogen and the TPD technique to probe the morphology of these types of films.

# Chapter 5

# Sticking of atomic and molecular hydrogen on icy grains

## 5.1 Introduction

For a gas-grain reaction to take place, such as $H_2$ formation or hydrogenation/deuteration of molecular species, the first step is that at least one of the reaction partners would stick on the surface of the grain. In this chapter I will present the experimental results we have obtained for the sticking of both hydrogen and deuterium molecules on the surface of non-porous ASW ice substrates at 10 K.

But before going into more details in the subject, an important remark concerning the definition itself of the sticking coefficient should be presented for the sake of clarification.

## 5.2 The sticking process

The definition of the sticking coefficient used by Govers et al. (1980) is that molecules that stick on the surface are those that become in thermodynamic equilibrium with it, and then become thermalised to the temperature of the surface. Govers et al. (1980) were in fact capable of measuring the energy transfer between the beam and the surface, with a bolometer, during the collision of molecules with the sample. Thus, they make the distinction between molecules that bounce on the surface and those that become adsorbed and therefore stick. Nevertheless, desorption may occur immediately after adsorption, the difference between bouncing molecules and those following the adsorption-desorption process is established through the amount of energy transferred to the surface of the bolometer.

In our experiments it is not possible to make such distinction because we are not able to measure the beam-surface energy transfer. One should

*Table 5.3.1: comparison between hydrogen (deuterium) sticking coefficients obtained by CMD and classical trajectory simulations done by several teams.*

| $E_i$ (K) | Buch & Zhang (1991) | | Takahashi *et al.* (1999) | Al-Halabi & van Dishoeck (2007) |
|---|---|---|---|---|
| | H atoms | D atoms | H atoms | H atoms |
| 10 | -- | -- | 1 | 0.97 |
| 50 | 0.85 | 0.92 | -- | -- |
| 90 | 0.53 | 0.90 | -- | -- |
| 100 | -- | -- | 0.98 | 0.72 |
| 140 | 0.26 | 0.51 | -- | -- |
| 200 | 0.11 | 0.38 | -- | -- |
| 300 | 0.051 | 0.19 | -- | 0.37 |
| 350 | -- | -- | 0.53 | -- |
| 600 | 0.004 | 0.043 | -- | 0.13 |

also note that this distinction is not very clear since the bouncing molecules might also transfer some of their kinetic energy to the surface without being adsorbed and thermalised. This quantity, represented by a factor called the accommodation coefficient, is the ratio of the average energy actually transferred between the surface and the impinging gas molecules scattered by the surface, to the average energy which would theoretically be transferred if the impinging molecules reached complete thermal equilibrium with the surface.

Whereas in our case, the definition we adopt for the sticking coefficient is given by the number of molecules that stay on the surface during a residence time $\geq$1 s compared to the number of molecules arriving at the surface during the time of the experiments. The lowest measurable time in our experiments being $\sim$1 s.

## 5.3 Previous works

The sticking of atomic and molecular hydrogen on amorphous ice surfaces that mimic the mantles covering the interstellar dust grains has been extensively studied theoretically over the years, but few experimental works have been carried out on the subject so far.

### 5.3.1 Theoretical

The first theoretical studies on the sticking of hydrogen on water ice surfaces were those of Hollenbach & Salpeter (1970), followed by Burke & Hollenbach (1983) and Leitch-Devlin & Williams (1985). But the first intensive calculations on this subject were those of Buch & Zhang (1991). These authors studied the sticking of H and D atoms on an amorphous water ice cluster made of 115 $H_2O$ molecules by using classical molecular dynamics (CMD) simulations. They calculated the sticking coefficients $S_E$ for several beam kinetic energies $E$ ranging from 50 K to 600 K (Table 5.3.1). The

fitting of their results was done using the simple exponential decay function $S_E=e^{-E/E_0}$, where $E$ is the kinetic energy of the incident gas and where $E_0$=200 K for D atoms and $E_0$=102 K for H atoms (∼2 times lower than that of D). These authors also found that some impinging atoms travel significant distances (∼20 Å) on the water cluster while losing their kinetic energy. This high mobility may affect significantly the reactivity of atoms on the grains by enhancing the probability for an atom to encounter other already adsorbed ones.

Masuda et al. (1998) and Takahashi et al. (1999b) also studied the sticking of atomic hydrogen on amorphous ice slab made of 1000 $H_2O$ molecules (40Å×40Å×20Å) at 10 K using CMD calculations. They calculated the sticking probability of hydrogen atoms as a function of the incident beam temperature (Table 5.3.1) and found that, for a kinetic temperature $E_i$=10 K, the sticking probability of a hydrogen atom is unity. They also found that, before the atom sticks, it travels 60Å on the amorphous ice surface during 1.7 ps before it gets thermalised and adsorbed.

In the same context, classical trajectory (CT) calculations were done by Al-Halabi & van Dishoeck (2007). Their results on the sticking probability of H atoms on ASW ice (6 bilayers of 360 $H_2O$ molecules) at 10 K were fitted by the same decaying exponential function used by Buch & Zhang (1991). These authors found that $S=\alpha e^{-E/E_0}$, where $E$ is the kinetic energy of the incident atoms, $E_0$=300 K (whereas 102 K for Buch) and $\alpha$=1 is a constant parameter. With these fitting function and parameters, the sticking coefficient of an H atom with $E$=10 K at a surface of 10 K is equal to $S$=0.97 and for $E$=300 K, it is equal to $S$=0.37 (Table 5.3.1).

### 5.3.2 Experimental

To date, only one set of experiments on the sticking of atomic hydrogen on amorphous water ice surfaces can be found in the literature (Schutte et al., 1976) and few experimental works have been conducted to measure the sticking coefficients of hydrogen and deuterium molecules on the same ice surfaces at low temperature (Govers et al., 1980; Hornekær et al., 2003).

Schutte et al. (1976) and Govers et al. (1980) presented results on the variation of the sticking and accommodation of atomic hydrogen (deuterium) with respect to the surface coverage with molecular hydrogen (deuterium). They both used bolometer experiments under ultra-high vacuum to study the sticking coefficient on a surface of a cryodeposit of $H_2O$, $N_2$ and Ar in the 3.5 K–15.5 K range. They found that at a surface temperature ≤10 K, the sticking coefficient of impinging $H_2$ molecules on an $H_2$ free surface increases slightly, if any, when the surface temperature decreases. This means that the sticking coefficient is rather independent of the surface temperature in the 3.7 K–10 K range. These authors also found that the sticking probability is highly dependent on the $H_2$ coverage of the surface, and that it increases with the increasing amount of adsorbed $H_2$. Schutte et al. (1976) explained

this behaviour by the fact that when a particle of mass $m$ approaches a surface with a kinetic energy $E_i$, it is first attracted by a potential well and its kinetic energy becomes $E_i$+$E_a$, where $E_a$ is the adsorption energy. Then a hard collision occurs with the surface particles of mass $M$. The impinging particle sticks only if the amount of energy lost is higher than $E_i$. In fact, the probability for an inelastic collision with the surface is given by $P_S$=$1 - e^{\frac{-6m}{M}\frac{E_i+E_a}{\theta_D}}$, where the exponent is the Debye-Waller factor and $\theta_D$ is the Debye temperature[1] of the surface. It is clear that the sticking process becomes more probable if the $\frac{m}{M}$ ratio is high. In other words, we obtain the highest sticking probability when $m \approx M$. This explains why the sticking probability of hydrogen is enhanced when there are other adsorbed hydrogen on the surface.

Hornekær et al. (2003) studied the HD formation efficiency on both porous and non-porous ASW ice at 8 K using the TPD technique. Their formation rate is defined as $R_{HD}$=$\mu S_D \eta$, where $\mu$ is the fraction of newly formed HD that stays trapped in the pores of the ice surface, $S_D$ is the sticking coefficient of impinging atoms (considered the same for both H and D atoms) and $\eta$ is the probability for an adsorbed atom to recombine with another adsorbed partner. These authors measured the sticking coefficient of $D_2$ with the King & Wells method (see section 5.4) and found it to be equal to $S_{D_2}$=0.2±0.15 for a $D_2$ beam at room temperature on *np*-ASW ice at 8 K. However, no direct measurements of the sticking coefficient of H or D atoms were made.

To my knowledge, the present experimental study constitutes the first measurement of the sticking coefficient variation of molecular hydrogen and deuterium as a function of the beam temperature.

## 5.4 The experiment

The water film is composed of 100 ML of non-porous ASW ice grown by depositing water vapour on the copper sample-holder maintained at 120 K and then cooled down to 10 K. We then irradiate the ice substrate by a pure and stable beam of $D_2$ (∼1 $10^{-4}$ mbar in the first chamber) or $H_2$ (∼6 $10^{-4}$ mbar in the first chamber)[2] at a certain beam temperature. During the irradiation, the signal of $D_2$ ($H_2$) in the main chamber is measured in real-time mode with the QMS in its remote position.

The experiment, shown in figure 5.4.2, is divided into four steps:

[1]The Debye temperature of a cubic solid of an edge $L$ is given by $\theta_D$=$\frac{hc_s}{2Lk_B}\sqrt{\frac{6N}{\pi}}$, where $h$ is Planck's constant, $k_B$ Boltzmann's constant, $c_s$ is the velocity of sound (or of phonons in the solid) and $N$ is the number of atoms or molecules.

[2]The pressure of $H_2$ is higher than that of $D_2$ in order to have a better S/N ratio due to the fact that $H_2$ is the major pollutant of the UHV chamber.

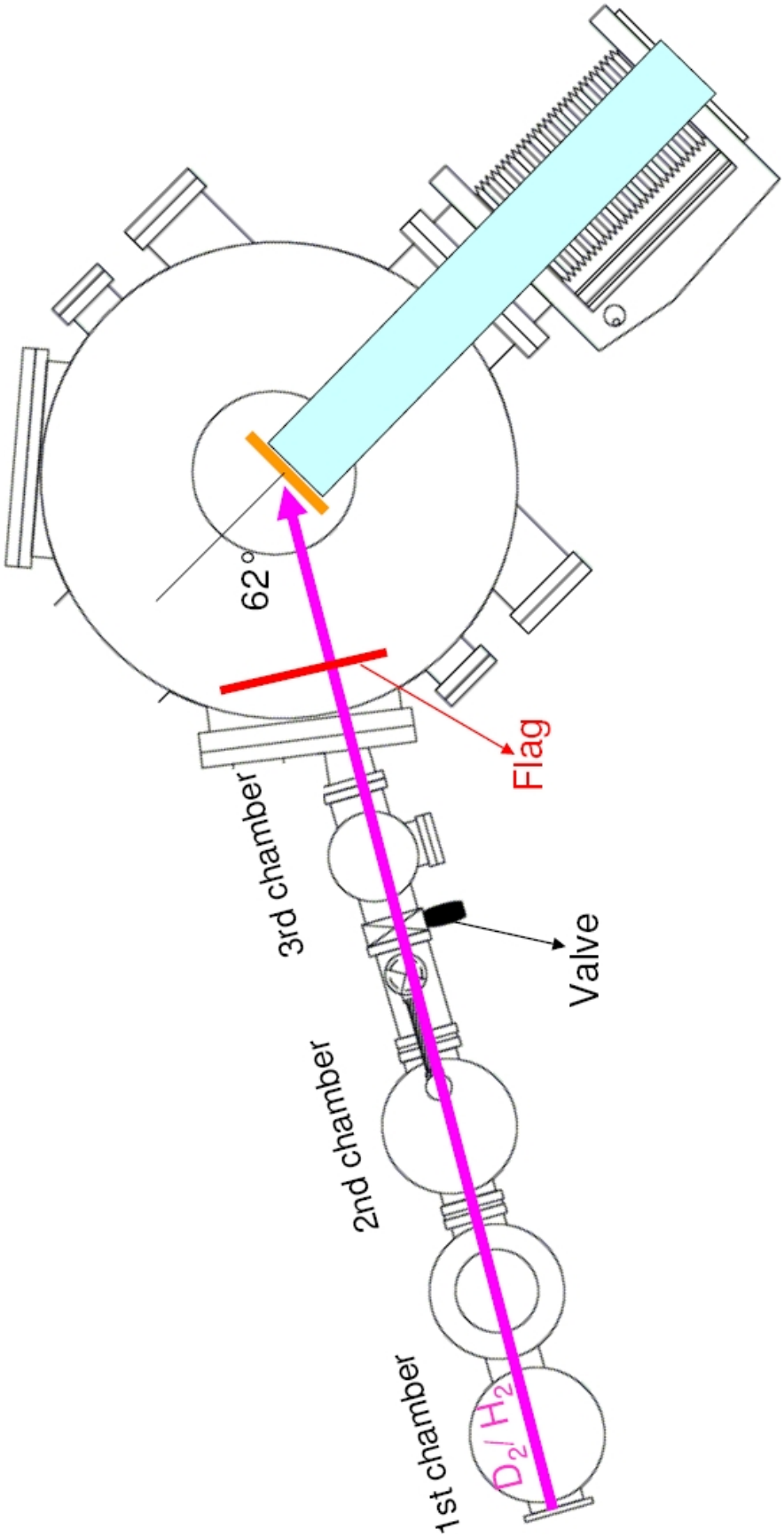


*Figure 5.4.1: A scheme of the first beam line showing, in black, the valve between the second chamber and the third chamber and, in red, the metallic flag that intercepts the $D_2$ or $H_2$ beam in the UHV chamber. The beam has an angle of 62° with respect to the normal to the surface of the sample holder.*

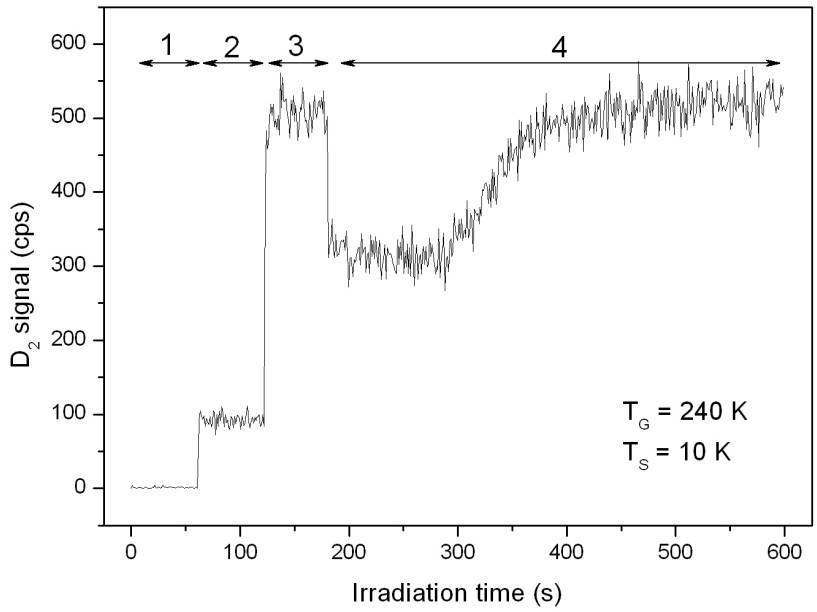


*Figure 5.4.2: A typical sticking experiment. The signal is that of the mass 4 ($D_2$) detected by the QMS during the irradiation of the surface with $D_2$ molecules.*

1. We start monitoring the signal for 60 seconds before introducing any $D_2$ ($H_2$) into the UHV chamber.

2. Then we introduce $D_2$ ($H_2$) by background, in order to measure the S/N ratio, by opening halfway the valve between the second and the third chamber, and by intercepting the beam in the main chamber with the metallic flag (fig. 5.4.1). This way we insure that no molecules reach directly the surface. In this step we measure the background pressure induced by the diffusion of molecules through the differentially pumped beam.

3. In the third step, the flag still intercepting the beam , we open wide the valve for additional 60 seconds to have a full indirect flux of $D_2$ ($H_2$).

4. After that, the flag is removed allowing the beam to hit the surface. This fourth step shown in figure 5.4.3 is known as the King & Wells method (King & Wells, 1972). It can take up to 600 seconds and is divided into 3 steps:

During the first $\sim$ 100 seconds of exposure (step (A) in fig. 5.4.3), the $D_2$ ($H_2$) signal in the UHV chamber decreases almost linearly. After that it presents a rapid rise (step (B) in fig. 5.4.3) and then reaches a plateau after

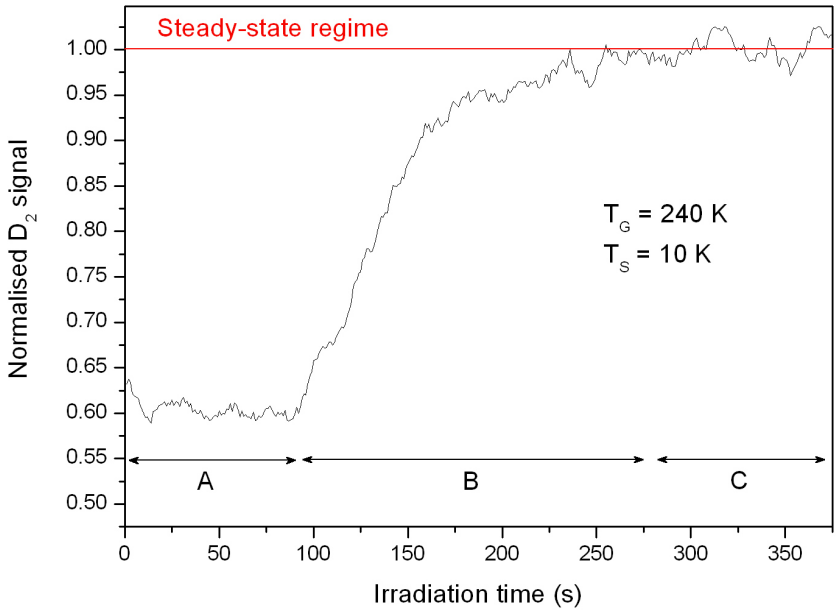


*Figure 5.4.3: King and Wells experiment. This figure constitutes the last part of the previous figure after signal smoothing (15 points/s). Time t=0 corresponds to the removal of the flag and the curve is normalised with respect to the average value of the final plateau. This $D_2$ signal can be divided into three steps as explained in detail in the text.*

$\sim$ 200 seconds (step (C) in fig. 5.4.3). This plateau stays constant as long as the beam flux is maintained, which means that we have reached a steady state regime. The signal intensity in this steady state regime is the same as that measured when the surface is at 30 K, when no molecules can stick on the surface, or when the flag is intercepting the beam (step 3 in fig. 5.4.2), prohibiting the molecules from directly reaching the surface. This plateau can be interpreted as a regime in which, even if molecules are reaching the surface, none are sticking anymore on it. It corresponds, therefore, to a regime of a sticking coefficient equal to 0. It is a regime where the number of molecules hitting the surface is equal to the number of molecules leaving it. We can, therefore, deduce that the variation of the signal before the plateau, observed in the first $\sim$200 seconds, is the signature of molecules sticking on the surface.

The first part of the figure, where the signal decreases (A), corresponds to an increasing sticking coefficient. This behaviour was already observed by Govers et al. (1980) while conducting experiments using bolometers to measure the gas-surface energy exchange. These authors have thus concluded that the increase of the sticking coefficient is due to the increase in the number of molecules already adsorbed on the surface. Schutte et al. (1976) underlined that the mass of the adsorbed molecules play an important role in the sticking and adsorption process. In fact, when a gas phase $D_2$ ($H_2$) molecule impinges on a $D_2$ ($H_2$) already adsorbed on the surface, the accommodation is greatly enhanced, thus enhancing the sticking of the impinging molecule. After the first 100 seconds, the sticking coefficient stops increasing, which causes the signal to rise rapidly (B). This rise is due to molecules that begin to desorb from the surface because their residence time becomes close to the time between two arrivals of impinging molecules (Amiaud et al., 2007). The plateau, however, corresponds to a regime where the number of desorbing molecules is compensated by the number of molecules adsorbed on the surface, then keeping the amount of molecules present on the surface constant.

The curve in fig. 5.4.3 can be transformed in terms of an absolute sticking coefficient $S(t)$ as already measured by Amiaud et al. (2007). It is equal to:

$$S(t) = \frac{Y(\infty) - Y(t)}{Y(\infty) - B}$$

The measured yield $Y(t)$[3] of $D_2$ molecules at time $t$ is the sum of molecules reflected from the surface $R_f(t)$ and a constant background factor $B$ (step 2 in fig. 5.4.2). $B$ does not originate from the direct molecular beam, but from the diffusion from the third stage of the triply differentially pumped beam. $Y(t)$=$R_f(t)$+$B$. The sticking coefficient is equal to the ratio between the non-reflected part of the signal and the incoming flux $F$. As $F = Y(\infty) - B$, $S(t)$ becomes $S(t) = (F - R_f(t))/F$.

[3] $Y(t)$ is the average value of the first 20 s of the $D_2$ or $H_2$ yield.

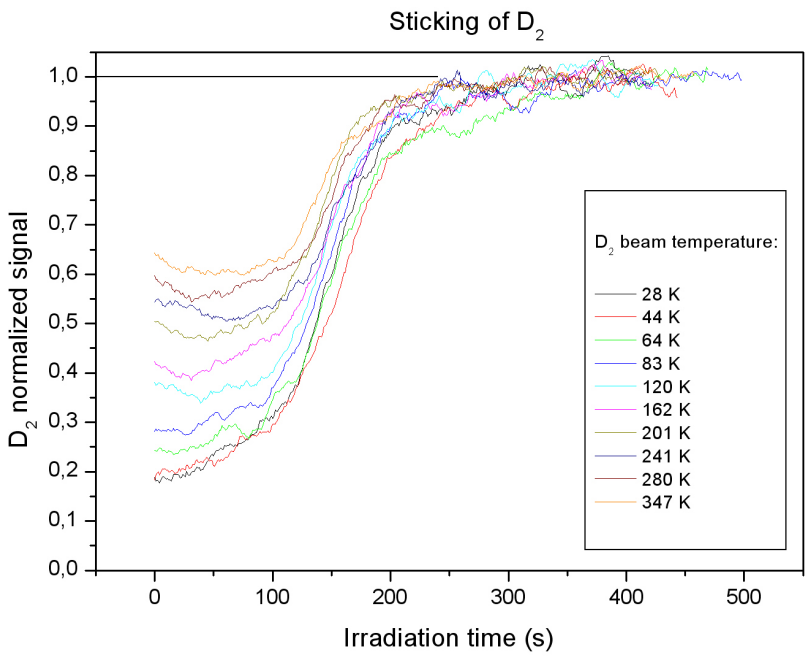


*Figure 5.5.1: King and Wells experiment repeated for several $D_2$ beam temperatures ranging from 28 K to 347 K. The decrease of part (A) of the signals with the beam temperature reflects the increase of the sticking coefficient of $D_2$ molecules on the surface.*

In the steady state regime $t = \infty$, the incoming flux is equal to the reflected molecules. Then, $F = R_f(\infty)$.

## 5.5 Variation of the sticking coefficient with the beam temperature

Following the same method of measurement, we repeated the same experiment for several beam temperatures ($T_G$) for $D_2$ as well as for $H_2$. Figure 5.5.1 shows the curves for each $T_G$, ranging from 28 K to 350 K, in the case of $D_2$.

Just by looking at this figure, we see very different behaviours from one curve to another. These behaviours can be interpreted as follows:

- The first remark concerns the starting point of each curve. We can clearly see that it is low for low beam temperatures and high when we work at higher beam temperatures. This is explained by the fact that for low $T_G$, the kinetic energy of molecules is low, making the collision with the surface less elastic, thus increasing the probability for a molecule to stick on the surface. The lower the beam temperature, the higher the sticking coefficient.

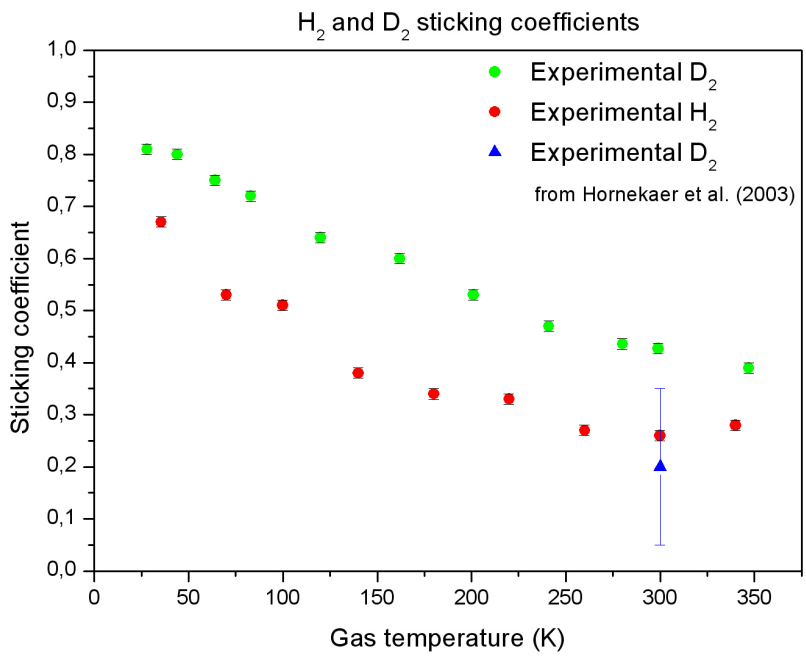


*Figure 5.5.2: Variation of the sticking coefficients of $D_2$ (green circles) and $H_2$ (red circles) as a function of the beam temperature $T_G$. The blue triangle represents the sticking coefficient for $D_2$ on the same type of ice obtained by Hornekær et al. (2003) shown for comparison. The error bars are about 5% of the sticking coefficient values. They are calculated by measuring the dispersion of several sticking coefficients obtained for the same beam temperature.*

- The second remark is that for high $T_G$, the signal starts with a linear decrease (in fig. 5.4.3 A) before it reaches the second stage. This behaviour disappears gradually when we work at lower beam temperatures. We have not yet understood the origin of this behaviour, but this disappearance of the linear decrease might be due to the fact that, at very low temperatures, the sticking coefficient is already at its maximum and cannot increase any further even with the presence of already adsorbed molecules on the surface. This makes the signal rise slowly right from the start before reaching the rapid increase of the second stage.

Using the formula of $S(t)$ taken from Amiaud et al. (2007), each curve in fig. 5.5.1 can be transformed in terms of an absolute sticking coefficient. Figure 5.5.2 shows the variation of the sticking coefficients of $D_2$ and $H_2$ as a function of $T_G$. We can see that the sticking coefficient of $D_2$ is higher than that of $H_2$, this is due to the fact that $D_2$ is heavier and has an adsorption

energy greater than that of $H_2$. An other information that can be obtained, is that our result at 300 K is slightly higher than the one obtained by Hornekær et al. (2003) where they derived, for $D_2$, a sticking coefficient S = 0.2± 0.15 for a beam temperature of 300 K. One should note that in their experiments, the incident beam is normal to the surface (0°) whereas in our case the beam has an angle of 62° (fig. 5.4.1). So no valid comparison can be made between the two measurements since the increase of the incidence angle can play an important role in enhancing the sticking probability of species.

## 5.6 The model

In this section I will describe the model that was developed in order to fit our experimental results obtained for molecular hydrogen and deuterium. It then extrapolates these results to find the sticking coefficients of hydrogen and deuterium atoms. This model was developed in collaboration with H. Bergeron from the LCAM (Orsay). The present work is a statistical model involving few physical parameters allowing to establish simple relations (1) between the sticking coefficients obtained for $H_2$ and $D_2$ and (2) between our results and those obtained by Buch & Zhang (1991) for the sticking coefficients of H and D atoms on water ice clusters.

### 5.6.1 Framework and hypotheses

In order to model the experimental data, we consider an amorphous surface with a temperature $T_S$=10 K. This surface is irradiated by a gas phase $G$ (in the half-space above the surface) composed of particles of mass $m$ at a temperature $T_G$. This gas phase is assumed to be in "pseudo-thermal" equilibrium: since the surface is irradiated with a beam, there exists a privileged direction in the velocity distribution, then a pure thermal distribution is not appropriated. Molecules that stick on the surface are considered to be bound to it by physisorption.

In our case the surface is amorphous. It is well-known that in the case of disordered surfaces the sticking probability is enhanced thanks to more complicated trajectories generated by the bumps of the surface (Hollenbach & Salpeter, 1970; Tully, 1981). The disorder of the surface is represented (statistically speaking) by a family of cells $C$ that have different properties each. And $S_C$ is the sticking probability of a particle hitting the surface in cell $C$. Each cell is characterised by a phenomenological velocity $c(m, C)$ (depending *a priori* on the mass of impinging particles).

### 5.6.2 The sticking coefficient $S(G, v)$

$S(G, v)$ is the sticking probability of particles of given species and given velocity $v$. This quantity is equivalent to the coefficient usually called $S(E)$

(Buch & Zhang, 1991; Al-Halabi & van Dishoeck, 2007) which is the sticking probability for a given kinetic energy (see subsection 5.7.1). Two probabilities contribute to this sticking coefficient, the intrinsic probability and the probability due to the velocity. To simplify, we consider that these contributions are independent and we multiply them to obtain the final sticking probability $S(G, v)$:

- **The intrinsic probability** $S_0(G)$
  This is the probability for a given particle of zero kinetic energy ($v$=0) "put" on the surface to stick on it. $S_0(G)$ depends essentially on the mass of molecules and on the nature of the molecule-surface interaction. It corresponds to the state $S(G, v = 0)$.

- **The probability due to velocity**
  As mentioned above, each cell $C$ of the surface is characterised by a velocity $c(m, C)$ depending of the mass of impinging particles and on the cell itself. Thus, two possibilities are present:

  1. if $v > c(m, C)$, the molecule rebounds,
  2. if $v < c(m, C)$, the molecule sticks.

  Since the cells are different, we have a probability distribution $g_m(c)$ of values of $c(m, C)$. The sticking probability $P(v)$ is that for $v < c$:

$$P(v) = \int_v^\infty g_m(c)dc = \Phi(\frac{v}{c_0}), \tag{5.1}$$

  where $c_0$ is a constant parameter and $\Phi$ is a decreasing function that verifies $\Phi(0) = 1$ and $\Phi(\infty) = 0$.

Finally, the sticking probability $S(G, v)$ can be written as follows:

$$S(G, v) = S_0(G)\Phi(\frac{v}{c_0}). \tag{5.2}$$

### 5.6.3 The final sticking coefficient

In our experiments, the sticking coefficient $S(G, T_G)$ that we find is a function of both the type of molecules and their temperature. A thermal (or pseudo-thermal) distribution of the gas velocity seen by our surface $f(v, T_G)$ should then be added:

$$S(G, T_G) = \int_0^\infty S(G, v)f(v, T_G)dv \tag{5.3}$$

If the distribution is a pure thermal one, $f(v, T_G)$ should be the pure Boltzmann law

$$f(v, T_G) = Z^{-1} v^2 e^{-\frac{mv^2}{2k_B T_G}}, \tag{5.4}$$

where Z is a normalisation factor obtained by $\int_0^{+\infty} f(v, T_G) dv = 1$. The $v^2$ term results from the spherical element of volume.

But the irradiation angle should be taken into account. In fact our beam is irradiating the surface with a 62° angle with respect to the normal. This gives a privileged direction and therefore, a unidirectional velocity distribution $f_b$ seen by the surface. With this, two possibilities arise:

$$\begin{cases} \text{If } v_b < 0,\ f_b(v_b, T_G) = 0 \\ \text{If } v_b > 0,\ f_b(v_b, T_G) = Z^{-1} v_b e^{-\frac{mv_b^2}{2k_B T_G}} \end{cases} \tag{5.5}$$

where $v_b$ is the velocity component in the beam direction.

Since our sample selects in fact the particles that have this velocity direction, this distribution becomes the module distribution we are looking for:

$$f(v) = Z^{-1} v e^{-\frac{mv^2}{2k_B T_G}} \tag{5.6}$$

By combining Equations 5.2, 5.3 and 5.6, the final sticking coefficient is then given by:

$$S(G, T_G) = S_0(G) \int_0^{\infty} e^{-u} \Phi\left(\sqrt{\frac{2k_B T_G u}{mc_0^2}}\right) du \tag{5.7}$$

or

$$S(G, T_G) = S_0(G) \int_0^{\infty} e^{-u} \Phi\left(\sqrt{\frac{T_G u}{T_0(m)}}\right) du, \tag{5.8}$$

where $T_0(m)=\frac{mc_0^2}{2k_B}$ is the characteristic temperature depending on the mass of the molecule.

### 5.6.4 Mass dependence of the sticking coefficient

To simplify notations, we replace $T_G$ by $T$, $S(G, T_G)$ by $S_{H_2}(T)$ and $S_{D_2}(T)$, and $S_0(G)$ by $S_0(H_2)$ and $S_0(D_2)$ to represent the sticking coefficients of $H_2$ and $D_2$ respectively. We also introduce the two masses $m_{H_2}$ and $m_{D_2}=2m_{H_2}$ the masses of $H_2$ and $D_2$ respectively, we then have $T_0(H_2)$ and $T_0(D_2)=2T_0(H_2)$ due to proportionality to the mass. If we define the mathematical function $\hat{\Phi}$ by:

$$\hat{\Phi}(x) = \int_0^{\infty} e^{-u} \Phi(\sqrt{xu}) du \tag{5.9}$$

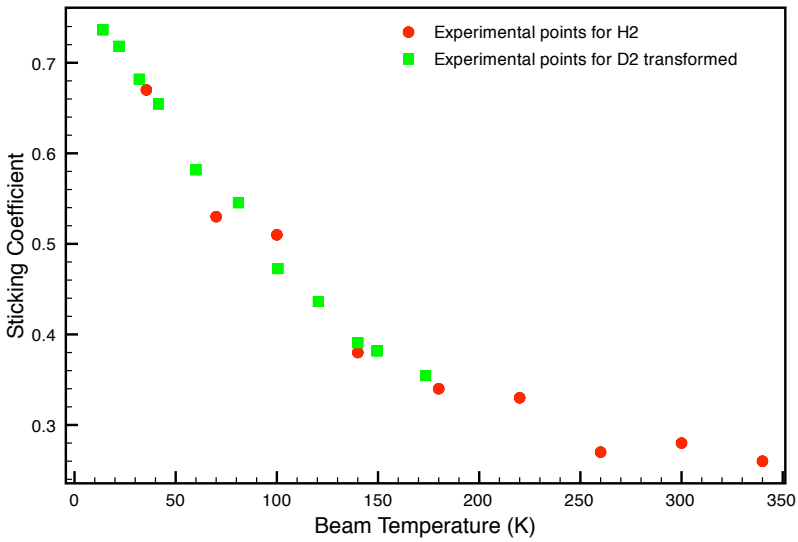


*Figure 5.6.1: In this figure we show a test of the model. Red circles represent the experimental sticking coefficient of $H_2$ and green squares represent the sticking coefficients of $D_2$ after the renormalisation-dilation transform of Eq. 5.11. These results are obtained for $S_0(D_2)/S_0(H_2) = 1.1$.*

we find,

$$\begin{cases} S_{H_2}(T) = S_0(H_2)\hat{\Phi}(\frac{T}{T_0(H_2)}) \\ S_{D_2}(T) = S_0(D_2)\hat{\Phi}(\frac{T}{2T_0(H_2)}) \end{cases} \tag{5.10}$$

from which we can deduce finally:

$$S_{H_2}(T/2) = \frac{S_0(H_2)}{S_0(D_2)} S_{D_2}(T). \tag{5.11}$$

This means that under our hypotheses, the experimental data of $S_{D_2}(T)$ should be equivalent to that of $S_{H_2}(\frac{T}{2})$ up to a renormalisation factor.

This result is very simple and very interesting because it is independent of the form of the function $\Phi$ that we use and then it constitutes a direct test of our theoretical hypotheses. Moreover it gives a method to obtain numerical sticking coefficients for $H_2$ at very low temperatures from the knowledge of sticking coefficient of $D_2$.

### 5.6.5 Comparison with experiment

We use Eq.5.11 to represent on the same graph experimental results of $H_2$ and $D_2$ with the ratio $\frac{S_0(D_2)}{S_0(H_2)} = 1.1$. The result is shown in figure 5.6.1. This figure clearly shows that our hypotheses are completely compatible with the experimental data of the sticking coefficients of $D_2$ and $H_2$ in figure 5.5.2.

## 5.7 Fitting the experimental data

Of course to go further, in particular to obtain a fit of these experimental results, we need to choose the unknown function $\Phi$. In the absence of complementary information, an infinite number of $\Phi$ functions can be chosen. Here we show the results corresponding to two functions: $\Phi(x) = e^{-x^2}$ and $\Phi(x) = \frac{1}{1+x^4}$. The reasons for this choice are explained below.

- **First fit**

$\Phi(x) = e^{-x^2}$ leads to the fitting function used by Buch & Zhang (1991) or by Al-Halabi & van Dishoeck (2007) for the sticking coefficient $S(E)$. The transformed function $\hat{\Phi}$ is $\hat{\Phi}(x) = 1/(1+x)$ and then

$$\begin{cases} S_{H_2}(T) = \frac{S_0(H_2)}{1+\frac{T}{T_0(H_2)}} \\ S_{D_2}(T) = \frac{S_0(D_2)}{1+\frac{T}{2T_0(H_2)}} \end{cases} \tag{5.12}$$

The results are shown on figure 5.7.1 and the values of coefficients are $S_0(H_2) = 0.835$, $S_0(D_2) = 0.918$ and $T_0(H_2) = 134.1$ K.

The fits are good for $T > 80\ K$, but the concavity (especially for $D_2$) in the domain $T < 80\ K$ does not seem to be the right one.

- **Second fit**

Since the fit of $D_2$ data in figure 5.7.1 seems to show that our fitting function has not the right concavity in the domain of low temperatures ($T < 80\ K$), we try to improve our choice with the new function $\Phi(x) = \frac{1}{1+x^4}$. Moreover we used a very different function from the first one to test the sensitivity of $S(T)$ to the $\Phi$ behaviour.

The very good agreement obtained with this new function proves the weak sensitivity of the thermal sticking coefficient to $\Phi$ (and then the difficulty of finding $\Phi$ from $S(T)$).

The function $\hat{\Phi}$ is not explicit in terms of usual functions, but a non-linear fit is always possible, giving the following values of the coefficients: $S_0(H_2)$=0.772, $S_0(D_2)$=0.847 and $T_0(H_2)$=100.0 K. The fit is shown in figure 5.7.2.

This second choice of $\Phi$ seems to reproduce better our experimental data of $D_2$ (concavity) at low temperatures, without any sensitive change in the quality of the fit of the experimental data of $H_2$. In fact, other $\Phi$ functions can give fits of the same quality (thermal velocity distribution makes $S(T)$ less sensitive to the type of $\Phi$).

As a first conclusion we find that this model is able to reproduce very well our experimental data. The mass dependence is well understood, but it is very difficult to rebuild the function $\Phi$ from only these data. So we try to use the sticking probabilities obtained by Buch & Zhang (1991) for H and D atoms to obtain this information.

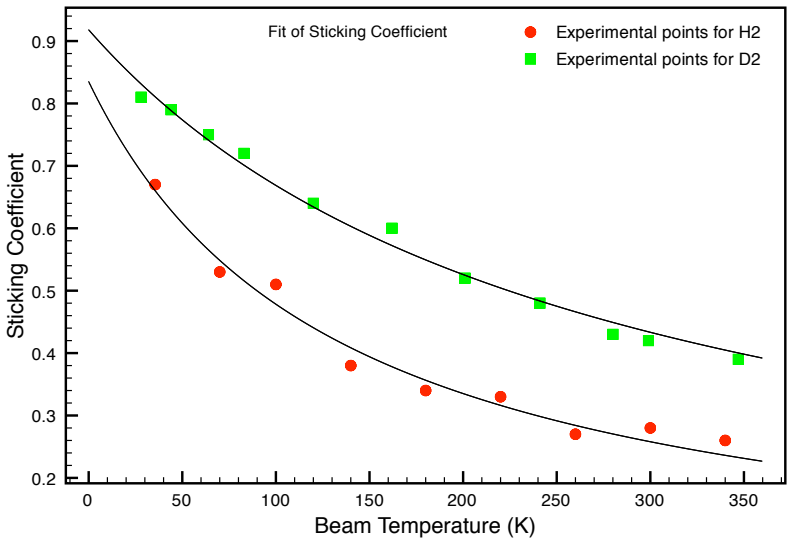


*Figure 5.7.1: Fit of experimental data obtained for* $\Phi(x) = e^{-x^2}$, $S_0(H_2) = 0.835$, $S_0(D_2) = 0.918$ *and* $T_0(H_2) = 134.1$ *K. Red circles and green squares represent* $H_2$ *and* $D_2$ *experimental data respectively.*

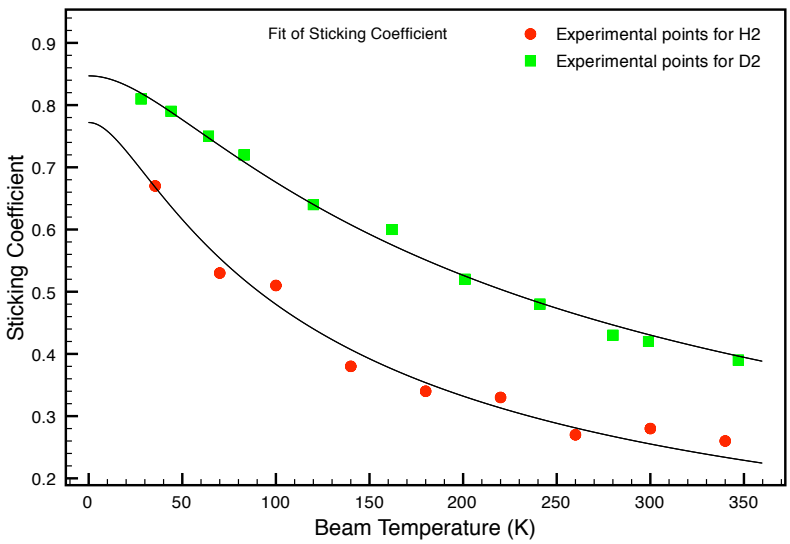


*Figure 5.7.2: Fit of experimental data obtained for* $\Phi(x) = 1/(1 + x^4)$, $S_0(H_2) = 0.772$, $S_0(D_2) = 0.847$ *and* $T_0(H_2) = 100$ *K. Red circles and green squares represent* $H_2$ *and* $D_2$ *experimental data respectively.*

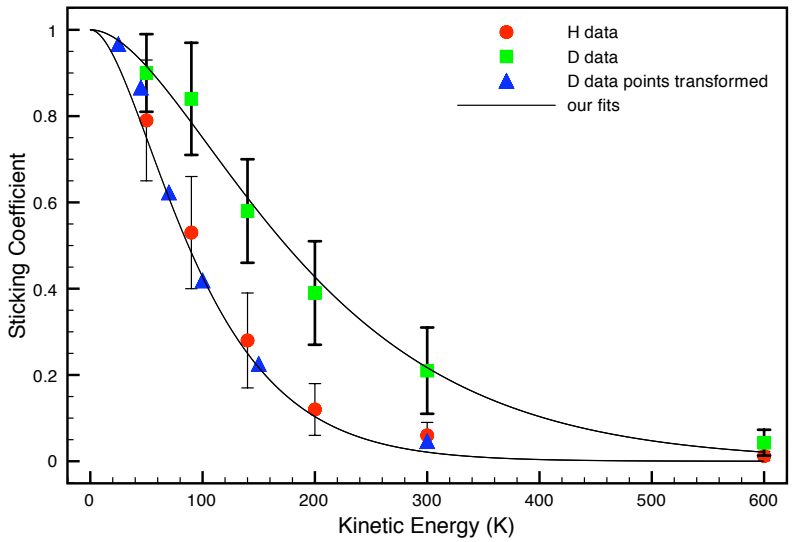


*Figure 5.7.3: Sticking coefficient for H and D atoms from Buch & Zhang (1991), plain circle for H, plain square for D. Plain triangle: renormalisation-dilation transform of D data points. Fit of H and D data points based on the function F.*

### 5.7.1 Testing the model on the sticking probabilities of H and D atoms from Buch & Zhang (1991)

In their article, Buch & Zhang (1991) give a set of values for the parameter $S_H(E)$ and $S_D(E)$ (table 2 and 3). These coefficients can be put in correspondence with our coefficient $S(G, v)$ through the relation $E = (1/2)mv^2$. Moreover the function $\Phi$ of our model only depends on water ice properties and then it must be roughly the same. These data allow us to get rid of the average effect due to the distribution velocity and to obtain the desired function $\Phi$.

Using the same hypotheses as previously exposed and using Equation 5.2, we obtain from our model:

$$S(E) = S_0 \Phi \left( \sqrt{\frac{2E}{mc_{0^2}}} \right) \tag{5.13}$$

Due to the mass ratio $m_D = 2m_H$, we get:

$$S_H(E/2) = \frac{S_0(H)}{S_0(D)} S_D(E). \tag{5.14}$$

In their exponential fitting $S(E) = e^{-E/E_0}$, Buch & Zhang (1991) found $E_0 = 200\ K$ for D and $E_0 = 102\ K$ for H. Then the relation $E_0(D) \simeq 2E_0(H)$ corresponding in fact to the mass term is recovered.

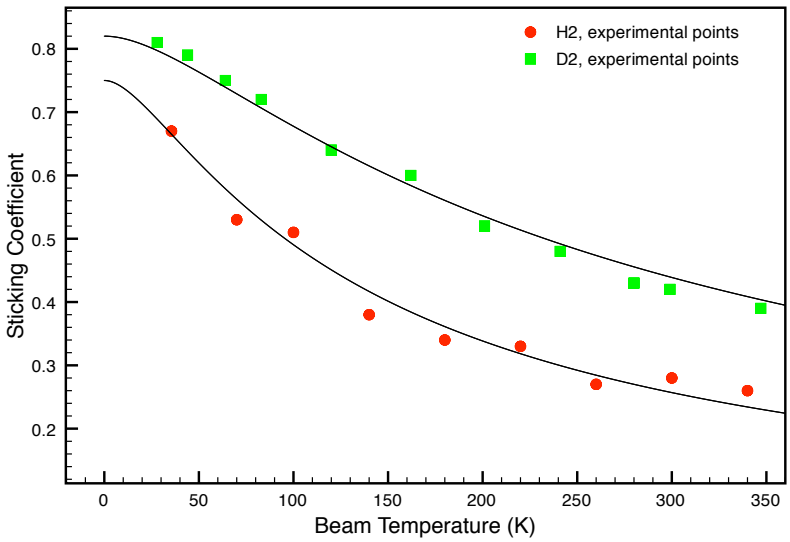


*Figure 5.7.4: Experimental results for $H_2$ and $D_2$ sticking probabilities and fits based on V. Buch data.*

The effect of Eq. 5.14 on their data can be tested as for $H_2$ and $D_2$ independently of any fit. This is shown in figure 5.7.3. The ratio $S_0(H)/S_0(D)$ has been fixed to $S_0(H)/S_0(D) = 0.95$. Due to the confidence intervals, it is reasonable to assume that in fact this ratio is equal to 1 and that $S_0(H) \simeq S_0(D) \simeq 1$.

Moreover we can improve the fitting function used by Buch & Zhang (1991) (corresponding to $\Phi(x) = e^{-x^2}$), using the modified function $\Phi(x) = (1+x^2)e^{-x^2}$. It leads to

$$\begin{cases} S_H(E) = S_0(H)F(\frac{E}{E_0}) \\ S_D(E) = S_0(D)F(\frac{E}{2E_0}) \end{cases} \tag{5.15}$$

where $F(x) = (1+x)e^{-x}$ and $E_0 = E_0(H) = (1/2)m_H c_0^2$.

The fits for atomic hydrogen and deuterium data are given in figure 5.7.3. with $S_0(H) = S_0(D) = 1$ and $E_0 = 52\ K$. The drastic modification of the parameter $E_0$ (from the pure exponential case where $E_0 \simeq 100\ K$) is not an error, it is a consequence of the change of function on the full range of temperatures.

The very good agreement of these curves with the data is a significant test, showing that we have obtained a good approximation of the $\Phi$ function.

### 5.7.2 Using Buch and Zhang data in our experimental results

In our model, the function $\Phi$ only depends on the surface properties (amorphous nature) and the velocity $c_0$ depends on the gas-surface interac-

tion. So we can roughly consider that the function $\Phi(x) = (1+x^2)e^{-x^2}$ used for fitting Buch's results is valid in our experiment.

At the opposite, the velocity parameter $c_0$ must be different for atom-surface interaction and for molecule-surface interaction.

We are able to calculate the function $\hat{\Phi}$ of Eq. 5.9:

$$\hat{\Phi}(x) = \frac{1+2x}{(1+x)^2} \tag{5.16}$$

and then

$$\begin{cases} S_{H_2}(T) = S_0(H_2)\hat{\Phi}(\frac{T}{T_0(H_2)}) \\ S_{D_2}(T) = S_0(D_2)\hat{\Phi}(\frac{T}{2T_0(H_2)}) \end{cases} \tag{5.17}$$

where $T_0(H_2) = m_{H_2}c_0^2(H_2)/(2k_B)$.

Figure 5.7.4 shows the fits of our data obtained with this new function: they are in very good agreement.
The values of the parameters are $S_0(H_2) = 0.75$, $S_0(D_2) = 0.82$ and $T_0(H_2) = 70\ K$.

### 5.7.3 Final remark

Choosing the dependence of sticking in velocity rather than in kinetic energy can be explained. On one hand the gas-surface interaction is based on short-ranged potentials that imply a finite distance $L$ of interaction, and on the other hand, sticking implies an energy transfer to the surface that needs a minimal time $\tau_0$ of interaction. If the impinging particle has a velocity $v$, it interacts with the surface during a time $\tau$ estimated to $\tau \simeq 2L/v$. Then the particle sticks to the surface if $\tau > \tau_0$ that is $v < c = 2L/\tau_0$, where $c = 2L/\tau_0$ is the characteristic velocity relative to sticking.

Now, we can compare the velocities $c_0(H)$ and $c_0(H_2)$ from the values $m_H c_0^2(H) = 2E_0 = 104\ K$ and $m_H c_0^2(H_2) = T_0(H_2) = 70\ K$. This leads to

$$\frac{c_0(H_2)}{c_0(H)} = \sqrt{\frac{70}{104}} \simeq 0.83. \tag{5.18}$$

As expected $c_0(H_2) \neq c_0(H)$, but the values are close.

If we return to our estimate $c_0$=2 L/$\tau_0$ where $L$ is a maximal distance of interaction and $\tau_0$ a minimal time of interaction, and if we assume roughly that $\tau_0(H_2) \simeq \tau_0(H)$ (we have not reached a regime of limited energy transfer), we find

$$\frac{L(H_2)}{L(H)} \simeq 0.83. \tag{5.19}$$

This result is compatible with the intuitive idea that the range of $H_2$-surface interaction is shorter than that of the H-surface interaction.

In fact, it is more difficult to trap $H_2$ than to trap H in a potential well on the surface, since $H_2$ has internal movements with possible energy transfers

between the different degrees of freedom of the molecule (rotation-translation of the two atoms). Thus if the two atoms of the molecule approach the critical interaction distance L(H) where only one H atom is trapped, this does not guarantee that the molecule will be trapped in the potential well and might be kicked out from the surface. Where such energy transfers do not take place in the case of only one H atom impinging on the surface.

## 5.8 Conclusions

In this chapter I have described in details a set of experiments that we have conducted in our laboratory in Cergy to measure the sticking coefficients of molecular hydrogen and deuterium on *np*-ASW ice surfaces held at 10 K using the King & Wells method. A study of the variation of the sticking coefficients with the molecular beam temperature was also presented. To my knowledge, this is the first experimental work that measures the sticking coefficient of hydrogen and deuterium molecules as a function of the beam temperature.

A collaboration with H. Bergeron (LCAM, Orsay), provided us with a model, written for this purpose, to fit the obtained experimental data. We found a high mass dependence between the sticking coefficients of $H_2$ and $D_2$. Using the same mass dependence, and improving the fitting function used in the model of Buch & Zhang (1991), we were able to fit their data and to transform the sticking coefficient of D atoms to that of H atoms. We were also able to fit our experimental data.

We are perfectly aware that the detailed interaction (and behaviour) of atoms and molecules with the ASW ice surface are not similar. Moreover in each situation (atomic or molecular), we omit a lot of parameters such as the surface temperature. But one of the main interests of this kind of statistical models is precisely to erase the details and to keep the main features. This is why we can use this model on Buch & Zhang (1991)'s data and extract some useful information for our fitting of molecular experimental points.

Moreover, the "bell-like" shape of the fitting function $F\left(\frac{T}{T_0}\right) = (1 + \frac{T}{T_0})exp\left(-\frac{T}{T_0}\right)$ for low beam temperatures ($\leq$10 K) is similar to the behaviour of the sticking of $H_2$ and $D_2$ observed by Schutte et al. (1976) and Govers et al. (1980). These authors found that, when going from 3.5 K to 10 K, the sticking coefficient of $H_2$ ($D_2$) (on $H_2$- ($D_2$)-free surface) decreases very slightly and stays almost constant.

The astrophysical interest of this chapter is that we can now extract some useful values of the sticking coefficients of $H_2$ and $D_2$ relevant to the dark clouds of the interstellar medium. For grains covered with amorphous ice mantles, where the temperature of the grain is equal to the temperature of the beam and is equal to 10 K, we found a sticking probability $S_{D_2}$=0.82 for $D_2$ and $S_{H_2}$=0.75 for $H_2$. And from the improved fitting function from Buch

| Species | H | $H_2$ | D | $D_2$ |
|---|---|---|---|---|
| From Buch & Zhang (1991) | $S_0$=0.97 $T_0$=52 K | – | $S_0$=0.99 $T_0$=104 K | – |
| Our data | = | $S_0$=0.75 $T_0$=70 K | = | $S_0$=0.82 $T_0$=140 K |

*Table 5.8.1: Comparison between our sticking values for H, $H_2$, D and $D_2$ obtained with the formula $S(T) = S_0(1 + \frac{T}{T_0})exp\left(-\frac{T}{T_0}\right)$ and those of Buch & Zhang (1991) obtained with $S(T) = S_0 exp\left(-\frac{T}{T_0}\right)$ for a beam temperature $T = 10\ K$.*

& Zhang (1991) we found that the sticking coefficient of D atoms $S_D$=0.99 and that of H atoms is equal to $S_H$=0.97 (table 5.8.1).

## 5.9 Perspectives

I am aware that the extrapolation of experimental data obtained for the molecular species is not enough to really deduce the sticking coefficients of H and D atoms. But the measurement of the sticking coefficients of hydrogen and deuterium atoms, even if feasible, remains indirect and difficult.

In the present section I will describe an experiment that can be done in order to measure the sticking coefficients of hydrogen and deuterium atoms on p-ASW ice surfaces.

### 5.9.1 Sticking coefficients of $D_2$ and $H_2$ on *p*-ASW films

This experiment consists on irradiating a *np*-ASW and a *p*-ASW ice surfaces with the same amounts of $D_2$ and then heat the surface in order to do the TPD after each irradiation. After that we compare the amounts of desorbing $D_2$ obtained on both surfaces for the same irradiation time (fig. 5.9.1).

If $N_{D_2}$ is the amount of $D_2$ molecules sent to the surface ($N_{D_2}$ is the same on both types of ice), the amount of $D_2$ that desorb after each TPD is given by

$$F_{D_2} = S_{D_2} \times N_{D_2}, \tag{5.20}$$

where $S_{D_2}$ is the sticking coefficient of $D_2$ molecules. I will call $S^p_{D_2}$ and $S^{np}_{D_2}$ the sticking coefficients of $D_2$ molecules on *p*- and *np*-ASW ice films respectively. And then we will have

$$F^p_{D_2} = S^p_{D_2} \times N_{D_2} \tag{5.21}$$

and

$$F^{np}_{D_2} = S^{np}_{D_2} \times N_{D_2}, \tag{5.22}$$

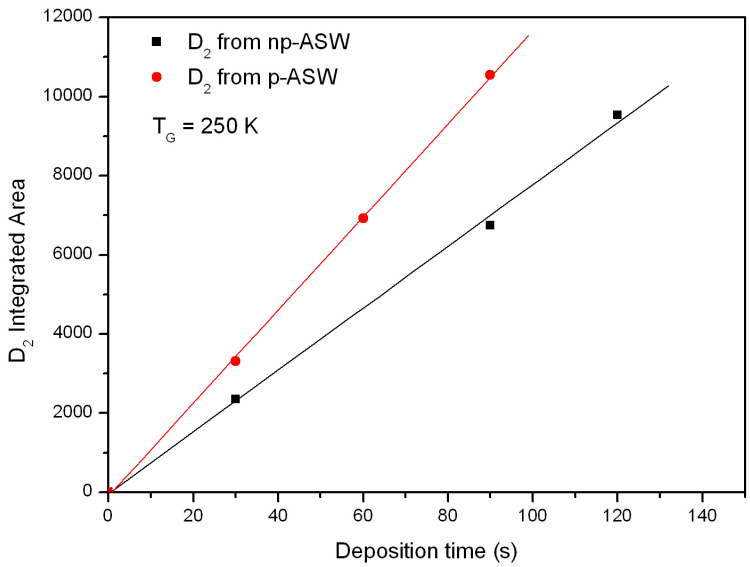


*Figure 5.9.1: Integrated area of $D_2$ TPD profiles obtained after irradiating p- and np-ASW with different amounts of $D_2$. Surface temperature is 10 K and beam temperature is 250 K.*

for the amounts of $D_2$ molecules detected during the TPD from *p*- and *np*-ASW films respectively.

Combining Eq. 5.21 and Eq. 5.22 leads to

$$S^p_{D_2} = \frac{F^p_{D_2}}{F^{np}_{D_2}} \times S^{np}_{D_2} \tag{5.23}$$

Knowing already the sticking coefficients of $D_2$ for a beam temperature ranging between 0 K and 350 K, and measuring the amounts of $D_2$ that desorb from each ASW ice film, we can calculate the sticking coefficient of molecular deuterium on *p*-ASW ice for a given beam temperature.

Figure 5.9.1 shows preliminary experimental results of this method for one temperature only. Using these values, we obtain a sticking coefficient of $D_2$ on *p*-ASW ice $S^p_{D_2}$=0.55 (i.e. the sticking coefficient is enhanced by 10% ($S^{np}_{D_2}$=0.5, see fig. 5.5.2).

The same experiment is then repeated for several beam temperatures and then the variation of the sticking coefficient of $D_2$ is obtained. With the model and the mass-temperature dependence between $S_{D_2}$ and $S_{H_2}$, the variation of the sticking coefficient of $H_2$ on *p*-ASW is then obtained.

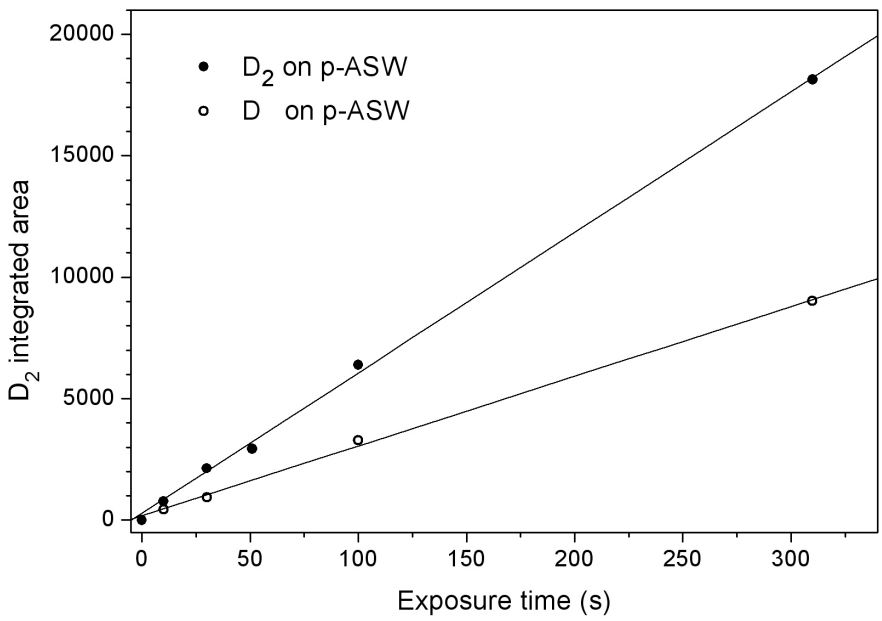


*Figure 5.9.2: Integrated area of $D_2$ TPD profiles obtained after irradiating a p-ASW ice film with different amounts of $D_2$ and D. Surface temperature is 10 K and beam temperature is 300 K.*

### 5.9.2 Sticking coefficients of D and H atoms on *p*-ASW films

To measure the sticking coefficients of hydrogen and deuterium atoms on *p*-ASW ice films we have proceeded as follows:

- We irradiate a *p*-ASW film with different exposure times of $D_2$ and then do the TPD after each exposure. A straight line is obtained (within the error bars) as shown in figure 5.9.2 (plain circles).
- We irradiate the same ice with the same exposure times but with D+D (discharge on) and we do the TPD after each exposure and measure the integrated area under each TPD profile (empty circles in figure 5.9.2).

If $N_{D_2}$ is the total amount of $D_2$ molecules sent to the surface, the total amount that desorbs during the TPD is given by

$$F_{D_2}^{off} = S_{D_2}^{p} \times N_{D_2}. \tag{5.24}$$

When the discharge is on, the amount of $D_2$ that desorbs is given by

$$F_{D_2}^{on} = N_{D_2}^{on} + N_{D_2 form}^{on}, \tag{5.25}$$

where $N_{D_2}^{on}$ is the amount of $D_2$ coming from the non-dissociated part of the beam

$$N_{D_2}^{on} = (1-\tau) S_{D_2} N_{D_2}, \tag{5.26}$$

where $\tau$ is the dissociation rate.

$N^{on}_{D_2 form}$ is the amount of $D_2$ that is formed on the surface of the $p$-ASW ice film. It is given by

$$N^{on}_{D_2 form} = 2\tau S_D \mu\eta N_{D_2}, \tag{5.27}$$

where $\mu$ is the fraction of $D_2$ that is trapped in the pores after formation and $\eta$ is the probability that has an adsorbed D atom to recombine with another adsorbed atom on the surface.

This leads to

$$F^{on}_{D_2} = \left[(1-\tau)S_{D_2} + 2\tau S_D \mu\eta\right] N_{D_2} \tag{5.28}$$

and finally we obtain

$$S_D = \left[\frac{F^{on}_{D_2}}{F^{off}_{D_2}} - (1-\tau)\right] \times \frac{S_{D_2}}{2\tau\mu\eta} \tag{5.29}$$

On $p$-ASW ice surfaces, the product $\mu\eta$ is usually estimated to be equal to unity (Hornekær et al., 2003). In my point of view this value is very optimistic, so let us consider it equal to $\mu\eta$=0.9. The measured dissociation rate $\tau$ is equal to 70% and $S_{D_2}$=0.55 (see subsection 5.9.1). By using the obtained $F^{on}_{D_2}$ and $F^{off}_{D_2}$ from figure 5.9.2, we obtain a sticking coefficient of D atoms $S_D \approx 0.2$ on $p$-ASW ice for a beam temperature of 300 K.

We then would have to repeat the same procedure for other beam temperatures to obtain the variation of $S_D$ as a function of $T_G$. After fitting the results with the model, the sticking coefficient of hydrogen atoms on $p$-ASW ice can then be obtained.

### 5.9.3 Precision and uncertainty of the measurements

Precision and uncertainty of the measurements depend on the stability of the beam flux and the detection efficiency of the QMS. They have to be as stable as possible during the time length of the experiments. This is especially when each experiment might take up to 30 minutes.

The flux changes with the temperature of the beam. The lower the temperature, the more diffusive becomes the beam and the less molecules enter the main chamber. This variation of the flux as a function of the beam temperature was one of the important points to study and to understand in order to finalise this chapter. But unfortunately, due to several problems in the experimental set-up, followed by some repairs, modifications and add-ons during the last year, this work could not be done before the end of this thesis, but will be included in the article that is currently in its final stage of preparation.

Instability in the QMS detection occurred when I was conducting experiments to study the variation of the flux as a function of the beam temperature last June. This problem is now solved but, due to the lack of time, these experiments were stopped.

# Chapter 6

# Mobility of cold hydrogen atoms on icy dust grains

## 6.1 Introduction

### 6.1.1 The context

As mentioned in chapter 2, the diffusion of an adsorbed hydrogen atom on the surface of icy interstellar dust grains is of paramount importance for the formation of molecular hydrogen, the hydrogenation and/or deuteration of other species. In fact, as we know by now, under the conditions ruling the dense clouds of the ISM, molecular hydrogen formation via the prompt Eley-Rideal mechanism is highly improbable since the H coverage of the grain surface stays very low. This means that the only efficient mechanism leading to $H_2$ formation is the Langmuir-Hinshelwood one where at least one of the two hydrogen atoms should diffuse on the surface of the grain in order to interact with the second atom and to form a molecule. The "hot atom" (Harris-Kasemo) mechanism is also improbable in these same conditions, since the kinetic temperature of the gas ($\sim$10 K) is not sufficiently high to allow the atom to diffuse on the surface with superthermal energy until it thermalises to the temperature of the grain. Thus, the only plausible mechanisms ruling the diffusion of hydrogen atoms on the icy mantles of the dust grains in dark clouds are tunnelling effect (quantum diffusion) and thermal hopping (See Chap. 2 Sect. 2.4 for details on these processes).

### 6.1.2 Previous works

The mobility of atomic hydrogen on astrophysically relevant ice surfaces have been studied theoretically and experimentally over the years. Tielens & Hagen (1982) were the first theoreticians to use chemical models hypothesizing the mobility of hydrogen atoms on dust grains; followed by several teams such as Buch & Zhang (1991), Masuda et al. (1998), Takahashi et al. (1999b), Cuppen & Herbst (2007) and Al-Halabi & van Dishoeck (2007).

For example, classical molecular dynamics (CMD) calculations by Masuda et al. (1998) were used to investigate the sticking and the difusion processes of atomic hydrogen on the surface of a"rigid" amorphous water ice at 10 K. These authors divided the mobility process into two steps: (1) diffusion of a hydrogen atom after it sticks on the ice slab and until it gets trapped in a potential well (called migration); and (2) rediffusion of the same atom after being trapped. They found that a hydrogen atom at 10 K migrates via thermal hopping on the ice slab before being trapped and that it has a migration length $l$=60.4 Å during a migration time of 1.7 ps at the surface of an amorphous ice at 10 K. However, these authors found that none of the hydrogen atoms rediffuse from one site to another after being trapped and found a diffusion barrier $E_{diff}$=108 meV and then a diffusion time $\tau_{diff}=10^{34}$ years[1] for a hydrogen atom to diffuse from one site to another.

Takahashi et al. (1999b) continued the works of Masuda et al. (1998) and completed them by doing simulations on both a "rigid" and a "soft" amorphous ice slabs plus calculation on the partitioning of the $H_2$ formation energy Takahashi et al. (1999a). In the same conditions ($T_{surface}=T_{gas}$=10 K) they found a diffusion time, after trapping, $\tau_{diff}$=10 s for a diffusion barrier $E_{diff}$=27 meV for a hydrogen atom to move from one site to another via thermal hopping.

Al-Halabi & van Dishoeck (2007), while studying the sticking probability of hydrogen atoms on amorphous water ice, found that a hydrogen atom arriving onto a surface of ice at 10 K with an incident energy $E_i$=300 K diffuses for $l\leq$60 Å due to the hot atom mechanism, in good agreement with the results of Masuda et al. (1998), and that if $E_i$=200 K, the diffusion distance is about 18 Å before it is thermalised, in good agreement with the results of Buch & Zhang (1991) who found $l$=20 Å. They also calculated the diffusion time and the surface explored by a hydrogen atom and found them to be $\tau_{diff}$=1 ms for $A$=1.26 $10^{-8}$ cm$^2$. This means that the mobility due to the Langmuir-Hinshelwood is also high, which ensures that $H_2$ is formed almost instantaneously on a porous amorphous substrate at 10 K (in agreement with Hornekær et al. (2003)).

But one cannot neglect the fact that other calculations and experiments rule out the mobility of hydrogen atoms on such surfaces. This is the case of Smoluchowski (1981) who found that a hydrogen atom makes much less than one jump at a surface temperature of 10 K. These authors found that two adsorbed hydrogen atoms react and form an $H_2$ molecule only if the distance between them is $\leq$10 Å, and that thermal hopping becomes possible only if the temperature of the amorphous ice is higher than 30–50 K, although it becomes limited by the short residence time of the atoms.

According to their experimental results, G. Vidali and co-workers (Katz et al., 1999; Manicò et al., 2001; Perets et al., 2005) conclude that the dif-

[1]The diffusion time is given by $\tau=Ae^{-E_{diff}/k_BT}$.

fusion of hydrogen atoms on the surface of an amorphous ice substrate is thermally activated when the temperature of the surface is increased during TPD experiments. In fact, Perets et al. (2005) found that the mobility of hydrogen atoms on a highly amorphous water ice surfaces at low temperatures is very low and that the diffusion barrier $E_{diff}$=55 meV is two times higher than that found by Takahashi et al. (1999b). Their assumptions are in contradiction with those of Hornekær et al. (2003) who found that the Langmuir-Hinshelwood mechanism is high even at a temperature as low as 8 K.

A recent experimental work by Mennella (2008a) on nano-sized carbon particles covered by a porous amorphous water substrate at 12 K and irradiated by hydrogen atoms at 80 K, demonstrates the hydrogenation of the carbon layer by forming C-H bonds in tertiary $sp^3$ carbon sites. The activation of the 3.47 $\mu$m band[2] means that impinging hydrogen atoms interact with the water substrate and reach the carbon grains. These results were also confirmed by density functional theory (DFT) calculations done by Bauschlicher et al. (2007).

Since more than thirty years (Hollenbach & Salpeter, 1971), the mobility of hydrogen atoms on icy dust grains is a matter of debate and controversy still exists. This chapter presents a simple set of experiments that proves the mobility of hydrogen atoms at 50 K on porous ASW ice surfaces at 10 K.

## 6.2 Experiments

The idea of the experiments is to prove the mobility of cold hydrogen atoms by using $O_2$ molecules as a probe. In fact hydrogen atoms are reacting with $O_2$. If the surface is held at 10 K more and more reactions may occur with the deposition time if H atoms are mobile and then less $O_2$ molecules detected in a subsequent TPD. For this purpose we conduct the same experiment twice. The first time on a 20 ML of *p*-ASW ice substrate and the second on a thicker substrate (250 ML) of the same ice structure.

### 6.2.1 Procedures

We start by growing the *p*-ASW ice substrate on 50 ML of *np*-ASW sub-layer. This sub-layer is grown by direct deposition with the capillary vaporiser at a surface temperature of 120 K as indicated in chap. 4 sect. 4.2.6. The purpose of the *np*-ASW ice sub-layer is to isolate the upper porous amorphous layer from the copper sample holder (Engquist et al., 1995). The 20 ML of *p*-ASW ice are grown following the background deposition method at a surface temperature of 10 K. Since ASW films deposited by background take a long time to form (∼100 minutes to grow 20 ML of *p*-ASW) and

[2]Absorption band due to the C-H stretching vibration of tertiary $sp^3$ carbon atoms.

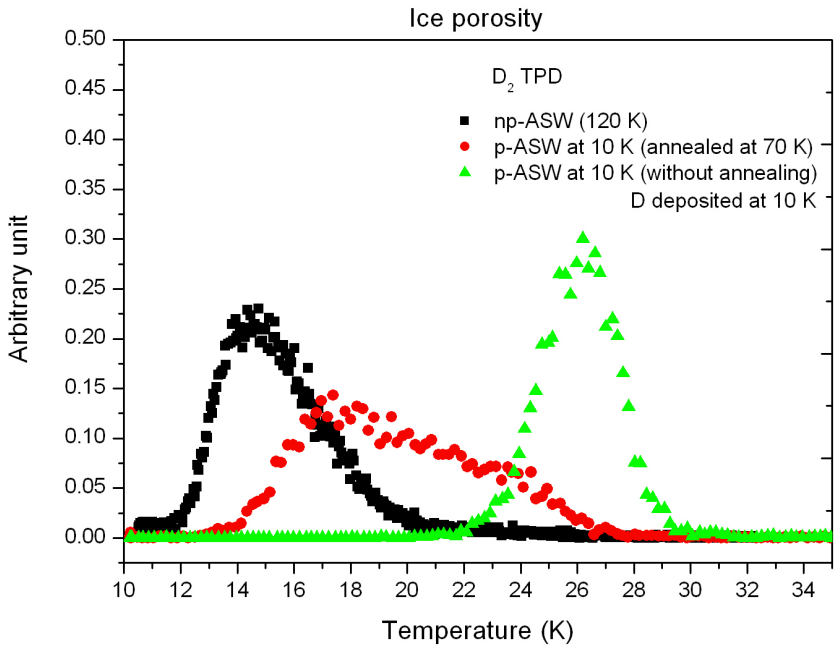


*Figure 6.2.1: The same amount of $D_2$ deposited on three different types of amorphous ice: np-ASW in black, p-ASW annealed to 70 K in red and p-ASW without annealing in green. We see that even if the ice was grown highly porous (at 10 K), its porosity is reduced considerably depending on the annealing temperature, in this case 70 K. The heating ramp is set to 10 K/min).*

since a long time (∼60 min) is needed to reach the base pressure again (from 2 $10^{-8}$ to 2 $10^{-10}$ mbar), the 250 ML of *p*-ASW film is deposited following the direct deposition method with the capillary vaporiser at 20 mm in front of the sample holder at 10 K (See chap. 4 sect. 4.2.6). Then the porosity of the 250 ML substrate is lower than that of the 20 ML *p*-ASW ice but its thickness ensures a more complex pore structure.

The desorption temperature of $O_2$ molecules, from a *p*-ASW ice surfaces, ranges from ∼30 K to ∼60 K. After the growth of the *p*-ASW substrates, they are annealed to 70 K to avoid any subsequent morphological changes due to the adsorption and desorption of $D_2$ and $O_2$ molecules (TPD up to 65 K). It has been previously shown (Chap. 4 Sect. 4.2.7) that the porous structure is reduced but stabilised by the annealing process. This is verified by looking at the shift of the $D_2$ desorption peak in figure 6.2.1.

When the base pressure in the UHV chamber is back to ∼1 $10^{-10}$ mbar, and the ice is annealed to 70 K and cooled back down to 10 K, we expose it

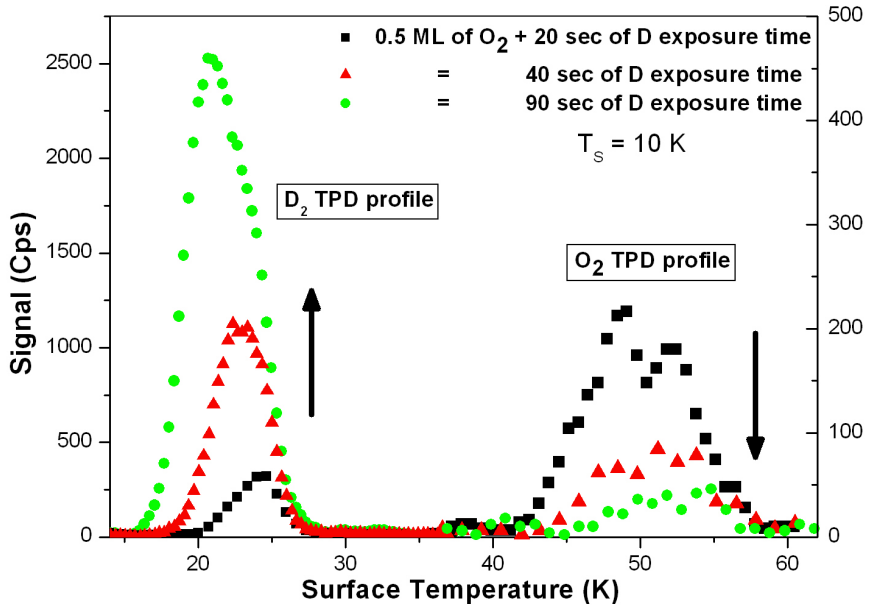


*Figure 6.2.2: TPD profiles of $D_2$ and $O_2$ after deposition of 0.5 ML of $O_2$ and followed by different deposition times of D (20 s: black squares, 40 s: red triangles and 90 s: green circles). The arrows emphasise that the quantity of desorbed $O_2$ decreases as the amount of exposed D grows. The heating ramp is set to 10 K/min).*

to 0.5 ML of $O_2$ molecules. During the beam deposition, the $O_2$ pressure in the first stage of the second beam line was stable at $\sim$5 $10^{-5}$ mbar. With this stable pressure we obtain, in the main chamber, a flux of $\sim$0.003 ML/s (1 ML every 6 minutes of $O_2$ exposure time). The calibration of the beam was done as explained in Chapter 3, section 3.5.3 by determining the $O_2$ exposure time required to saturate the first $O_2$ monolayer on *np*-ASW ice (Kimmel et al., 2001).

The whole ($O_2$ and *p*-ASW ice substrate) is then irradiated by a certain amount of cold D atoms ranging from 0 to 2 EML (exposed ML). This unit is used instead of ML because in the case of deuterium and hydrogen the sticking coefficient is not necessarily unity, so that not all the atoms or molecules that reach the surface of the ice stick on it. The $D_2$ beam is dissociated in the microwave discharge with a dissociation rate of 50% during this set of experiments. Several checks are done between measurements to ensure that this dissociation rate is stable during the experiments. Before leaving the first stage, the beam is cooled to 50 K by passing through the aluminium nozzle screwed to the He closed-cycle cryostat of the first beam line.

After each D+$D_2$ irradiation, the surface is heated with a linear ramp

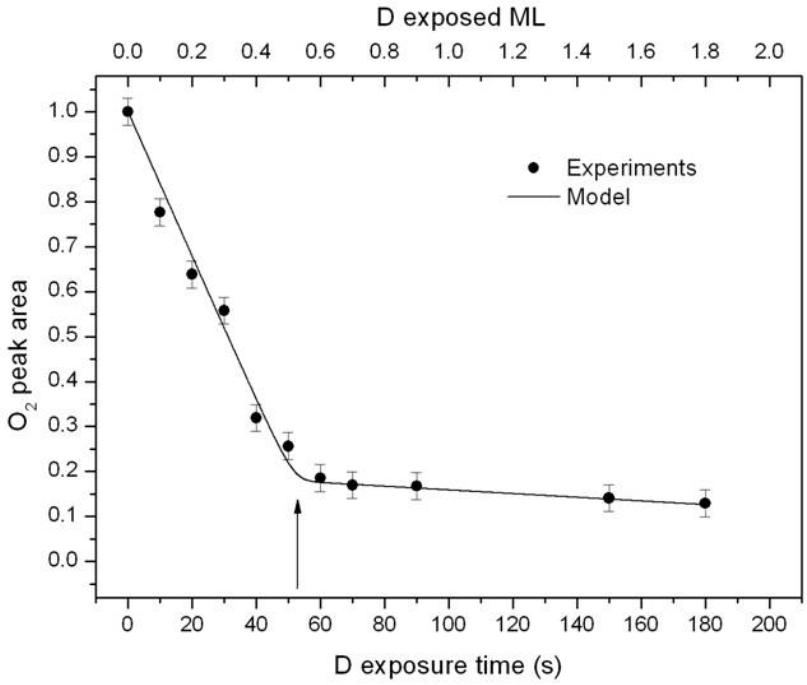


*Figure 6.2.3: Normalised $O_2$ TPD integrated areas following different D exposures. The $O_2$ normalisation is made with respect to the TPD integrated area corresponding to 0.5 ML of $O_2$ alone. $O_2$ and D both deposited at a surface temperature of 10 K. The solid line represents the model results (see text).*

of 10 K/min to 65 K and TPD profiles of $D_2$ and $O_2$ are simultaneously monitored with the QMS in front of the surface. The time needed to close the valve of D+$D_2$ and place the QMS in front of the surface is ∼1 minute. An example of $D_2$ and $O_2$ TPD profiles are shown in figure 6.2.2 for three different D irradiation times (20 s, 40 s and 90 s). We can see that the integrated area under the $O_2$ TPD profiles decreases and that the integrated area under the $D_2$ TPD profiles increases with the increasing deposition time of cold D atoms. This figure proves that the oxygen molecules adsorbed on the surface of the ice substrate are being consumed by the deuterium atoms. Here, two processes are at play: (1) the formation of $D_2$ and (2) the destruction or consumption of $O_2$ by D atoms.

### 20 ML of *p*-ASW

This experiment is repeated for several D exposure times, ranging from 0 EML to 1.8 EML, on the same 20 ML *p*-ASW ice substrate. The integrated area under each TPD profile of $O_2$ and $D_2$ are shown in figures 6.2.3 and 6.2.4 respectively, as a function of D exposure time (lower axis) and D EML (upper axis).

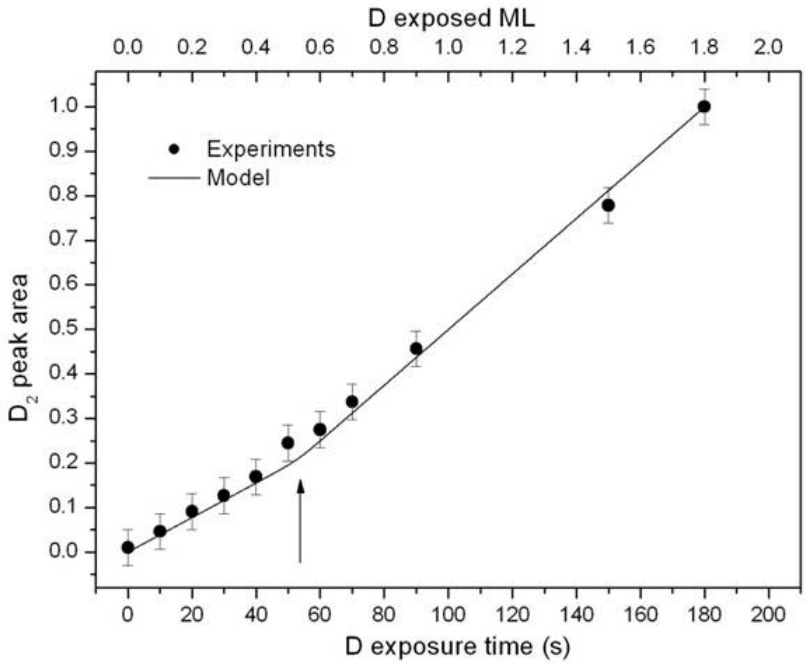


*Figure 6.2.4: Normalised $D_2$ TPD integrated areas following different D exposures. The $D_2$ normalisation is made with respect to the TPD integrated area corresponding to 1.8 ML of D. $O_2$ and D both deposited at a surface temperature of 10 K. The solid line represents the model results (see text).*

Like figure 6.2.2, figure 6.2.3 clearly shows that the quantity of desorbing $O_2$ decreases with the increase of the exposed dose of D atoms. A sudden change in the slope of the linear decrease occurs after ∼0.5 EML of D exposure which is equivalent to 50 s of D exposure time. This means that we have two regimes: (1) a fast destruction regime between 0 s and 50 s of D exposure and (2) a slow destruction regime after 50 s of D exposure. A similar change appears in the slope of figure 6.2.4 in the case of $D_2$ formation. This change, although less marked, occurs at almost the same time than that in figure 6.2.3 in the case of $O_2$. This means that the formation of molecular deuterium also presents two regimes: (1) a slow formation regime between 0 s and 50 s of D exposure and (2) a fast formation regime after 50 s of D exposure.

These experiments can be explained as follows: as D atoms are deposited onto the *p*-ASW ice substrate, two competing mechanisms are occurring, namely $O_2$ destruction and $D_2$ formation. Assuming that D atoms are mobile on porous ice at 10 K, a deuterium atom has two possibilities, either encounter another D atom and react with it to form a $D_2$ molecule (D+D formation) or an $O_2$ molecule and react with it to form $O_2D$ ($O_2$ destruction) (Miyauchi et al., 2008; Ioppolo et al., 2008). It is significant that in both cases of $O_2$ and $D_2$ desorptions, the change in the slopes occurs after the same time of D exposure (marked by arrows in figures 6.2.3 and 6.2.4). The change in the slopes in both pictures suggests that after ∼50 s (0.5 EML) of D irradiation, when most of $O_2$ molecules has been destroyed, a greater number of D atoms are available on the surface of the ice substrate to form $D_2$. The presence of a rapid regime of $O_2$ destruction (80% of the initial dose destroyed by 0.5 EML of D) and of a slow regime (for the remaining 20% of the initial dose of adsorbed $O_2$) can be ascribed to the non-perfect overlap of the two beams on the surface of the sample holder.

As schematised in figure 6.2.5, the molecular $O_2$ and atomic D beams actually have an 80% of full overlap on the surface, thus 20% of the deposited $O_2$ dose is only exposed to a background flux of D atoms ∼10 times lower than the direct flux. This has been verified using the flag valve that intercepts the direct D beam when it enters in the main chamber. Without a direct D beam, a small indirect exposure of D atoms still remains in the chamber and the $O_2$ destruction rate becomes ∼10 times lower, as occurs after ∼50 s of D atom irradiation time.

If the two beams were overlapping perfectly on the surface, the destruction of $O_2$ in the fast regime would have been 100% instead of 80% during the first 50 s of D exposure. One should note that the change of the slope in the case of $D_2$ is not rough as in the case of $O_2$ and that it increases rapidly during the first 50 s of D exposure time. This is due to the fact that we monitored the desorptions of $D_2$ coming from both D+D and the non-dissociated $D_2$. So the signal was not corrected by substracting the desorption of the non-dissociated part of the $D_2$ beam.

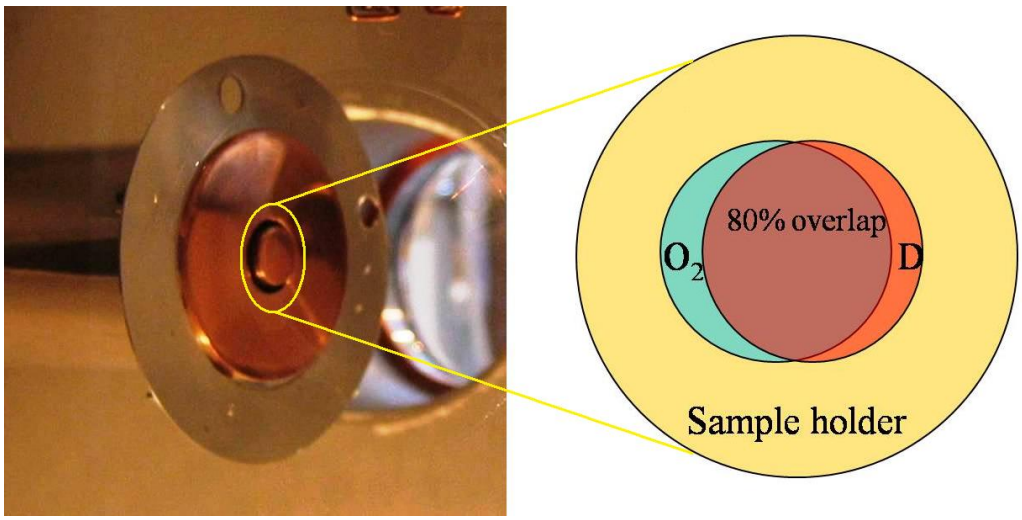


*Figure 6.2.5: Overlap of the $O_2$ and D beams on the surface of the sample holder.*

### 250 ML of *p*-ASW

In order to verify that the destruction of $O_2$ molecules on a 20 ML *p*-ASW ice substrate was actually due to the fact that mobile D atoms were able to scan the porous surface, we did the same experiment using a thicker *p*-ASW ice substrate. This time, on 250 ML p-ASW films, we also deposited the $O_2$ molecules at a higher temperature, namely 25 K, to favour $O_2$ mobility and to have $O_2$ molecules not only adsorbed on the surface of the ASW but also deeper into the porous structure. The results obtained are shown in figure 6.2.6. The plain circles represent the normalised integrated areas of desorbed $O_2$ of the molecular beam originally deposited at a surface temperature of 25 K and then exposed to different times of D atoms at 10 K. The empty circles represent the normalised integrated areas under the TPD profiles of $O_2$ molecules previously deposited at 10 K and then exposed to the same D atom exposures.

First, we notice that in this experiment the $O_2$ destruction rate is much slower than in the case of the 20 ML *p*-ASW substrate. This is due to the fact that the porosity is greater in the case of the 250 ML. The structures (holes, pores, piles...) are more pronounced. The total accessible surface becomes higher and subsequently the average surface density of $O_2$ molecules is reduced. In this case, the $D_2$ formation is favoured. Secondly, we find that if $O_2$ is deposited at 25 K, the destruction rate is even lower. This is due to the fact that, at 25 K, $O_2$ molecules are mobile on the inner and outer surface of the ASW ice. Therefore $O_2$ molecules are spread over all the accessible porous surface. The $O_2$ surface density is again lower and $D_2$ formation is favoured. We also notice the disappearance of the slope change that was present in both figures 6.2.3 and 6.2.4. It is due to the fact that we should have exposed the surface to longer times of D atoms in order to reach 80%

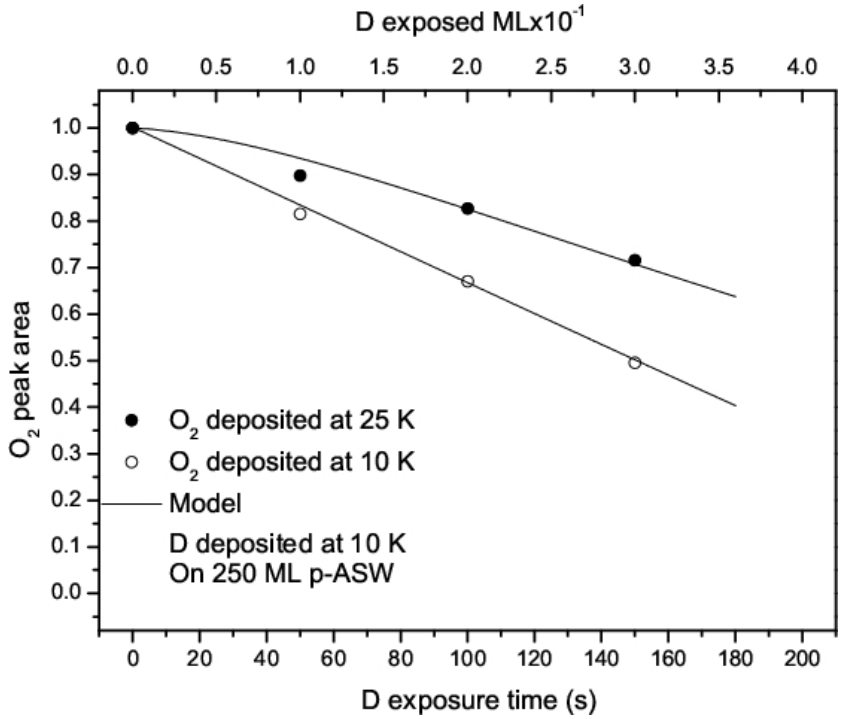


*Figure 6.2.6: Comparison between normalised TPD integrated areas of 0.5 ML of $O_2$ deposited at 10 K (empty circles) and 25 K (plain circles) and then irradiated with 0, 50, 100 and 150 seconds of D atoms on 250 ML of p-ASW at 10 K. The solid line represents the model results (see text).*

of destruction of the adsorbed $O_2$ to observe it.

Finally we have checked, with very large exposure times (600 s) of D irradiation, that all the $O_2$ molecules disappear even on the 250 ML *p*-ASW film, when $O_2$ is deposited at 25 K .

### D deposited before $O_2$

This experiment is made to rule out the assumption that the mobility of D atoms and the $O_2$+D reaction on the surface of the *p*-ASW ice substrate could only be triggered by the heating phase. In fact, G. Vidali and co-workers assume that the diffusion of deuterium and hydrogen atoms on the cold ice surface only takes place during the heating ramp before and during the TPDs. In order to check this assumption, we deposited D atoms before $O_2$. The results are shown in figures 6.2.7 and 6.2.8 for $O_2$ and $D_2$ respectively. In figure 6.2.7 we see that the amount of desorbing $O_2$ from the *p*-ASW ice surface is constant, within the experimental error bars (<10%) irrespective of the amount of D atoms previously deposited. Figure 6.2.8 on the other hand, show that the amount of desorbing $D_2$ increase linearly with respect to the amounts of deposited D atoms on the surface. This means that all D atoms that reach the surface react with each other to form $D_2$ before being exposed to $O_2$ molecules. These results clearly demonstrate that D atoms that adsorb on the ice surface diffuse immediately and either react with each other or desorb before $O_2$ is deposited.

## 6.3 The model

The model we used to fit our experimental data is based on the rate equation model described in Katz et al. (1999). This model calculates the formation rate $N_{D_2}$ of $D_2$ and the destruction rate $N_{O_2}$ of $O_2$ (equal to the formation rate of $O_2D$).

The $O_2$ molecules that are destroyed by the background flux of D atoms (during and after 50 s of D irradiation time) are also taken into account and given by $R_{O_2}$.

The model starts running at time $t$=0 where the number of $O_2$ molecules present on the surface is $L_{O_2}$=0.5 ML, that of D atoms $L_D$=0 and that of $D_2$ molecules $L_{D_2}$=0 as well.

If $F_{tot}$ is the initial beam flux of $D_2$, after the dissociation $F_{tot}$ is divided into a flux of D, $F_D$, and a flux of $D_2$, $F_{D_2}$. Both fluences on the surface are determined knowing the sticking probabilities of $D_2$ and of D, $S_{D_2}$ and $S_D$ respectively (Matar et al. (2009), to be submitted), and the dissociation rate $\tau$ at a beam temperature of 50 K. The fluxes are given by:

$$F_D = 2\tau S_D F_{tot} \text{ and } F_{D_2} = (1 - \tau) S_{D_2} F_{tot}$$

At time $t$+d$t$, the number of D atoms present on the surface then becomes $L_D(t+\mathrm{d}t)=L_D(t)+F_D\mathrm{d}t$. Taking into account the porosity $\rho$ (dimensionless

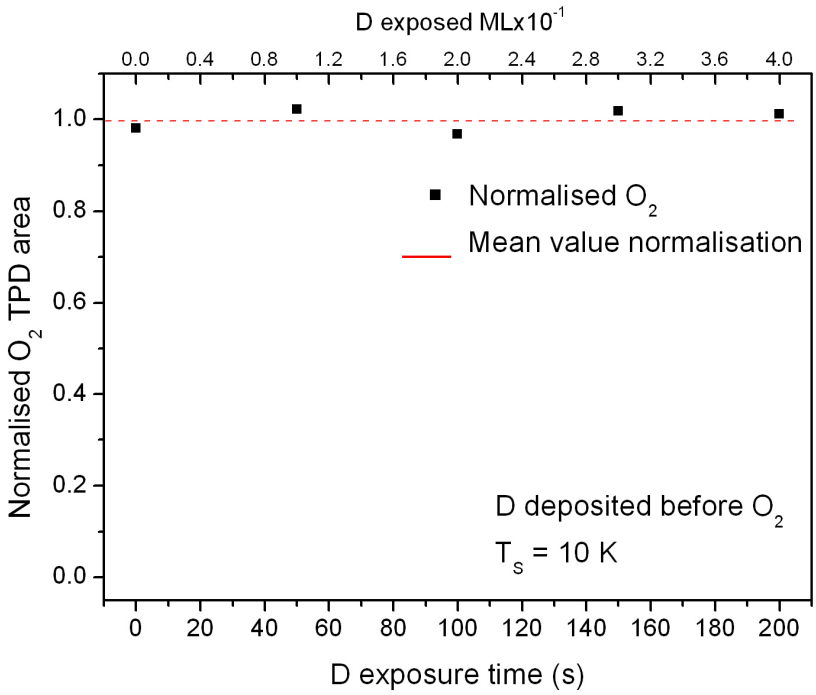


*Figure 6.2.7: Normalised $O_2$ TPD integrated areas for $O_2$ deposited after different D exposures. The $O_2$ normalisation was made with respect to the mean value of all TPD integrated areas. $O_2$ and D both deposited at a surface temperature of 10 K.*

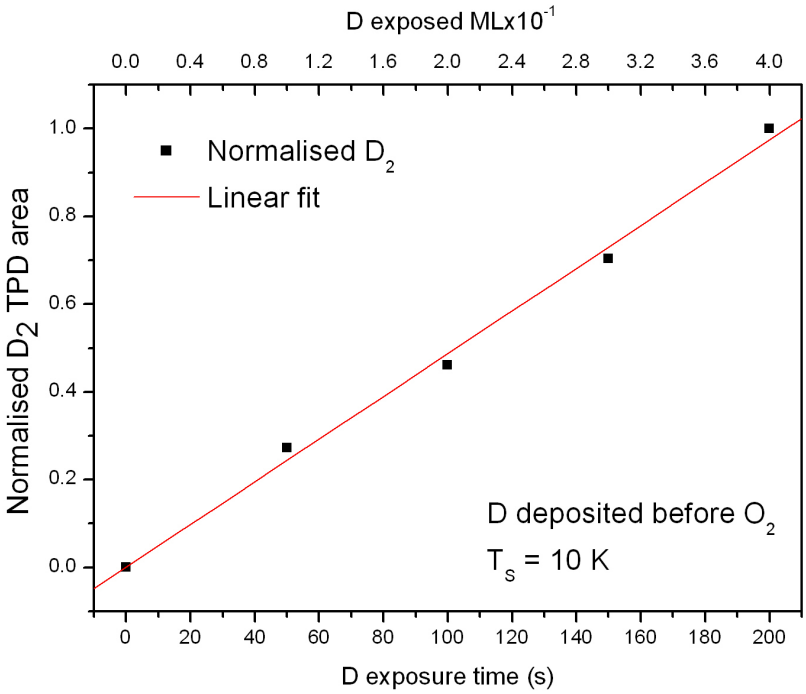


*Figure 6.2.8: Normalised $D_2$ TPD integrated areas for $O_2$ deposited after different D exposures. The $D_2$ normalisation was made with respect to the TPD integrated area corresponding to 200 s of D exposure time. $O_2$ and D both deposited at a surface temperature of 10 K.*

parameter that we introduced in order to control the surface density dependin gon the thickness of the p-ASW ice film) of the *p*-ASW ice substrate, the surface density of D, $D_2$ and $O_2$, the total number of reactions ($D_2$ formation and $O_2$ destruction) is given by:

$$N_{react}\mathrm{d}t = \frac{(L_D+L_{O_2})}{\rho} \times \frac{L_D}{\rho} \times P_{diff}\mathrm{d}t$$

where $\mathrm{P}_{diff} = \mathrm{A}e^{\frac{-E_{diff}}{k_B T}}$ is the probability for a D atom to diffuse from one adsorption site to another, where $\mathrm{A}=10^{13}$ $\mathrm{s}^{-13}$ is the vibration frequency of a deuterium atom, $E_{diff}$ the diffusion barrier, $k_B$ the Boltzmann constant and $T$ the surface temperature (10 K).

The number of formed $D_2$ is then given by:

$$N_{D_2}\mathrm{d}t = \frac{1}{2}\mathrm{N}_{react} \times \frac{L_D}{(L_D+L_{O_2})}\mathrm{d}t$$

and the number of destroyed $O_2$ is given by:

$$N_{O_2}\mathrm{d}t = \mathrm{N}_{react} \times \frac{L_{O_2}}{(L_D+L_{O_2})}\mathrm{d}t$$

The number of D atoms present on the surface at time $t$+d$t$ then becomes

$$L_D(t+\mathrm{d}t) = L_D(t) - 2N_{D_2}\mathrm{d}t - N_{O_2}\mathrm{d}t + F_D\mathrm{d}t,$$

that of $D_2$

$$L_{D_2}(t+\mathrm{d}t) = L_{D_2}(t) + N_{D_2}\mathrm{d}t + \mathrm{F}_{D_2}\mathrm{d}t,$$

and that of $O_2$

$$L_{O_2}(t+\mathrm{d}t) = L_{O_2}(t) - N_{O_2}\mathrm{d}t - R_{O_2}\mathrm{d}t.$$

Where $R_{O_2}$ is the amount of residual $O_2$ destroyed by D atoms coming from the background and which is equal to $\frac{N_{O_2}}{5}$ (20% of $N_{O_2}$ due to the non perfect overlap).

As figures 6.2.3, 6.2.4 and 6.2.6 clearly show, our simple model is able to reproduce the experimental results under the same conditions, namely, dissociation efficiency of the $D_2$ beam, sticking probabilities of D and $D_2$ at 50 K and porosity of the ice. A best fit of the experimental data has given a diffusion barrier of 22±2 meV[4].

[3]In the literature two values for A are normally used, $10^{12}$ $\mathrm{s}^{-1}$ and $10^{13}$ $\mathrm{s}^{-1}$. We use the latter value since previously published work by our team (Amiaud et al., 2006) have shown that it fits better the experimental results in the case of hydrogen and deuterium.

[4]The ±2 meV arise from the fact that the experimental data were fitted with $E_{diff}$=20, 21, 22, 23 and 24 meV, and almost the same fit was obtained. A change in the fits becomes observable below 20 meV and over 24 meV.

## 6.4 Discussions

### 6.4.1 Is atomic hydrogen mobile on icy grains?

In this section I will try to discuss and present additional arguments in favour of D atoms mobility at 10 K on *p*-ASW ice surfaces. If D atoms were not mobile on porous water ice surfaces at 10 K, they should stay in the vicinity of the external surface and not penetrate in the pores of the ice substrate. In addition, the hot atoms mechanism should not take place or should be considerably reduced in our experimental conditions, where D atoms have a kinetic temperature of 50 K.

An important point in the present experiments is that we were working with high coverages. The total number of deuterium atoms sent onto the surface of the *p*-ASW ice is quite high (2 ML *i.e.*, 2 $10^{15}$ atoms.cm$^{-2}$). This amount corresponds to a value of full coverage of the external surface of the substrate. If deuterium atoms were not mobile, all the atoms sticking on the surface of the ice should stay on the surface, thus increasing their number and the surface density should become high. As a consequence, two mechanisms should then become non-negligible and detectable. The first one is the formation due to the Eley-Rideal mechanism where an atom from the gas phase reacts with an already adsorbed deuterium to form a deuterium molecule leading to its immediate release into the gas phase. The second is the Langmuir rejection mechanism (Perets et al., 2005; Vidali et al., 2007) where a deuterium atom, that is deposited from the gas phase on top of an already adsorbed atom on the surface, is rejected and immediately released into the gas phase. In both cases, a fraction of atomic and molecular deuterium evaporates during the irradiation of the surface by the atomic D beam, and therefore does not desorb during the heating phase. If this is the case, the amount of desorbing $D_2$ should not increase linearly for long D exposure times as is the case in figure 6.2.4, but should reach a saturation plateau after a certain coverage of the surface. If D atoms were not mobile on the surface, the Eley-Rideal and the Langmuir rejection mechanisms should become more and more efficient, leading to a constant recombination rate of D atoms on the *p*-ASW ice surface as shown in figure 6.4.1.

In fact, if we consider the D coverage formula used by Vidali et al. (2007):

$$n_D(t)=1 - exp(-f_D.t)$$

where $n_D$ is the total yield of $D_2$ molecules in each TPD run, and $f_D$ is the D atom flux. Applying this expression to our experimental conditions ($f_D$ = 0.01 ML.s$^{-1}$ for D irradiation time ranging from 0 s to 200 s, we find that the recombination rate starts to slow down between ∼40 s and 50 s of D exposure times which is equivalent to ∼0.4–0.5 EML as shown in figure 6.4.1. This is not consistent with our experimental results (fig. 6.2.4), where we see that the recombination rate of D atoms never stops increasing even after a value of full surface coverage or higher (∼600 s *i.e.*, 6 EML of D exposure).

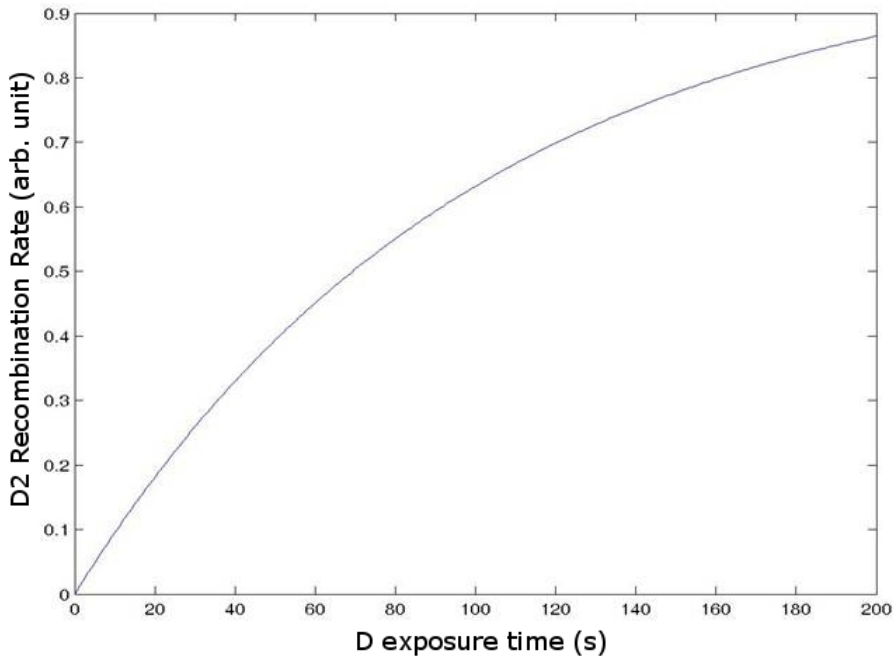


*Figure 6.4.1: Langmuir rejection mechanism of D atoms on p-ASW ice surfaces. If D atoms are not mobile on porous water ice surfaces at 10 K, the recombination rate should become constant after a certain D coverage of the surface.*

| Author | $E_{diff}$ (meV) | $\tau_{diff}$ (s) | $l_{diff}$ (Å) | $T_{gas}$ (K) |
|---|---|---|---|---|
| Matar et al.(08) *(Experiment)* | 22±2 | 1.2 $10^{-2}$ | – | 50 |
| Perets et al.(05) *(Experiment)* | 55 | $10^{14}$ | – | 300 |
| Al-Halabi & van Dishoek (07) *(Th.)* | 20 | $10^{-3}$ | 18 | 200 |
| Buch & Zhang (91) *(Theory)* | 19–34 | 4 $10^{-4}$–1.3 $10^{4}$ | 20 | 200 |
| Takahashi et al. (99) *(Theory)* | 27 | 4 | 60 | 10 |

*Table 6.4.1: Comparison between the results obtained by several authors on the mobility of atomic hydrogen on p-ASW ice surfaces under conditions of dark interstellar clouds.*

We can thus conclude that either the surface density does not increase to reach a value of the coverage close to unity or the two mechanisms mentioned above (Eley-Rideal and Langmuir rejection) are not efficient. However, it is highly improbable that the Eley-Rideal mechanism does not occur under these coverage conditions, therefore the only valid explanation is that the surface density remains low even after 600 s of D irradiation. This implies that D atoms are mobile at 10 K and diffuse through the pores of the *p*-ASW ice substrate.

On the other hand, the calculations done by Buch & Zhang (1991) show that the adsorption energy of both hydrogen and deuterium atoms on a water cluster and the height of the energy barrier between two adjacent sites are both described by large distributions. The diffusion barrier was found to be peaked in the 19.4–34.5 meV range. This means that the mobility depends on the height of the adsorption site. Some deep adsorption sites can bind atoms more than others reducing then their mobility. Thus it is possible that a small fraction of hydrogen atoms are not mobile at 10 K on the time scale of our experiments and require thermal activation in order to react.

In conclusion, the experiments that we have conducted show that, globally, deuterium atoms are able to diffuse and to penetrate the porous structure of the ice at 10 K, even if they have a kinetic temperature as low as 50 K (before they stick on the ice surface). In fact, our model gives a non-infinite D atom mobility, $E_{diff}$=22±2 meV, in good agreement with the calculations of Buch & Zhang (1991) and Al-Halabi & van Dishoeck (2007). Our value is also in good agreement with that found by Takahashi et al. (1999b) (27 meV), even if it is slightly lower. Though the difference between

the two values is somewhat minimal (∼3 meV), it changes dramatically the time needed for a deuterium atom to diffuse from one site to an adjacent one. Our diffusion barrier leads to a mean diffusion time $\tau_{diff}$=12 ms whereas that of Takahashi et al. (1999b) gives a $\tau_{diff}$=4 s. A comparison between the results of the different works is shown in table 6.4.1. This means that on the time scale of our experiments, D atoms diffuse into the porous structure and move from one site to another more rapidly and efficiently leading to an even more efficient formation reaction.

But we should not forget that the value of our diffusion barrier is about half the one obtained by Perets et al. (2005) who found it to be $E_{diff}$=55 meV for deuterium atoms on *p*-ASW ice substrates at 10 K. A possible explanation for the discrepancy between these two results could arise from the different assumptions made on the surface coverage. Despite the fact that the D atoms fluence is about the same in both works (up to 2 ML of D atoms), Perets et al. (2005) assume in their analysis that their coverage is always less than 1% of this value.

### 6.4.2 Consequence of the $O_2$+D reaction efficiency on water formation

Another aspect of these experiments concerns the efficiency of the $O_2$ + D reaction in comparison with the D + D reaction. It has been shown (Miyauchi et al., 2008; Ioppolo et al., 2008) that the reaction

$$O_2 + D \rightarrow DO_2$$

is very efficient. In fact, at the accuracy of our flux estimation (∼50%), the proportion of D required to destroy $O_2$ is close to 1, and the $O_2$+D reaction is believed to have a low energy barrier (Walch et al., 1988). In our experiments the fact that the $O_2$+D reaction seems to be favoured in comparison with the D+D reaction when the exposition is low does not mean that the D + D reaction is less efficient because of an activation barrier. In fact, in our model we have assumed that both D+D and $O_2$+D reactions have 100% efficiency.

Once again, if atoms are mobile, the density of D atoms stays low because they are consumed by the $O_2$ molecules. It is only when the density of D atoms is equal to that of $O_2$ atoms that the production of $D_2$ can be effective. This consideration allows us to conclude that at any moment in our experiment, the density of D atoms is low, initially because they are consumed by $O_2$ and subsequently because they form $D_2$.

At the end of the experiment, when the ice is sublimated we detect a high proportion of HDO and not $D_2O$ owing to thermally activated isotopic exchange between H atoms (from the ice) and D atoms (from $D_2O$) (Smith et al., 1997). Therefore $O_2$ is one of the possible precursors for water formation[5].

[5] $D + O_2 \rightarrow DO_2$ / $DO_2 + D \rightarrow D_2O_2$ / $D_2O_2 + D \rightarrow D_2O + OD$.

Finally these experiments show that no $O_2$ should survive on grains in dark interstellar clouds. Apart from specific detection limitations, it can be a fundamental reason of the non detection of $O_2$ on icy grains in dark clouds.

## 6.5 Some perspectives

### 6.5.1 Thermal hopping *versus* tunnelling effect

Our results are unable to show if the mobility of atomic deuterium on $p$-ASW ice surfaces at 10 K is due to thermal hopping, tunnelling effect or a contribution of both. If the latter case is true, we do not know which mechanism dominates this mobility. In order to understand how this mobility occurs and to have an idea on the contribution of each diffusing mechanism, more experiments should be done on the same water ice surfaces but at lower surface temperatures ($< 8$ K), since tunnelling effect or quantum diffusion is less dependent on the temperature of the surface than thermal hopping.

### 6.5.2 Infrared spectroscopy

The fact that we anneal the $p-$ASW ice substrate to 70 K and cool it back down to 10 K before depositing either $O_2$ or D atoms on the ice and finally do the TPDs reduces considerably the porosity of our ice substrate. This prohibits us to have a true and valid comparison between our results and those of other teams like Perets et al. (2005) for example. These authors grew their porous ice films at a surface temperature of 10 K and the ice was never annealed, the irradiation with H and D atoms was done at a surface temperature of 14.5 K and during the TPD phase the temperature was always below 38 K. Whereas in our experiments, the porous ice is grown at 10 K but annealed to 70 K, and during the TPD phase the temperature of the surface reaches $\sim$65 K. An other experiment can be done to avoid annealing the ice in order to have comparable results and to prove that atomic hydrogen is mobile on porous icy grains at 10 K.

We can proceed the same way Mennella (2008a) did, by depositing $O_2$ before the $p$-ASW ice substrate and then irradiate the whole by cold D atoms. Infrared spectroscopy has to be used *in situ* to see whether any $D_2O$ molecules are formed (via the $DO_2$ formation route (Miyauchi et al., 2008; Ioppolo et al., 2008)). This way the ice preserves its high porosity, and if $D_2O$ molecules are detected, this that D atoms are able to penetrate all the thickness of the ice to reach O2 molecules and react with them.

# Chapter 7

# Formation of molecular hydrogen and energy partitioning

## 7.1 Introduction

After studying and discussing the sticking and the mobility of hydrogen atoms on the surface of amorphous water ices under the conditions of dense molecular clouds, I will discuss in the present chapter the formation of molecular hydrogen on the same ice under the same conditions. I will also shed some light on possible explanations to two important unanswered questions: (i) the partitioning of the energy released upon the formation of an $H_2$ molecule, and (ii) the non-detection of excited $H_2$ in dark quiescent clouds.

### 7.1.1 The energy partitioning problem

In fact, several theoretical and experimental works have been conducted, over the years, on the formation of molecular hydrogen on surfaces of astrophysical relevance, and particularly on the partitioning of its formation energy. The only theoretical calculations relevant to the experimental study presented in this chapter are those of Takahashi et al. (1999a,b). These authors did complete and detailed calculations on the formation of molecular hydrogen on amorphous water ice surfaces and the different processes leading to it (sticking, diffusion, formation and evaporation). For this they used a classical description in a molecular dynamics (MD) formulation for a rigid and a soft water ice samples. These authors found that when a hydrogen molecule is formed, the energy released is divided between vibrational, rotational and translational energies with the following percentages: 70–79% of its energy is transformed to vibrational while 10–15% resides as a rotational energy and 7–12% as a translational energy and that the rest of the 4.48 eV

released is absorbed by the ice substrate.

A previous experimental study by our team (Amiaud et al., 2007) on *np*-ASW ice showed that molecular hydrogen is formed in a ro-vibrationally excited state up to $v$"=7. Experiments on *p*-ASW ice surfaces (Roser et al., 2003; Hornekær et al., 2003) showed that newly formed HD molecules desorb from the surface with a kinetic energy that shows previous thermalisation with the substrate, meaning that some of the released energy was absorbed by the ice. But no information on the internal energy of the formed $H_2$ has been given.

### 7.1.2 The detection problem

Computational studies by Duley & Williams (1986, 1993) on the formation of molecular hydrogen on highly amorphous silicates and carbonaceous grains suggest that the newly formed $H_2$ molecule would be in the highly vibrational excited states since the $H_2$ binding on these surfaces is weak. On the other hand, they found that $H_2$ formed on PAH grains would be in the lowest vibrational excited states because of the strong binding of $H_2$ on these surfaces. These authors also suggested that vibrational emission might be detectable in dark clouds where $H_2$ is known to be formed on amorphous ice mantles with very high vibrationally excited states because of the very weak binding.

Observations by Usuda (1996) claimed that the intensity and the origin of the $H_2$ emission spectrum cannot be explained only by UV pumping and dynamical excitation, suggesting that the population for vibrational energy levels of $v$>2 should increase because of the formation pumping mechanism. For this reason, these authors suggest that the vibrational emission might be detectable even in dark clouds where $H_2$ molecules are formed on icy mantles (Duley & Williams, 1986, 1993). It is also suggested that, in these regions, rotationally and translationally excited $H_2$ might be detectable.

Takahashi et al. (1999a)'s MD calculations on the formation of $H_2$ and the distribution of its released energy, revealed the importance of the formation pumping mechanism for the production of $H_2$ in highly excited states ($v$"=6–10) in the conditions of dark clouds where $T_{grain}$=$T_{gas}$=10 K.

In principle, the observation of nascent $H_2$ molecules in the interstellar medium, especially in dark quiescent clouds, should be possible. Once formed, in a ro-vibrationally excited state, an $H_2$ molecule will de-excite by spontaneous radiative cascade transitions to lower energy levels. Then infrared emission occurs and should be detectable. Tiné et al. (2003) predicted an observational spectrum for newly formed excited $H_2$ that should have a clear spectral signature both in diffuse and dark clouds. But when they did their observations of the two dark clouds L1498 and L1512 to compare them with their predictions they did not detect any excited $H_2$ molecules. Similarly, observations of Barnard 68 (or Lynds Dark Nebula LDN 57) have been made as part of the programme ref 66.C-0526(A) in March 2001 at ESO-VLT

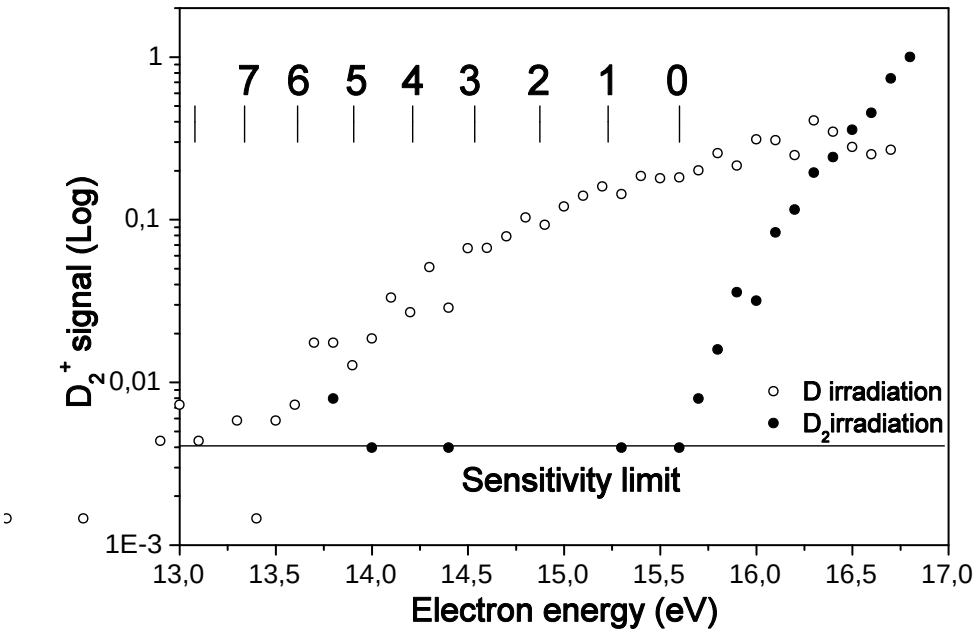


*Figure 7.1.1: Ionisation threshold of excited $D_2$ molecules formed on the surface. plain circles are for $D_2$ irradiation and empty circles are for D irradiation ($D+D_2$) (Amiaud, 2006).*

using the ISAAC instrument in spectroscopic mode by Lemaire & Field (private communication). No detection of $H_2$ emission has been observed looking at the core of the object in K band, despite a 5-hour integration in nodding mode to subtract the telluric lines.

## 7.2 The Experiments

### 7.2.1 Introduction

In order to detect if molecules in an excited vibrational state of the ground electronic state are produced in our experiments, we have made use of a specific feature of the quadrupole mass spectrometer (QMS).

To be detected, $D_2$ molecules are ionised by electrons emitted from the filament in the ionising head of the QMS. The kinetic energy of electrons emitted in the ionisation zone is usually set to 30 eV. By varying this energy to smaller values it is possible to detect molecules in a vibrationally excited state. $D_2$ molecules in the ground state have an ionisation threshold of 15.46 eV. Excited $D_2$ molecules need lower energy electrons to be detected.

Then by setting the electron energy to a value smaller than 15.46 eV, we are able to detect solely internally excited molecules. Previous experiments conducted by our group (Amiaud et al., 2007) reveal the presence of excited $D_2$ molecules up to $v$"=7. In fact a non-negligible number of detections were carried out down to the value of 13.6 eV. A faint signal is still recorded at 13.4 eV corresponding to $v$"=7 (fig 7.1.1).

For the experiments reported in this chapter, the detection of excited $D_2$ was performed with an ionising electron energy equal to 15.2 eV, allowing us to detect molecules in a vibrationally excited state $v$"$\geq$2.

Excited nascent $D_2$ molecules are studied on three different types of amorphous solid water (ASW) ice substrates:

1- 100 ML of bare *np*-ASW,

2- 100 ML of the same ice previously saturated with $D_2$ molecules and

3- 10 ML of *p*-ASW.

In all cases the surface temperature is held at 10 K.

The experiments consist on irradiating the substrates by D atoms. $D_2$ molecules are then detected by the QMS in real-time mode. The QMS was located 5 cm above the surface, therefore only indirect measurements of nascent molecules is performed. For each sample measurements are made twice: the first experiment done with ionising electron energy equal to 30 eV to record the signal of $D_2$ reflected from the surface (non-dissociated part+formed/excited part), and the second experiment with ionising electron energy of 15.2 eV to record the signal of newborn excited $D_2$ molecules only. The dissociation rate of the $D_2$ beam was checked to be constant during the whole time of the experiments and was equal to 60% (100 $D_2 \rightarrow$ 120 D + 40 $D_2$). The resulting D atoms are thermalised to room temperature ($\sim$ 300 K) due to collisions with the wall of the Polytetrafluoroethylene (PTFE) tube and the aluminium nozzle guiding them out of the microwave source.

### 7.2.2 Bare *np*-ASW ice

The results of the experiment done on the bare *np*-ASW are shown in figure 7.2.1. The blue curve is the total amount of $D_2$ being reflected from the surface and the red curve is that of excited $D_2$ only.

In the blue curve, we distinguish three regimes in the evolution in time of the total $D_2$ molecules: (a) a steep linear increase of the signal during the first 150 s of D irradiation, followed by (b) a less step increase in the signal untill $\sim$600 s and finally (c) a plateau where the signal stays constant at its maximum during the rest of the experiment as long as we irradiate the surface with D atoms. They are analysed as follows:

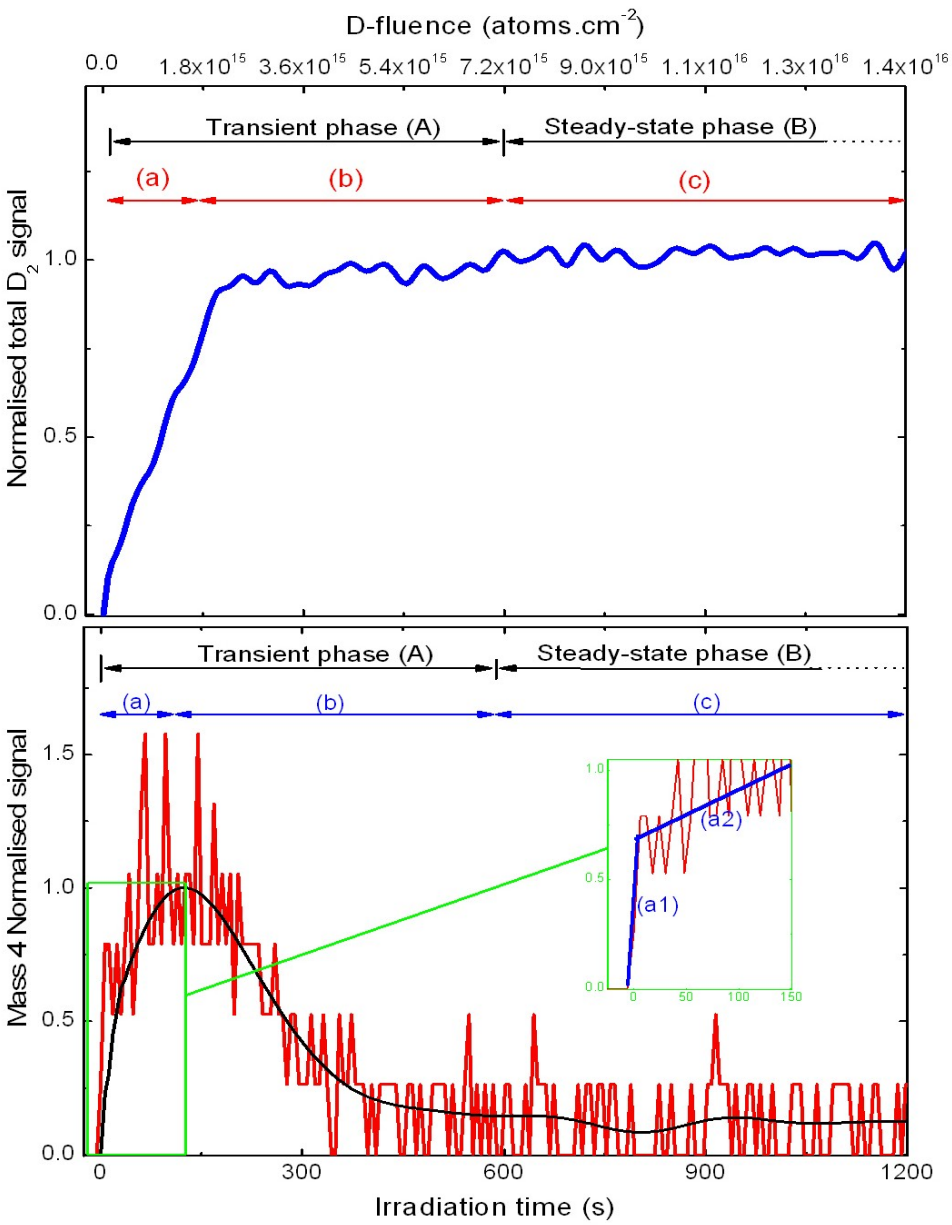


*Figure 7.2.1: Normalised total $D_2$ signal (blue curve, QMS at 30 eV) and excited $D_2$ signal (red curve, QMS at 15.2 eV) monitored during D irradiation of 100 ML of bare np-ASW ice substrate at 10 K. The black curve is a 20 s FFT smoothing of the excited $D_2$ signal. The inset shows a zoom of the first 150 seconds.*

(a)- The first regime, where the linear increase is rough, is the signature of a growing and enhanced $D_2$ formation. In fact, the adsorption energy of the non-dissociated part of the $D_2$ beam (40%) enhances the sticking coefficient of D atoms as we have seen in chapter 5 and as also explained by Schutte et al. (1976) and Govers et al. (1980). After the irradiation has begun at $t$=0, few atoms are expected to stick although those that are adsorbed on the bare surface can occupy the deeper binding sites. This results in a long residence time that favours the recombination between hydrogen atoms.

(b)- When the coverage of the *np*-ASW surface by $D_2$ molecules becomes close to the saturation coverage ($\sim$1.8 $10^{14}$ molecules.cm$^{-2}$), we see that the signal becomes less steep. This change in the slope is explained by a slow increase of the formation rate of $D_2$ on the surface. When molecules gradually fill up the ice substrate, the binding energy of adsorbed atoms decreases gradually as the molecules saturate the stronger binding sites (Hixson et al., 1992). In fact, this formation regime is highly dependent on the coverage of the surface by $D_2$ molecules coming from the non-dissociated part of the beam. As we have seen in chapter 5, when the surface approaches saturation, the sticking coefficient of $D_2$ molecules starts to decrease forcing the recombination rate of D atoms to become slower than in the first stage where the surface coverage was still low.

(c)- Finally, when the amount of sticking molecules becomes constant, after $\sim$600 s of D irradiation time, we reach a steady-state regime (plateau) where the amount of formed/deposited $D_2$ molecules on the surface becomes equal to the amount of $D_2$ molecules desorbing from it. Therefore the $D_2$ formation rate becomes constant.

This interpretation can be confirmed by looking at the red curve in figure 7.2.1 which is the signal of excited $D_2$ molecules only, that also presents three different regimes for the same time-scales than for the blue curve: (a) the rough rise of the signal that can be divided into two steps (a1) and (a2) (see below), this increase is followed by (b) a decrease after reaching a maximum at $\sim$ 150 seconds of D irradiation time and then (c) the signal reaches a plateau after $\sim$600 s of D irradiation. They are analysed as follows:

(a)- In this regime we can distinguish two sub-regimes (see the green inset): (a1) where the signal of newly formed excited $D_2$ increases dramatically during the first 4 s of D irradiation. During this rise, less than 2% of the surface is covered by D atoms. In these conditions of atomic coverage, the recombination rate is very high because the surface is still clean of $D_2$ molecules. In these first seconds the surface is cleaning itself very efficiently because each formed molecule is released directly into the gas phase leaving the surface clean.

In these coverage conditions, the formation due to the Eley-Rideal mechanism is highly improbable. Considering that the cross section of an Eley-Rideal reaction is equal to ∼10 Å$^2$, only 2% of the gas phase atoms interact with already adsorbed ones and lead to the formation of a $D_2$ molecule. This means that the most probable formation reaction is that due to the Langmuir-Hinshelwood mechanism, a fact that we have seen in the previous chapter. The mobility of D atoms is very high at a surface temperature of 10 K to allow a very efficient formation with a diffusion time between two neighbour adsorption sites equal to 12 ms for porous ice (of course this time is a lot less for non-porous ice). But after ∼4 s (a2) the $D_2$ coverage of the surface starts to play a role slowing down the recombination rate which makes the increase less steep. In this first regime (a), nascent molecules are then released into the gas phase (rise of the signal in the red curve) contributing to the increase of the total signal of detected $D_2$ (regime (a) in the blue curve).

The peak in the excited $D_2$ signal indicates a high recombination probability resulting from an optimum equilibrium between the increase of the sticking efficiency and the shortening of the residence time of D atoms on the surface as this was explained in the previous paragraph. The surface coverage at this stage is ∼1.0 $10^{14}$ molecules.cm$^{-2}$. As pointed out by Govers (2005), around this molecular coverage we observe an abrupt change in the binding energy of atoms, in that it begins to decrease as the surface coverage with $D_2$ molecules grows further.

(b)- The drop of the signal of excited $D_2$, after it reaches a maximum at ∼150 s, coincides with the decrease in the recombination rate found in regime (b) in the blue curve. Then it rapidly reaches (c) a steady-state regime after ∼500 s also coinciding with the regime (c) of the blue curve. This decrease in excited $D_2$ signal does not mean that we are not forming $D_2$ molecules anymore but that the newly formed excited $D_2$ de-excite rapidly before being released into the gas phase. This de-excitation might be due to the presence of a high coverage of already adsorbed $D_2$ on the ice surface. With this observation we suggest that the nascent $D_2$ molecules may undergo a thermalisation with the surface by loosing their internal energy via efficient energy transfer due to the enhanced number of molecules on the surface. A large amount of $D_2$ is formed in an excited state but promptly release their internal energy on the surface via an efficient energy transfer that involves the favourable mass ratio between newly formed molecules and the molecules adsorbed in the vicinity (Schutte et al., 1976). The already adsorbed molecules can in turn use part of this energy to desorb from the substrate in a non-excited state via a non-thermal desorption process or by simple thermal desorption due to the increase of the surface coverage.

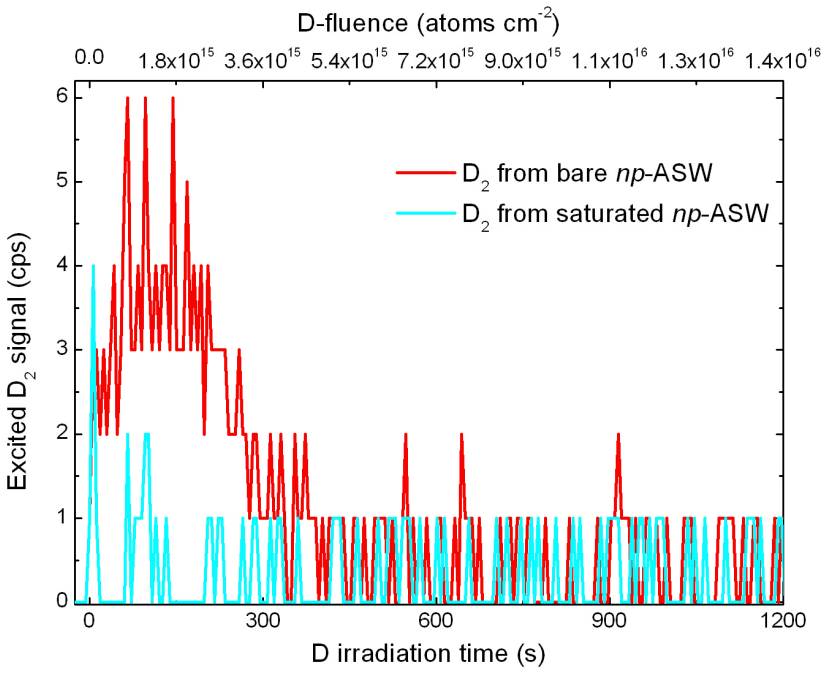


*Figure 7.2.2: Excited $D_2$ signals monitored during D irradiation of 100 ML of np-ASW ice substrate at 10 K. The red curve is that of the bare np-ASW ice and the cyan curve is that of the same np-ASW ice saturated by $D_2$ molecules before the D irradiation.*

(c)- The signal of excited $D_2$ attains a low-count plateau and stays as such in a regime of saturation of the surface, that is to say under conditions close to those of the dense regions of the interstellar medium.

We should note that several experiments have been done by irradiating the ASW ice surface to $D_2$ molecules instead of D atoms (i.e. no $D_2$ formation in progress) and by exposing the surface at a higher temperature to D atoms (i.e. the residence time of atoms becomes then too short for recombination to be efficient) to verifiy if excited $D_2$ can be detected, but, in both cases, we did not detect any excited $D_2$ molecules. So the recorded low-count plateau value of the ro-vibrationally excited $D_2$ molecules should not be considered as a mere instrumental noise, but as a real measurable signal.

### 7.2.3 $D_2$ saturated *np*-ASW ice

This experiment is done to prove our interpretation of the behaviour of excited $D_2$ molecules found in the first experiment: the role of the already adsorbed $D_2$ molecules on the surface in the de-excitation of newly formed $D_2$. For this we saturate the same *np*-ASW ice surface by exposing it to

20 minutes of $D_2$ molecules which is equivalent to ∼10 EML, and then we irradiated it with D atoms. However it should be noted that, due to the reduced sticking coefficient of $D_2$ molecules and the reduced binding energy when the saturation of the surface at 10 K is achieved, only a fraction (20%) of the *np*-ASW ice surface is covered with molecules. Figure 7.2.2 clearly shows that the excited $D_2$ signal in the case of a surface with molecules pre-adsorbed on the *np*-ASW substrate (cyan curve) is much lower than in the first case (red curve) and a low-count plateau is attained rapidly right after we begin irradiating the surface by D atoms.

### 7.2.4 *p*-ASW ice

An uncertainty arises when we mention the structure of the ice mantles covering the interstellar dust. Until now no firm conclusions exist concerning the subject and no experiments, theories or observations have given any information whatsoever on the morphology of the amorphous ice surfaces of dust grains. It can be compact (*np*-) ASW ice, or it can be porous ($p-$) ASW ice with a porosity ranging from high-density substrates (∼1.1 g.cm$^{-3}$) below 38 K to low-density (∼0.94 g.cm$^{-3}$) substrates above 68 K (Jenniskens & Blake, 1994).

For this reason we have repeated the first experiment on 10 ML of *p*-ASW ice substrate. The results of this experiment are shown in figure 7.2.3. As in figure 2, the blue curve is the signal of total $D_2$ molecules reflected from the surface and recorded by the QMS in real-time mode, and the red curve is that of excited molecules only. The black curve is the signal of excited $D_2$ obtained when irradiating the *np*-ASW ice from figure 7.2.1 shown for comparison.

As we know, when we are dealing with a porous substrate, the effective surface is considerably large compared to that of the *np*-ASW substrate. This means that the time needed for adsorbing $D_2$ molecules to saturate the porous surface becomes much longer. This is why the rise of the total $D_2$ signal (blue curve) is very slow and the plateau is reached after ∼1200 s instead of ∼120 s (see fig. 7.2.1). As we have seen in the case of the *np*-ASW substrate, the excited-$D_2$ signal (red curve) is likewise proportional to the total yield of $D_2$ molecules until a maximum is reached after around 1000 s of D-atom irradiation, concurrent with a fast rise of the molecular formation efficiency (slope of the total-$D_2$ signal). This is in agreement with the assumption made earlier that, in a regime of low coverage, the number of excited-$D_2$ molecules is proportional to the total number of nascent molecules. However, the peak detected in the case of *p*-ASW is so small that it barely stands out from the excited-$D_2$ low-count plateau value that is attained right after the maximum (at $t \approx 1200$ s). To emphasize the big difference between the amount of ro-vibrationally excited molecules detected in the two types of water ice substrates investigated (*np*- *vs* *p*-ASW), the excited-$D_2$ yield curve of the porous substrate case (red curve) and the excited-$D_2$ yield curve

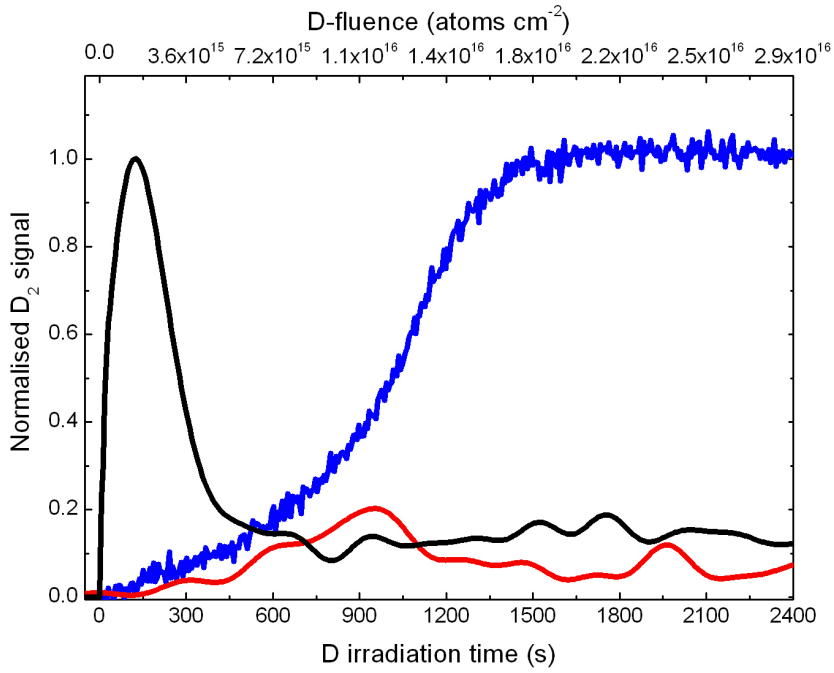


*Figure 7.2.3: Normalised total $D_2$ signal (blue curve) and excited $D_2$ signal (red curve) monitored during D irradiation of 10 ML of bare p-ASW ice substrate at 10 K. The black curve is that of the irradiation of the np-ASW shown here for comparison with the red curve.*

of the non-porous surface case (black curve) are both shown in figure 7.2.3. To facilitate a direct comparison, the red curve (porous case) was scaled by the same factor used for normalising the black curve (non-porous case, fig. 7.2.1). From this comparison, it is clear that the excited-$D_2$ yield is considerably reduced in the case of the p-ASW substrate. This result implies that the excited nascent molecules readily thermalise with the substrate as they form in the pores of the *p*-ASW film.

Hornekær et al. (2003) measured the kinetic energy of HD molecules formed on the surface and found that they fully thermalise with the porous surface before desorbing. In this work we show that also the internal energy of newly formed $D_2$ molecules that rapidly desorb is deposited almost completely in the porous ice. In fact, hydrogen atoms are mobile at 10 K and penetrate the porous structure (previous chapter (Matar et al., 2008), thus nascent molecules are re-captured several times within the pores. This explains why we do not observe significant internal or kinetic energy in the desorbing molecules.

## 7.3 Conclusions

### 7.3.1 From the experiments

$D_2$ is formed on ASW ice surfaces in high vibrational excited states (at least $v$=7) and immediatly de-excite releasing a large amount of its internal energy into the ice substrate before desorbing. Unfortunately we are not able to give an estimate of the fraction of the energy deposited in the ice substrate. Yet, qualitative indications are that it is greater than what has been predicted by Takahashi et al. (1999a) which is around 5% of the entire formation energy but comparable to the value between 40% and 60% found by Creighan et al. (2006) in the case of graphite and Yabushita et al. (2008b) in the case of $H_2$ formation by water photolysis.

The present experiments demonstrate that two conditions contribute to the relaxation of nascent hydrogen molecules formed on the surface of amorphous water ice. On *np*-ASW, newly formed $D_2$ molecules promptly de-excite as the surface coverage reaches saturation in $D_2$ at 10 K. On *p*-ASW, we found that the signal of excited $D_2$ is always low and basically independent of the surface coverage, indicating that the porosity of the substrate contributes efficiently to the relaxation of nascent $D_2$ molecules.

### 7.3.2 Consequences for astrophysics

We can actually assess if, under interstellar conditions of interest here, surface coverage and surface morphology are comparable to those simulated in our experiments. To estimate the surface coverage on interstellar dust

grain we have to verify that the lifetime $\tau$ of a molecule on the surface is comparable to the time interval $\Delta t$ between the arrival of two molecules on a single dust grain surface; i.e., that the arrival rate balances the evaporation rate.

Let us consider the time interval between the impacts of two molecules on the surface of a dust grain. Typical conditions of the dense quiescent medium are $T_{gas} \sim T_{grain} = 10$ K, density $n_{H_2} = 10^4$ cm$^{-3}$, and for our calculation we can approximate the dust grains to spheres with average radius $r_{grain} = 0.1\,\mu$m. Then we have

$$\Delta t = (n_{H_2}\,\bar{v}\,A/4)^{-1}.$$

$\bar{v}$ is the mean velocity of the molecules and $A$ is the grain surface accessible to the molecules in the gas phase. Under dense cloud conditions $\Delta t$ turns out to be of $\sim 6$ hours.

The residence time $\tau$ is expressed as $\tau = 1/\nu_0 \exp(E_a/T_s)$. $\nu_0$ is the vibration frequency of a molecule on the surface and represents the number of attempts per second to evaporate ($\nu_0 = 10^{13}$ s$^{-1}$). $E_a$ is the adsorption energy in units of Kelvin and $T_s$ is the surface temperature. The surface temperature in our case is 10 K so the residence time of $H_2$ molecules on the grain surface depends critically on the adsorption energy. Amiaud et al. (2007) derived the distribution of $E_a$ from $D_2$ TPD spectra in a saturation regime on np-ASW at 10 K. They found that $E_a$ ranges from about 400 to 700 K (33 to 59 meV) and estimated the saturation coverage to be $\sim$1.8 $10^{14}$ molecules.cm$^{-2}$. Putting $E_a = 400$ K in the expression of $\tau$ (corresponding value for the lesser bound molecules) we find a residence time of $\sim 6.5$ hours, and thus $\Delta t \approx \tau$.

By scaling $E_a$ to a lower value suitable for $H_2$, presumably comprised between 360 and 650 K (Vidali, 1991), we find a minimum value for $\tau$ of around 10 minutes which does not impair the validity of our conclusion as the fraction of weakly bound $H_2$ ($E_a < 400$ K) does not account for more than a few percent of the total surface population (e.g., Hixson et al. (1992)).

The surface molecular coverage on interstellar dust grains in dark clouds can then be estimated to be in the range 1.5 - 2 $10^{14}$ molecules.cm$^{-2}$, a value consistent with previous estimates by Govers et al. (1980) and Buch & Devlin (1994) and comparable to the surface coverage we reach in our experiments. In addition, since dust grains residing in dark clouds are covered by icy mantles of many monolayers dominated by water ice, as in the present work, our results are relevant to the excited newly formed $H_2$ molecules in dark clouds. If we assume a non-porous ice substrate covering cosmic dust grains, we have shown that the fraction of newly formed excited $H_2$ molecules is considerably reduced in the gas phase. Should the surface of dust grains in dark clouds be covered with a porous water ice mantle, the binding energy of the H-H reaction is released on the surface even more efficiently owing to the pores that trap the molecules long enough so that

they de-excite inside the pores before leaving the grain.

### 7.3.3 Further ideas

The part of the formation energy that is deposited into the grain can have several effects:

(1) trigger the formation of other molecules on the grain,

(2) lead to the desorption of species that are adsorbed in a neighbour site

(3) play an important role in changing the morphology of the ice mantles from porous to non-porous.

This last point is not certain and is yet to be verified. In fact, preliminary experimental results obtained in our laboratory (Accolla et *al*. *In preparation*), have shown that in dark quiescent clouds, if the ice found on the grain or accreting from the gas phase on it has a porous structure, this ice progressively undergoes a morphological transformation from porous to non-porous (Fig. 7.3.1). This change is due, together with UV processing, ion and CR bombardment, to the adsorbing species and the chemical reactions taking place on the surface. The formation of molecular hydrogen for example being one of these processes if not the most important. If this assumption is true, then the non-detection of excited $H_2$ in dark quiescent clouds is explained by experiments done both on *p*- and *np*-ASW ice surfaces.

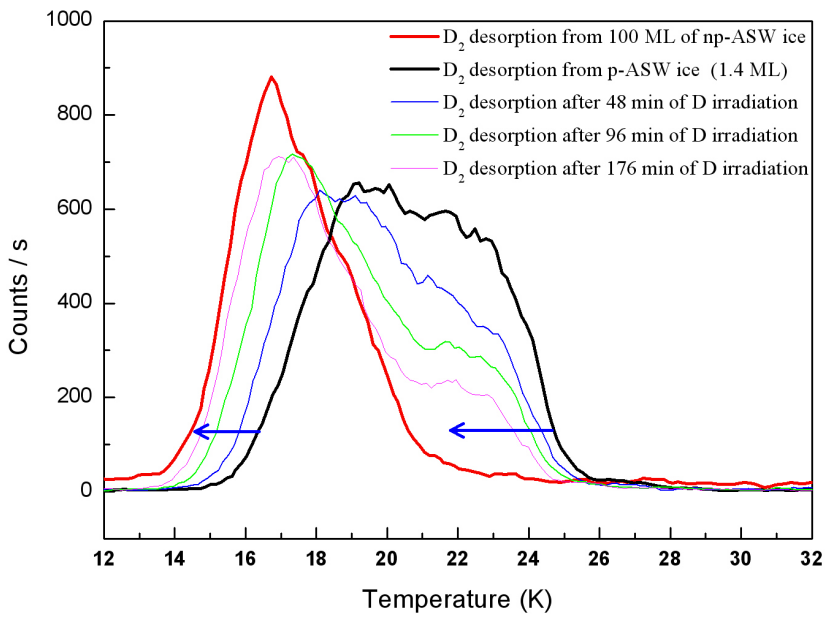


*Figure 7.3.1: By looking at the position of $D_2$ TPD peaks, we can see the morphological transformation of ASW ice from p- to np-ASW after increasing D irradiation times. (From Accolla et al. (2009), in preparation).*

# Chapter 8

# Conclusion

Even if most of the conditions dominating in the interstellar medium are orders of magnitudes below those that we can reach in the laboratory at the exception of temperature (density, flux, time scale,...), and even if information concerning several components, such as the interstellar grains, the morphology of the ice and its constituents etc., are very limited still, experimental astrophysics plays an important role to decipher and interpret what the astronomers are observing, in our case the ISM. It allows to identify the processes taking place there, to understand them and to measure the key parameters ruling them (sticking coefficients, diffusion barrier, ...).

The results presented in this thesis have been done using the FORMOLISM experimental set-up. This semi-heavy experiment has been completed in 2004 and is fully operational for scientific purposes since 2005. It is evolving year after year in order to improve its performance.

During this thesis, the measurement and the control of the first beam's temperature have been modified and improved in order to reach lower temperatures and to monitor them more precisely.

Until now we are not sure of the morphology of the water ice films that cover the interstellar dust grains. We know that in dark clouds water ice mantles are amorphous and that the grains can be covered with several layers of ice. But we do not know if these mantles are porous or non-porous. This is why we are conducting our experiments on both types of ice. This thesis work uncovers additional pieces of the puzzle and is a follow-up of the thesis work done by Amiaud (2006).

It is true that the ice mantles that cover the dust grains in the interstellar medium are not composed of pure water ice but other molecular components such as $CH_3OH$, $NH_3$, CO and $CO_2$ also exist. These impurities can of course have some influence on the sticking of atomic and molecular hydrogen, and on the adsorption, diffusion, formation and desorption kinetics.

A detailed study of the sticking process of H and D molecules, using the King and Wells method, showed that the sticking coefficient of species is highly dependent on the kinetic temperature of the beam.

We find that under conditions of dense molecular clouds, the sticking coefficient is equal to 82% for $D_2$ and 75% for $H_2$ on non porous amorphous water ice films. The experimental results are fitted with a simple rate equation model. The sticking coefficients of H and D atoms are found by extrapolating the experimental data of $D_2$ and $H_2$ and are found to be equal to 99% for D and 97% for H atoms. We also find that the variation of the sticking coefficient with temperature follows a bell-like curve and does not have an exponential behaviour as it was suggested by Buch & Zhang (1991) and Al-Halabi & van Dishoeck (2007).

We propose a method to experimentally measure the sticking coefficients of molecular and atomic H and D on porous amorphous ice. The obtained results are then used in experiments to study the mobility of atomic D on porous amorphous water ice films.

An other important process leading to the formation of $H_2$, along with the hydrogenation of other molecular species, on the icy grains is also studied.

The experiments show that atomic D is mobile on porous amorphous water ice surfaces at 10 K. The experiments are done by depositing $O_2$ on 20 ML and 250 ML of porous water ice films and then exposing them to D atoms. We find that, even in the latter case, the diffusion of D atoms is detectable. By fitting the experimental results with a rate equation model identical to that presented by Katz et al. (1999), we find that the diffusion barrier is equal to 22±2 meV which is equivalent to a hopping time of the order of 10 ms from one adsorption site to a neighbour one. The experimental method that we use (irradiation of $O_2$ by D atoms) shows a very efficient $D_2O$ formation (and also HDO due to the isotopic exchange during the heating phase) via the $DO_2$ formation route.

However, for the time being no information is available whether this mobility is due to thermal hopping or tunnelling effect and other experiments are suggested that can shed some light on the subject.

In the last chapter of this thesis, I present experiments on the formation of $H_2$ and its de-excitation. These experiments are intended to shed some light on the partitioning of the energy (4.48 eV) that is liberated upon formation of $H_2$ on icy interstellar dust grains as well as on its detection problem in interstellar dark clouds.

Three sets of experiments are conducted: irradiation with D atoms of (1) a bare non-porous ASW ice film, (2) a $D_2$ saturated non-porous ASW ice film and (3) a porous ASW ice film. As a result, we find that $D_2$ is formed in high vibrational excited states (up to $v$"=7) and that it immediately de-excite before desorbing for two reasons: (1) the molecular

coverage of the surface and (2) the porosity of the ice. On *np*-ASW, newly formed $D_2$ molecules promptly de-excite as the surface coverage reaches saturation at 10 K. On *p*-ASW, we find that the signal of excited $D_2$ is always low and basically independent of the surface coverage, indicating that the roughness of the substrate contributes efficiently to the relaxation of nascent $D_2$ molecules. We also find that almost 90% of the liberated energy is deposited into the ice both in the porous and the non-porous cases. These results might explain why the attempts of several astronomer teams to detect excited newly formed $H_2$ in dark quiescent clouds were unsuccessful.

In conclusion, the experimental studies conducted with FORMOLISM and presented in this PhD thesis allowed us to explore certain fundamental properties of the gas-surface interaction, and to investigate the processes that lead to the formation of molecular hydrogen. The water ice samples used in these works, at 10 K, are pure amorphous water ice films (porous and non-porous) mimicking the ice mantles that cover the interstellar dust grains.

# Bibliography


Al-Halabi, A. & van Dishoeck, E. F. (2007). Hydrogen adsorption and diffusion on amorphous solid water ice. *MNRAS*, **382**, 1648–1656.

Al-Halabi, A., Kleyn, A., van Dishoeck, E., & Kroes, G. (2002). Sticking of Hydrogen Atoms to Crystalline Ice Surfaces: Dependence on Incidence Energy and Surface Temperature. *J. Phys. Chem. B*, **106**, 6515–6522.

Amenomiya, Y. & Cvetanovic, R. J. (1963). Application of flash-desorption method to catalyst studies. I. Ethylene-Alumina system. *J. Phys. Chem.*, **67**, 144–147.

Amiaud, L. (2006). *Interaction d'atomes et de molécules d'hydrogène avec des glaces d'eau à très basse température : formation de $H_2$ dans le milieu interstellaire.* Ph.D. thesis, Observatoire de Paris-Meudon, Université de Cergy-Pontoise 2006.

Amiaud, L., Fillion, J. H., Baouche, S., Dulieu, F., Momeni, A., & Lemaire, J. L. (2006). Interaction of $D_2$ with $H_2$ amorphous ice studied by temperature-programed desorption experiments. *J. Chem. Phys.*, **124**(9), 094702.

Amiaud, L., Dulieu, F., Fillion, J.-H., Momeni, A., & Lemaire, J. L. (2007). Interaction of atomic and molecular deuterium with a nonporous amorphous water ice surface between 8 and 30 K. *J. Chem. Phys.*, **127**(14), 144709–+.

Attard, G. & Barnes, C. (1998). *Surfaces.* Oxford University Press. ISBN 0-19-855686-1.

Bar-nun, A., Herman, G., Laufer, D., & Rappaport, M. L. (1985). Trapping and release of gases by water ice and implications for icy bodies. *Icarus*, **63**, 317–332.

Bar-Nun, A., Dror, J., Kochavi, E., & Laufer, D. (1987). Amorphous water ice and its ability to trap gases. *Physical Review B*, **35**(5), 2427–2435.

Bauschlicher, Jr., C. W., Liu, Y., Ricca, A., Mattioda, A. L., & Allamandola, L. J. (2007). Electronic and Vibrational Spectroscopy of Diamondoids and

the Interstellar Infrared Bands between 3.35 and 3.55 $\mu$m. *ApJ*, **671**, 458–469.

Biham, O., Furman, I., Katz, N., Pirronello, V., & Vidali, G. (1998). H_2 formation on interstellar grains in different physical regimes. *MNRAS*, **296**, 869–872.

Boogert, A. C. A., Schutte, W. A., Tielens, A. G. G. M., Whittet, D. C. B., Helmich, F. P., Ehrenfreund, P., Wesselius, P. R., de Graauw, T., & Prusti, T. (1996). Solid methane toward deeply embedded protostars. *A&A*, **315**, L377–L380.

Boogert, A. C. A., Ehrenfreund, P., Gerakines, P. A., Tielens, A. G. G. M., Whittet, D. C. B., Schutte, W. A., van Dishoeck, E. F., de Graauw, T., Decin, L., & Prusti, T. (2000). ISO-SWS observations of interstellar solid $^{13}CO_2$ : $heatediceandtheGalactic^{12}C/^{13}Cabundanceratio. A\&A, \mathbf{353}, 349 - -362.$

Brooke, T. Y., Sellgren, K., & Geballe, T. R. (1999). New 3 Micron Spectra of Young Stellar Objects with H_2O Ice Bands. *ApJ*, **517**, 883–900.

Buch, V. (1992). Growth and structure of amorphous ice condensates: A computational study. II). *J. Chem. Phys.*, **96**(5), 3814–3823.

Buch, V. & Devlin, J. P. (1991). Spectra of dangling OH bonds in amorphous ice: Assignment to 2- and 3-coordinated surface molecules. *J. Chem. Phys.*, **94**(5), 4091–4092.

Buch, V. & Devlin, J. P. (1994). Interpretation of the 4141 inverse centimeters (2.415 microns) interstellar infrared absorption feature. *ApJ*, **431**, L135–L138.

Buch, V. & Zhang, Q. (1991). Sticking probability of H and D atoms on amorphous ice - A computational study. *ApJ*, **379**, 647–652.

Burke, J. R. & Hollenbach, D. J. (1983). The gas-grain interaction in the interstellar medium - Thermal accommodation and trapping. *ApJ*, **265**, 223–234.

Carruthers, G. R. (1970). Rocket Observation of Interstellar Molecular Hydrogen. *ApJ*, **161**, L81+.

Chiar, J. E., Gerakines, P. A., Whittet, D. C. B., Pendleton, Y. J., Tielens, A. G. G. M., Adamson, A. J., & Boogert, A. C. A. (1998). Processing of Icy Mantles in Protostellar Envelopes. *ApJ*, **498**, 716–+.

Collings, M. P., Dever, J. W., Fraser, H. J., & McCoustra, M. R. S. (2003). Laboratory studies of the interaction of carbon monoxide with water ice. *Astrophysics and Space Science*, **285**, 633–659.

Collings, M. P., Anderson, M. A., Chen, R., Dever, J. W., Viti, S., Williams, D. A., & McCoustra, M. R. S. (2004). A laboratory survey of the thermal desorption of astrophysically relevant molecules. *MNRAS*, **354**(4), 1133–1140.

Compiègne, M., Abergel, A., Verstraete, L., & Habart, E. (2008). Dust processing in photodissociation regions. Mid-IR emission modelling. *A&A*, **491**, 797–807.

Creighan, S. C., Perry, J. S. A., & Price, S. D. (2006). The rovibrational distribution of $H_2$ and HD formed on a graphite surface at 15–50 K. *J. Chem. Phys.*, **124**(11), 114701.

Cuppen, H. M. & Herbst, E. (2007). Simulation of the Formation and Morphology of Ice Mantles on Interstellar Grains. *ApJ*, **668**, 294–309.

Dartois, E., Schutte, W., Geballe, T. R., Demyk, K., Ehrenfreund, P., & D'Hendecourt, L. (1999). Methanol: The second most abundant ice species towards the high-mass protostars RAFGL7009S and W 33A. *A&A*, **342**, L32–L35.

Demyk, K., Dartois, E., D'Hendecourt, L., Jourdain de Muizon, M., Heras, A. M., & Breitfellner, M. (1998). Laboratory identification of the 4.62mu M solid state absorption band in the ISO-SWS spectrum of RAFGL 7009S. *A&A*, **339**, 553–560.

Devlin, J. & Buch, V. (1995). Surface of ice as viewed from combined spectroscopic and computer modeling studies. *J. Phys. Chem.*, **99**, 16534–16548.

Dohnalek, Z., Kimmel, G. A., Ayotte, P., Smith, R. S., & Kay, B. D. (2003). The deposition angle-dependent density of amorphous solid water films. *J. Chem. Phys.*, **118**(1), 364–372.

Draine, B. T. (2003). Interstellar Dust Grains. *ARA&A*, **41**, 241–289.

Duley, W. W. & Williams, D. A. (1986). The formation of interstellar H2 on amorphous silicate grains. *MNRAS*, **223**, 177–182.

Duley, W. W. & Williams, D. A. (1993). The formation of H2 on interstellar dust. *MNRAS*, **260**, 37–42.

Engquist, I., Lundstroem, I., & Liedberg, B. (1995). Temperature-programmed desorption and infrared studies of $D_2$2O ice on self-assembled alkanethiolate monolayers: influence of substrate wettability. *J. Phys. Chem.*, **99**, 12257.

Field, D. (2000). $H_2$ formation in space: a negative ion route? *A&A*, **362**, 774–779.

Flower, D. (2007). *Molecular Collisions in the Interstellar Eedium.* Cambridge University Press. ISBN13: 978-0-521-84483-3.

Gerakines, P. A., Whittet, D. C. B., Ehrenfreund, P., Boogert, A. C. A., Tielens, A. G. G. M., Schutte, W. A., Chiar, J. E., van Dishoeck, E. F., Prusti, T., Helmich, F. P., & de Graauw, T. (1999). Observations of Solid Carbon Dioxide in Molecular Clouds with the Infrared Space Observatory. *ApJ*, **522**, 357–377.

Gibb, E. L. & Whittet, D. C. B. (2002). The 6 Micron Feature in Protostars: Evidence for Organic Refractory Material. *ApJ*, **566**, L113–L116.

Gibb, E. L., Whittet, D. C. B., Schutte, W. A., Boogert, A. C. A., Chiar, J. E., Ehrenfreund, P., Gerakines, P. A., Keane, J. V., Tielens, A. G. G. M., van Dishoeck, E. F., & Kerkhof, O. (2000). An Inventory of Interstellar Ices toward the Embedded Protostar W33A. *ApJ*, **536**, 347–356.

Gibb, E. L., Whittet, D. C. B., Boogert, A. C. A., & Tielens, A. G. G. M. (2004). Interstellar Ice: The Infrared Space Observatory Legacy. *ApJS*, **151**, 35–73.

Gould, R. J. & Salpeter, E. E. (1963). The Interstellar Abundance of the Hydrogen Molecule. I. Basic Processes. *ApJ*, **138**, 393–+.

Govers, T. R. (2005). Recombination of atomic hydrogen physisorbed on low-temperature surfaces. http://hal.ccsd.cnrs.fr/ccsd-00004273/en/.

Govers, T. R., Mattera, L., & Scoles, G. (1980). Molecular beam experiments on the sticking and accommodation of molecular hydrogen on a low-temperature substrate. *J. Chem. Phys.*, **72**(10), 5446–5455.

Guillot, B. & Guissani, Y. (2003). Polyamorphism in low temperature water: A simulation study. *J. Chem. Phys.*, **119**(22), 11740–11752.

Guillot, B. & Guissani, Y. (2004). Investigation of vapor-deposited amorphous ice and irradiated ice by molecular dynamics simulation. *J. Chem. Phys.*, **120**(9), 4366–4382.

Hixson, H. G., Wojcik, M. J., Devlin, M. S., Devlin, J. P., & Buch, V. (1992). Experimental and simulated vibrational spectra of $H_2$ absorbed in amorphous ice: Surface structures, energetics, and relaxations. *J. Chem. Phys.*, **97**(2), 753–767.

Hollenbach, D. & Salpeter, E. E. (1970). Surface Adsorption of Light Gas Atoms. *J. Chem. Phys.*, **53**(1), 79–86.

Hollenbach, D. & Salpeter, E. E. (1971). Surface Recombination of Hydrogen Molecules. *ApJ*, **163**, 155–+.

Hornekær, L., Baurichter, A., Petrunin, V. V., Field, D., & Luntz, A. C. (2003). Importance of Surface Morphology in Interstellar $H_2$ Formation. *Science*, **302**(5652), 1943–1946.

Hornekær, L., Baurichter, A., Petrunin, V. V., Luntz, A. C., Kay, B. D., & Al-Halabi, A. (2005). Influence of surface morphology on $D_2$ desorption kinetics from amorphous solid water. *J. Chem. Phys.*, **122**(12), 124701.

Hornekaer, L., Sljivancanin, Z., Xu, W., Otero, R., Rauls, E., Stensgaard, I., Laegsgaard, E., Hammer, B., & Besenbacher, F. (2006). Metastable Structures and Recombination Pathways for Atomic Hydrogen on the Graphite (0001) Surface. *Physical Review Letters*, **96**(15), 156104.

Ioppolo, S., Cuppen, H. M., Romanzin, C., van Dishoeck, E. F., & Linnartz, H. (2008). Laboratory evidence for efficient water formation in interstellar ices. *ApJ*, **686**.

Jenniskens, P. & Blake, D. F. (1994). Structural Transitions in Amorphous Water Ice and Astrophysical Implications. *Science*, **265**, 753–756.

Jenniskens, P., Blake, D. F., Wilson, M. A., & Pohorille, A. (1995). High-Density Amorphous Ice, the Frost on Interstellar Grains. *ApJ*, **455**, 389.

Joblin, C. (2004). PAHs in the Interstellar Carbon Cycle: The Experimental View of PIRENEA. In S. Pfalzner, C. Kramer, C. Staubmeier, and A. Heithausen, editors, *The Dense Interstellar Medium in Galaxies*, pages 517–+.

Jones, A. P. (2001). Interstellar and circumstellar grain formation and survival. *Royal Society of London Philosophical Transactions Series A*, **359**, 1961–+.

Jura, M. (1975). Interstellar clouds containing optically thin $H_2$. *ApJ*, **197**, 575–580.

Katz, N., Furman, I., Biham, O., Pirronello, V., & Vidali, G. (1999). Molecular Hydrogen Formation on Astrophysically Relevant Surfaces. *ApJ*, **522**, 305–312.

Kimmel, G. A., Stevenson, K. P., Dohnalek, Z., Smith, R. S., & Kay, B. D. (2001a). Control of amorphous solid water morphology using molecular beams. I.) Experimental results. *J. Chem. Phys.*, **114**(12), 5284–5294.

Kimmel, G. A., Dohnalek, Z., Stevenson, K. P., Smith, R. S., & Kay, B. D. (2001b). Control of amorphous solid water morphology using molecular beams. II.) Ballistic deposition simulations. *J. Chem. Phys.*, **114**(12), 5295–5303.

Kimmel, G. A., Dohnálek, Z., Stevenson, K. P., Smith, R. S., & Kay, B. D. (2001). Control of amorphous solid water morphology using molecular beams. II. Ballistic deposition simulations. *J. Chem. Phys.*, **114**, 5295–5303.

King, D. A. & Wells, M. G. (1972). Molecular beam investigation of adsorption kinetics on bulk metal targets: Nitrogen on tungsten. *Surface Science*, **29**, 454–482.

Koch, N. & Steffens, E. (1999). High intensity source for cold atomic hydrogen and deuterium beams. *Review of Scientific Instruments*, **70**, 1631–1639.

Laffon, C., Lacombe, S., Bournel, F., & Parent, P. (2006). Radiation effects in water ice: A near-edge x-ray absorption fine structure study. *The Journal of Chemical Physics*, **125**(20), 204714.

Langel, W., Fleger, H. W., & Knœzinger, E. (1994). Structure and morphology of gas phase deposited ice. *Ber. Bunsengesch. Phys. Chem.*, **98**, 81–91.

Laufer, D., Kochavi, E., & Bar-Nun, A. (1987). Structure and dynamics of amorphous water ice. *Phys. Rev. B*, **36**(17), 9219–9227.

Leitch-Devlin, M. A. & Williams, D. A. (1985). Sticking coefficients for atoms and molecules at the surfaces of interstellar dust grains. *MNRAS*, **213**, 295–306.

Lequeux, J. (2005). *The interstellar medium. Translation from the French language edition of: Le Milieu Interstellaire by James Lequeux, EDP Sciences, 2003 Edited by J. Lequeux. Astronomy and astrophysics library, Berlin: Springer, 2005.*

L'vov, B. V. (2007). *Thermal Decomposition of Solids and Melts New Thermochemical Approach to the Mechanism, Kinetics and Methodology Series: Hot Topics in Thermal Analysis and Calorimetry , Vol. 7.* Springer.

Malmasson, D. (1994). *Utilisation d'un Laser VUV en Spectroscopie Moléculaire à Haute Résolution. Application à CO et $H_2$.* Ph.D. thesis, Laboratoire Atomes et Molécules en Astrophysique, Observatoire de Paris-Meudon.

Manicò, G., Ragunì, G., Pirronello, V., Roser, J. E., & Vidali, G. (2001). Laboratory Measurements of Molecular Hydrogen Formation on Amorphous Water Ice. *ApJ*, **548**, L253–L256.

Martin, C., Manca, C., & Roubin, P. (2002a). Adsorption of small molecules on amorphous ice: volumetric and FTIR isotherm co-measurements: Part I. Different probe molecules. *Surface Science*, **502-503**, 275–279.

Martin, C., Manca, C., & Roubin, P. (2002b). Adsorption of small molecules on amorphous ice: volumetric and FTIR isotherm co-measurements: Part II. The case of CO. *Surface Science*, **502-503**, 280–284.

Masuda, K., Takahashi, J., & Mukai, T. (1998). Sticking probability and mobility of a hydrogen atom on icy mantle of dust grains. *A&A*, **330**, 773–781.

Matar, E., Congiu, E., Dulieu, F., Momeni, A., & Lemaire, J. L. (2008). Mobility of D atoms on porous amorphous water ice surfaces under interstellar conditions. *A&A*, **492**, L17–L20.

Mayer, E. & Pletzer, R. (1986). Astrophysical implications of amorphous ice / a microporous solid. *Nature*, **319**, 298–301.

Mennella, V. (2008a). Activation of the 3.47 $\mu$m Band by H Atom Irradiation of Carbon Grains Covered with a Water Ice Layer at 12 K. *ApJ*, **682**, L101–L104.

Mennella, V. (2008b). HD Formation by Abstraction of H/D Chemisorbed in Carbon Grains with D/H Atoms under Simulated Interstellar Conditions. *ApJ*, **684**, L25–L28.

Michelsen, H. A. & Auerbach, D. J. (1991). A critical examination of data on the dissociative adsorption and associative desorption of hydrogen at copper surfaces. *J. Chem. Phys.*, **94**, 7502–7520.

Miyauchi, N., Hidaka, H., Chigai, T., Nagaoka, A., Watanabe, N., & Kouchi, A. (2008). Formation of hydrogen peroxide and water from the reaction of cold hydrogen atoms with solid oxygen at 10K. *Chem. Phys. Letters*, **456**, 27–30.

Molster, F. J., Yamamura, I., Waters, L. B. F. M., Tielens, A. G. G. M., de Graauw, T., de Jong, T., de Koter, A., Malfait, K., van den Ancker, M. E., Van Winckel, H., Voors, R. H. M., & Waelkens, C. (1999). Low-temperature crystallization of silicate dust in circumstellar disks. *Nature*, **401**, 563–+.

Morisset, S., Aguillon, F., Sizun, M., & Sidis, V. (2005). Wave-packet study of $H_2$ formation on a graphite surface through the Langmuir-Hinshelwood mechanism. *J. Chem. Phys.*, **122**, 4702.

Narten, A. H., Venkatesh, C. G., & Rice, S. A. (1976). Diffraction pattern and structure of amorphous solid water at 10 and 77 K. *J. Chem. Phys.*, **64**, 1106–1121.

Notesco, G. & Bar-Nun, A. (1997). Trapping of methanol, hydrogen cyanide, and n-hexane in water ice, above its transformation temperature to the crystalline form. *Icarus*, **126**, 336–341.

Palla, F., Salpeter, E. E., & Stahler, S. W. (1983). Primordial star formation - The role of molecular hydrogen. *ApJ*, **271**, 632–641.

Palumbo, M. E., Geballe, T. R., & Tielens, A. G. G. M. (1997). Solid Carbonyl Sulfide (OCS) in Dense Molecular Clouds. *ApJ*, **479**, 839–+.

Parent, P., Laffon, C., Mangeney, C., Bournel, F., & Tronc, M. (2002). Structure of the water ice surface studied by X-ray absorption spectroscopy at the O K-edge. *J. Chem. Phys.*, **117**(23), 10842–10851.

Perets, H. B., Biham, O., Manicó, G., Pirronello, V., Roser, J., Swords, S., & Vidali, G. (2005). Molecular Hydrogen Formation on Ice Under Interstellar Conditions. *ApJ*, **627**, 850–860.

Perry, J. S. A. & Price, S. D. (2003). Detection of rovibrationally excited $H_2$ formed through the heterogeneous recombination of H atoms on a cold HOPG surface. *Ap&SS*, **285**, 769–776.

Petrenko, V. F. & Whitworth, R. W. (2002). *Physics of ice*. Oxford University Press. ISBN13: 9780198518945.

Pirronello, V., Biham, O., Liu, C., Shen, L., & Vidali, G. (1997a). Efficiency of Molecular Hydrogen Formation on Silicates. *ApJ*, **483**, L131+.

Pirronello, V., Liu, C., Shen, L., & Vidali, G. (1997b). Laboratory Synthesis of Molecular Hydrogen on Surfaces of Astrophysical Interest. *ApJ*, **475**, L69+.

Pirronello, V., Liu, C., Roser, J. E., & Vidali, G. (1999). Measurements of molecular hydrogen formation on carbonaceous grains. *A&A*, **344**, 681–686.

Pletzer, R. & Mayer, E. (1989). Type I isotherms for $N_2$ adsorption on vapor deposited amorphous solid water. *J. Chem. Phys.*, **90**(9), 5207–5208.

Pozgainer, G., Windholz, L., & Winkler, A. (1994). Rovibrational state-specific detection of desorbing hydrogen molecules using multiphoton ionization (REMPI) . *Measurement Science and Technology*, **5**, 947–953.

Redhead, P. A. (1962). Thermal desorption of gases. *Vacuum*, **12**, 203–211.

Rinnen, K.-D., Buntine, M. A., Kliner, D. A. V., Zare, R. N., & Huo, W. M. (1991). Quantitative determination of $H_2$, HD, and $D_2$ internal-state distributions by (2+1) resonance-enhanced multiphoton ionization. *Journal of Chemical Physics*, **95**, 214–225.

Roser, J. E., Manicò, G., Pirronello, V., & Vidali, G. (2002). Formation of Molecular Hydrogen on Amorphous Water Ice: Influence of Morphology and Ultraviolet Exposure. *ApJ*, **581**, 276–284.

Roser, J. E., Swords, S., Vidali, G., Manicò, G., & Pirronello, V. (2003). Measurement of the Kinetic Energy of Hydrogen Molecules Desorbing from Amorphous Water Ice. *ApJ*, **596**, L55–L58.

Roueff, E., Abgrall, H., Liu, X., & Shemansky, D. (2000). Radiative and Electronic Excitation of Lyman and Werner Transitions in $H_2$. In F. Combes and G. Pineau Des Forets, editors, *Molecular hydrogen in space*, page 13.

Rowland, B., Fisher, M., & Devlin, J. P. (1991). Probing icy surfaces with the dangling-OH-mode absorption: Large ice clusters and microporous amorphous ice. *J. Chem. Phys.*, **95**(2), 1378–1384.

Schutte, A., Bassi, D., Tommasini, F., Turelli, A., Scoles, G., & Hermans, L. J. F. (1976). Recombination of atomic hydrogen on low temperature surfaces. *J. Chem. Phys.*, **64**, 4135–4142.

Schutte, W. A., Boogert, A. C. A., Tielens, A. G. G. M., Whittet, D. C. B., Gerakines, P. A., Chiar, J. E., Ehrenfreund, P., Greenberg, J. M., van Dishoeck, E. F., & de Graauw, T. (1999). Weak ice absorption features at 7.24 and 7.41 MU M in the spectrum of the obscured young stellar object W 33A. *A&A*, **343**, 966–976.

Sha, X., Jackson, B., & Lemoine, D. (2002). Quantum studies of Eley-Rideal reactions between H atoms on a graphite surface. *J. Chem. Phys.*, **116**, 7158–7169.

Sha, X., Jackson, B., Lemoine, D., & Lepetit, B. (2005). Quantum studies of H atom trapping on a graphite surface. *J. Chem. Phys.*, **122**, 4709–+.

Shull, J. M., Tumlinson, J., Jenkins, E. B., Moos, H. W., Rachford, B. L., Savage, B. D., Sembach, K. R., Snow, T. P., Sonneborn, G., York, D. G., Blair, W. P., Green, J. C., Friedman, S. D., & Sahnow, D. J. (2000). Far Ultraviolet Spectroscopic Explorer Observations of Diffuse Interstellar Molecular Hydrogen. *ApJ*, **538**, L73–L76.

Silvera, I. F. (1980). The solid molecular hydrogens in the condensed phase: Fundamentals and static properties. *Reviews of Modern Physics*, **52**, 393–452.

Smith, R., Huang, C., & Kay, B. (1997). Evidence for Molecular Translational Diffusion during the Crystallization of Amorphous Solid Water. *J. Phys. Chem. B*, **101**(32), 6123–6126.

Smoluchowski, R. (1981). Rate of $H_2$ formation on amorphous grains. *Ap&SS*, **75**, 353–363.

Spitzer, L., Drake, J. F., Jenkins, E. B., Morton, D. C., Rogerson, J. B., & York, D. G. (1973). Spectrophotometric Results from the Copernicus Satellite.IV. Molecular Hydrogen in Interstellar Space. *ApJ*, **181**, L116+.

Stahler, S. W. & Palla, F. (2004). *The Formation of Stars.* WILEY-VCH Verlag GmbH & Co. KGaA,Weinheim. ISBN: 3-527-40559-3.

Takahashi, J., Masuda, K., & Nagaoka, M. (1999a). Product Energy Distribution of Molecular Hydrogen Formed on Icy Mantles of Interstellar Dust. *ApJ*, **520**, 724–731.

Takahashi, J., Masuda, K., & Nagaoka, M. (1999b). The formation mechanism of molecular hydrogen on icy mantles of interstellar dust. *MNRAS*, **306**, 22–30.

Tielens, A. G. G. M. (2005). *The Physics and Chemistry of the Interstellar Medium.* pp. . ISBN 0521826349. Cambridge, UK: Cambridge University Press, 2005.

Tielens, A. G. G. M. & Hagen, W. (1982). Model calculations of the molecular composition of interstellar grain mantles. *A&A*, **114**, 245–260.

Tiné, S., Williams, D. A., Clary, D. C., Farebrother, A. J., Fisher, A. J., Meijer, A. J. H. M., Rawlings, J. M. C., & Davis, C. J. (2003). Observational Indicators of Formation Excitation of $H_2$. *Ap&SS*, **288**, 377–389.

Tissue, B. M. (2000). The Chemistry Hypermedia Project: Quadrupole Mass Spectrometry. http://www.chem.vt.edu/chem-ed/ms/quadrupo.html.

Toennies, J. P., Welz, W., & Wolf, G. (1979). Molecular beam scattering studies of orbiting resonances and the determination of van der Waals potentials for H-Ne, Ar, Kr, and Xe and for $H_2$-Ar, Kr, and Xe. *Journal of Chemical Physics*, **71**, 614–642.

Tully, J. C. (1981). Summary Abstract: Atomic and molecular scattering at surfaces. *Journal of Vacuum Science Technology*, **18**, 427–+.

Usuda, T. (1996). *No title found.* Ph.D. thesis, Univ. Tokyo, (1996).

van Dishoeck, E. F., Dartois, E., Pontoppidan, K. M., Thi, W. F., D'Hendecourt, L., Boogert, A. C. A., Fraser, H. J., Schutte, W. A., & Tielens, A. G. G. M. (2003). Origin and Evolution of Ices in Star-Forming Regions: A VLT-ISAAC 3-5 microns Spectroscopic Survey. *The Messenger*, **113**, 49–55.

Vichnevetski, E., Bass, A. D., & Sanche, L. (2000). Sample morphology and porosity in electron stimulated desorption: $N_2$* from $N_2$ adsorbed onto nanoscale ice films. *J. Chem. Phys.*, **113**, 3874–3881.

Vidali, G. (1991). Potentials of physical adsorption. *Surf. Sci. Re.*, **12**, 135–181.

Vidali, G., Roser, J. E., Manicò, G., & Pirronello, V. (2004). Experimental study of the formation of molecular hydrogen and carbon dioxide on dust grain analogues. *Advances in Space Research*, **33**, 6–13.

Vidali, G., Pirronello, V., Li, L., Roser, J., Manico, G., Mehl, R., Lederhendler, A., Perets, H. B., Brucato, J. R., & Biham, O. (2007). Molecular Hydrogen Formation on Low Temperature Surfaces in Temperature Programmed Desorption Experiments. *J. Phys. Chem. A*, **111**, 12611–12619.

Walch, S. P., McMichael Rohlfing, C., Melius, C. F., & Bauschlicher, Jr., C. W. (1988). Theoretical characterization of the minimum energy path for the reaction H+$O_2$ –$HO_2^*$ –HO+O. *J. Chem. Phys.*, **88**, 6273–6281.

Whittet, D. C. B., Pendleton, Y. J., Gibb, E. L., Boogert, A. C. A., Chiar, J. E., & Nummelin, A. (2001). Observational Constraints on the Abundance and Evolution of "XCN" in Interstellar Grain Mantles. *ApJ*, **550**, 793–798.

Williams, D. & Herbst, E. (2002). It's a dusty Universe: surface science in space. *Surface Science*, **500**, 823–837.

Willner, S. P., Gillett, F. C., Herter, T. L., Jones, B., Krassner, J., Merrill, K. M., Pipher, J. L., Puetter, R. C., Rudy, R. J., Russell, R. W., & Soifer, B. T. (1982). Infrared spectra of protostars - Composition of the dust shells. *ApJ*, **253**, 174–187.

Yabushita, A., Hama, T., Iida, D., & Kawasaki, M. (2008a). Hydrogen peroxide formation following the vacuum ultraviolet photodissociation of water ice films at 90 K. *J. Chem. Phys.*, **129**(1), 014709–+.

Yabushita, A., Hama, T., Iida, D., Kawanaka, N., Kawasaki, M., Watanabe, N., Ashfold, M. N. R., & Loock, H.-P. (2008b). Measurements of Energy Partitioning in $H_2$ Formation by Photolysis of Amorphous Water Ice. *ApJ*, **682**, L69–L72.

Yabushita, A., Hama, T., Iida, D., Kawanaka, N., Kawasaki, M., Watanabe, N., Ashfold, M. N. R., & Loock, H.-P. (2008c). Release of hydrogen molecules from the photodissociation of amorphous solid water and polycrystalline ice at 157 and 193 nm. *J. Chem. Phys.*, **129**(4), 044501–+.

# Appendix A

# Publications

**Articles in refereed journals:**

E. Congiu, **E. Matar**, L. E. Kristensen, F. Dulieu, and J. L. Lemaire. "Laboratory evidence for the non-detection of excited nascent $H_2$ in dark clouds."

*Mon. Not. R. Astron. Soc. 297, L96–L100, 2009.*

**E. Matar**, E. Congiu, F. Dulieu, A. Momeni, and J. L. Lemaire. "Mobility of D atoms on porous amorphous water ice surfaces under interstellar conditions."

*Astronomy and Astrophysics, 492, L17L20, 2008.*

L. Amiaud, A. Momeni, F. Dulieu, J. H. Fillion, **E. Matar**,J.-L. Lemaire. "Measurement of the adsorption energy difference between *ortho*- and *aara*-$D_2$ on an amorphous ice surface."

*Physical Review Letters, vol. 100, Issue 5, id. 056101, 2008.*

F. Dulieu, E. Congiu, L. Amiaud, J. H. Fillion, **E. Matar**, A. Momeni, V. Pirronello, and J. L. Lemaire. "Experimental evidence of water formation on interstellar dust grains."

*Submitted to Astronomy and Astrophysics.*

**E. Matar**, F. Dulieu, H. Chaabouni, J.L. Lemaire, and H. Bergeron. "Gas-temperature dependent sticking of atomic and molecular hydrogen on interstellar dust grains."

*In final stage of preparation.*

**Oral contributions to international conferences:**

**E., Matar**, F. Dulieu, E. Congiu, H. Chaabouni, M. Accolla, H. Mokrane, M. Chehrouri, and J. L. Lemaire.
"Laboratory Astrophysics : Formation of hydrogen on interstellar dust grains, an experimental approach."
*First Lebanese Astrophysics Meeting '09: From stars to galaxies, April, 14–17, 2009, Beirut, Lebanon.*

**E. Matar**, F. Dulieu, H. Chaabouni, J.L. Lemaire.
"The sticking of hydrogen molecules on icy interstellar dust grains: Beam temperature dependence."
*Réunion plénière du GDR; May 4–7, 2009, La Londe-les-Maures, France.*

**E. Matar**, E. Congiu, F. Dulieu, A. Momeni, J.-L. Lemaire.
"Mobility of cold D atoms on icy interstellar dust grains."
*Heterogeneous Chemical Processes in the Astronomical Environment, June 15 - 17, 2009, UCL, London.*

**Seminar:**
"Mobilité des atomes de D froids sur les surfaces de glace des grains du milieu interstellaire." *Seminaire "Cœurs Denses", Observatoire de Paris-Meudon, Paris, June 23, 2009.*

Mon. Not. R. Astron. Soc. **397,** L96–L100 (2009) doi:10.1111/j.1745-3933.2009.00692.x

# Laboratory evidence for the non-detection of excited nascent $H_2$ in dark clouds

E. Congiu,★ E. Matar, L. E. Kristensen,† F. Dulieu and J. L. Lemaire
*Université de Cergy-Pontoise & Observatoire de Paris, LERMA/LAMAp, UMR 8112 du CNRS, 95000 Cergy-Pontoise, France*

Accepted 2009 May 22. Received 2009 May 21; in original form 2009 February 23

**ABSTRACT**

There has always been a great deal of interest in the formation of $H_2$ as well as in the binding energy released upon its formation on the surface of dust grains. The present work aims at collecting experimental evidence for how the bond energy budget of $H_2$ is distributed between the reaction site and the internal energy of the molecule. So far, the non-detection of excited nascent $H_2$ in dense quiescent clouds could be a sign that either predictions of emission line intensities are not correct or the de-excitation of the newly formed molecules proceeds rapidly on the grain surface itself. In this Letter, we present experimental evidence that interstellar molecular hydrogen is formed and then rapidly de-excited on the surface of porous water ice mantles. In addition, although we detect ro-vibrationally excited nascent molecules desorbing from a bare non-porous (compact) water ice film, we demonstrate that the amount of excited nascent hydrogen molecules is significantly reduced no matter the morphology of the water ice substrate at 10 K (both on non-porous and on porous water ice) in a regime of high molecular coverage as is the case in dark molecular clouds.

**Key words:** methods: laboratory – ISM: clouds – dust, extinction – ISM: molecules.

## 1 INTRODUCTION

The formation of molecular hydrogen ($H_2$) in the interstellar medium (ISM) is considered one of the most important chemical reactions occurring in space. $H_2$ is ubiquitous, it is by far the most abundant molecular species in the Universe and is a major contributor to the cooling of astrophysical media. In addition, this simple molecule is also responsible for initiating the interstellar chemistry leading to the large and various inventory of molecules that have been observed so far (Dalgarno 2000).

Since gas phase routes for the conversion of hydrogen atoms to molecules are too inefficient to account for the high abundances that are observed, it has been long assumed (Gould & Salpeter 1963), and now confirmed by many laboratory experiments (e.g. Vidali et al. 2006, and references therein), that molecular hydrogen is formed efficiently in surface reactions on cosmic dust grains. The two main mechanisms invoked for surface catalysis are: the Langmuir–Hinshelwood (L–H) mechanism, in which $H_2$ forms in a H-atom diffusion process, and the Eley–Rideal (E–R) mechanism, or 'prompt' mechanism, in which an impinging H-atom reacts directly with an adsorbed H-atom (Duley 1996).

Of major concern for this work, is the 4.48 eV released upon formation of the $H_2$ molecule on grain surfaces and how the binding energy is distributed between the reaction site and the translational and internal energy in the molecule. Several theoretical and experimental works have been carried out on this subject. To cite just a few examples, the formation of $H_2$ via the E–R process on graphite surfaces at 10 K was studied with purely quantum mechanical calculations (Farebrother et al. 2000; Meijer et al. 2001; Morisset et al. 2004a), semiclassical quantum molecular dynamics (Rutigliano 2001) and classical and quasi-classical trajectory calculations (Parneix & Brechignac 1998). These studies generally find the product $H_2$ in significantly excited $v$–$J$ states. Quantum dynamics of the L–H mechanism on graphite was studied by Morisset et al. (2004b, 2005). They predict even greater vibrational energy of the nascent molecule. A very recent computational study by Goumans et al. (2009) on an olivine surface seems to suggest, however, that nascent $H_2$ formed from chemisorbed H-atoms is considerably less ro-vibrationally excited than when it is formed on graphite. As to the case of interest here, hydrogen formation on water ice, Takahashi, Masuda & Nagaoka (1999) made a detailed calculation of $H_2$ formation on amorphous ice using a classical description in a molecular dynamics formulation. They found most of the recombination energy distributed in vibration (70–80 per cent) of the product $H_2$ while only 5 per cent of the H–H bond energy was deposited in the ice substrate.

Experiments performed on non-porous surfaces show that molecular hydrogen is formed in a ro-vibrational excited state both on graphite (Latimer, Islam & Price 2008) and on amorphous solid water (ASW) ice (Amiaud et al. 2007). As for the formation of $H_2$ on porous substrates, Roser et al. (2003) and Hornekær et al. (2003)

★E-mail: econgiu@u-cergy.fr
†Present address: Leiden Observatory, Niels Bohrweg 2, NL-2333 CA Leiden, the Netherlands.

© 2009 The Authors. Journal compilation © 2009 RAS

A&A 492, L17–L20 (2008)
DOI: 10.1051/0004-6361:200810434
© ESO 2008

Astronomy & Astrophysics

Letter to the Editor

# Mobility of D atoms on porous amorphous water ice surfaces under interstellar conditions

E. Matar, E. Congiu, F. Dulieu, A. Momeni*, and J. L. Lemaire

Université de Cergy-Pontoise & Observatoire de Paris, LERMA, UMR 8112 du CNRS, 95000 Cergy-Pontoise, France
e-mail: Elie.Matar@u-cergy.fr

Received 20 June 2008 / Accepted 23 October 2008

**ABSTRACT**

*Aims.* The mobility of H atoms on the surface of interstellar dust grains at low temperature is still a matter of debate. In dense clouds, the hydrogenation of adsorbed species (i.e., CO), as well as the subsequent deuteration of the accreted molecules depend on the mobility of H atoms on water ice. Astrochemical models widely assume that H atoms are mobile on the surface of dust grains even if controversy still exists. We present here direct experimental evidence of the mobility of H atoms on porous water ice surfaces at 10 K.
*Methods.* In a UHV chamber, $O_2$ is deposited on a porous amorphous water ice substrate. Then D atoms are deposited onto the surface held at 10 K. Temperature-Programmed Desorption (TPD) is used and desorptions of $O_2$ and $D_2$ are simultaneously monitored.
*Results.* We find that the amount of $O_2$ that desorbs during the TPD diminishes if we increase the deposition time of D atoms. $O_2$ is thus destroyed by D atoms even though these molecules have previously diffused inside the pores of thick water ice. Our results can be easily interpreted if D is mobile at 10 K on the water ice surface. A simple rate equation model fits our experimental data and best fit curves were obtained for a D atom diffusion barrier of 22 ± 2 meV. Therefore hydrogenation can take place efficiently on interstellar dust grains. These experimental results are consistent with most calculations and validate the hypothesis used in several models.

**Key words.** astrochemistry – ISM: atoms – dust, extinction – methods: laboratory

## 1. Introduction

Among the numerous molecules detected in different astrophysical environments, a large fraction is composed of hydrogenated species (Chang et al. 2007, and references therein). It has been established that dust grains play a major role in the hydrogenation of compounds (Herbst & Klemperer 1973; Smith et al. 2006). In the dense interstellar medium where most of the hydrogenated species have been detected (especially during the star formation stage, Tegmark et al. 1997; Cazaux & Tielens 2004; Cazaux & Spaans 2004), grains are covered in a molecular mantle mainly composed of water ice. In all the theoretical chemical models that describe the hydrogenation of compounds on grains (Tielens & Hagen 1982; Cuppen & Herbst 2007), mobility of hydrogen is hypothesised, though some calculations on amorphous water surfaces (Smoluchowski 1981) and modelling of experimental data (Perets et al. 2005) rule out such a mobility. On the other hand, other calculations (Buch & Zhang 1991; Masuda et al. 1998) and interpretations of experimental data (Hornekær et al. 2003) validate the hypothesis that H is mobile at 10 K, a temperature supposed to be close to that of dust grains in interstellar dense clouds where hydrogenation takes place. We have already demonstrated that D atoms are mobile at 10 K (in our experiment time scale) on non-porous amorphous solid water (np-ASW) ices (Amiaud et al. 2007), but the porosity and the roughness of the water ice films grown at low temperatures (10 K) may considerably lower the D atom mobility.

Yet the debate upon the mobility of hydrogen atoms is not closed, and much controversy exists regarding the interpretation of experiments (Vidali et al. 2006; Dulieu 2006). If one considers only the latest estimated value of 51 meV (Perets et al. 2005) for the diffusion energy barrier of H on porous amorphous solid water (p-ASW) ice, the hopping time between two adjacent adsorption sites is about 10 million years at 10 K. In such a context, no hydrogenation chemistry can occur on icy mantles of dust grains on a reasonable time scale. Hence, observational evidence of hydrogenated and deuterated species is a good argument for an experimental investigation of the mobility of H-atoms.

The aim of this paper is to provide new experimental evidence that directly addresses – without the prism of a sophisticated model – the question of hydrogen mobility on p-ASW ice at 10 K. By using $O_2$ as a tracer of D mobility we present a set of experiments that are straightforward to interpret if D is mobile on the surface of porous amorphous water ice, as is expected from almost all calculations and included in several astrochemical models. In Sect. 2 we briefly describe the experimental set-up and procedures. In Sect. 3 we present our experimental results and explain them assuming that D is mobile on p-ASW ice at 10 K. In Sect. 4, we describe a simple rate equation model that we used to fit our experimental results. In Sect. 5 we discuss other interpretations before concluding.

## 2. Experimental section

The FORmation of MOLecules in the InterStellar Medium (FORMOLISM) experimental set-up has been developed with the purpose of studying the reaction and interaction of atoms and molecules on surfaces simulating dust grains under interstellar conditions (the relevance of substrate, low density, and very low temperatures ∼10 K). FORMOLISM is composed of an ultra-high vacuum chamber with a base pressure of $\sim 10^{-10}$ mbar, a

* *Present address*: LCAM, Université Paris-Sud, Orsay, France.

PRL **100,** 056101 (2008) PHYSICAL REVIEW LETTERS week ending 8 FEBRUARY 2008

# Measurement of the Adsorption Energy Difference between *Ortho*- and *Para*-$D_2$ on an Amorphous Ice Surface

L. Amiaud,* A. Momeni, F. Dulieu,† J. H. Fillion,‡ E. Matar, and J.-L. Lemaire

*LERMA, UMR8112 du CNRS, de l'Observatoire de Paris et de l'Université de Cergy Pontoise, 5 mail Gay Lussac, 95031 Cergy Pontoise Cedex, France*

(Received 16 February 2007; published 4 February 2008)

Molecular hydrogen interaction on water ice surfaces is a major process taking place in interstellar dense clouds. By coupling laser detection and classical thermal desorption spectroscopy, it is possible to study the effect of rotation of $D_2$ on adsorption on amorphous solid water ice surfaces. The desorption profiles of ortho- and para-$D_2$ are different. This difference is due to a shift in the adsorption energy distribution of the two lowest rotational states. Molecules in $J'' = 1$ rotational state are on average more strongly bound to the ice surface than those in $J'' = 0$ rotational state. This energy difference is estimated to be $1.4 \pm 0.3$ meV. This value is in agreement with previous calculation and interpretation. The nonspherical wave function $J'' = 1$ has an interaction with the asymmetric part of the adsorption potential and contributes positively in the binding energy.

DOI: 10.1103/PhysRevLett.100.056101 PACS numbers: 68.43.Mn, 68.43.Vx, 98.38.Bn, 98.58.Bz

Because of the nuclear spin of its atomic constituents, two states of $H_2$ exist in the lowest electronic state: *para*-$H_2$ with even $J$ rotational numbers, and *ortho*-$H_2$ with odd $J$ rotational numbers. In the dark clouds of the interstellar medium, the dust grains are covered with ice, mainly composed of water, which is the most abundant molecule in the solid phase [1]. In these environments, molecular hydrogen is the most abundant species. The interaction between molecular hydrogen and a water ice surface is therefore a major process [2–5] in these dense interstellar regions. The ortho- to para- $(o/p)$ ratio of the hydrogen molecules has great consequences on the subsequent chemistry, particularly on the deuteration of species [6]. The $o/p$ conversion on interstellar grains has been discussed in the context of photodissociation regions [7]. The adsorption energy of the molecules, and therefore of the ortho- and para- states, can play an important role in the coverage of the interstellar dust grains [8].

The difference in adsorption energy on some cold surfaces ($TiO_2 \ldots$) of ortho- and para-$H_2$ states has been known for a long time ([9] and references within). This is the basis for experimental procedures that allow separating ortho-$H_2$ from normal $H_2$. In the case of a water surface, infrared spectroscopy has demonstrated the adsorption of ortho-$H_2$ in preference to para-$H_2$, by observing change in the spectra in time [10]. Computations have been carried out to explain this behavior using $H_2$ water ice cluster interactions [11]. The calculated average difference in the adsorption energy is found to be $\sim$30 K ($\sim$2.6 meV). These authors [11] explain this energy difference from a physical point of view as follows: the wave function of para-$H_2$ ($J = 0$) is approximately spherically symmetric, while the wave function of ortho-$H_2$ ($J = 1$) is similar to the nonspherical hydrogen atom's $p$ function. Therefore para-$H_2$, does not "feel" the anisotropic part of the potential, while ortho-$H_2$, has extra binding energy with respect to para-$H_2$ due to the anisotropic part. Even if in the astrophysical context $H_2$ is much more relevant than $D_2$, this experimental study deals with $D_2$ only, which has been chosen to avoid complications due to the presence on $H_2$ as a main pollutant of UHV chambers. In the case of deuterium, the ortho-$D_2$ has even $J$ rotational numbers, whereas para-$D_2$ has odd ones. At 300 K, the normal $D_2$ $o/p$ ratio is statistically equal to $2/1$. To our knowledge, there is no experimental measurement of such difference in the adsorption energies for molecular hydrogen adsorbed on water ice surfaces despite its high importance for astrophysics. In this Letter we present a new technique coupled to an original analysis in order to measure directly the difference in adsorption energies of the two lowest states of $D_2$. In the first part we present briefly the experimental setup and the technique used (thermal desorption spectroscopy of selected quantum state TDS-SQS). In order to explain the method that will be used to analyze the TDS-SQS profiles, the second part shows the change of the classical TDS profiles when two hydrogen isotopes are present on the surface. We briefly recall the model that has been used to describe this isotopic segregation, based only on an energy shift between two populations. The last part presents the experimental $D_2$ desorption study from amorphous solid water (ASW) ice surface of the $J = 0$, 1, 2 rotational states and the analysis that concludes to an average adsorption energy difference between para- and ortho- states of $1.4 \pm 0.3$ meV.

Our experiments were performed using the FORMOLISM setup. The precise experimental procedures and more details are described in [12]. The setup contains a main UHV chamber. A copper sample thermally controlled between 8 and 800 K, with 0.2 K precision and 1 K absolute accuracy, is covered with the ASW ice sample. The sample is composed of 250 layers of nonporous ASW deposited at 120 K [13] in order to isolate subsequent depositions from the

 © 2008 The American Physical Society

*Astronomy & Astrophysics* manuscript no. Dulieu˙09˙B
July 20, 2009
© ESO 2009

Letter to the Editor

# Experimental evidence for water formation on interstellar dust grains by hydrogen and oxygen atoms

F. Dulieu[1] , L. Amiaud[1,3] , E. Congiu[1], J-H. Fillion[1,4], E. Matar[1], A. Momeni[1,3], V. Pirronello[2], and J. L. Lemaire[1]

[1] LERMA, UMR8112 du CNRS, de l'Observatoire de Paris et de l'Université de Cergy Pontoise, 5 mail Gay Lussac, 95031 Cergy Pontoise Cedex, France
[2] Dipartimento di Metodologie Fisiche e Chimiche, Università di Catania, Viale A. Doria 6, 95125 Catania, Sicily, Italy
[3] Present address: LCAM, Orsay, France
[4] Present address: Université Pierre et Marie Curie - Paris 6, LPMAA, UMR 7092 du CNRS, France

Received XXX; accepted YYY

**Abstract**

*Context.* The synthesis of water is one necessary step in the origin and development of life. It is believed that pristine water is formed and grows on the surface of icy dust grains in dark interstellar clouds. Until now, there has been no experimental evidence whether this scenario is feasible or not on an astrophysically relevant template and by hydrogen and oxygen atom reactions.
*Aims.* We present here the first experimental evidence of water synthesis by such a process on a realistic grain surface analogue in dense clouds, i.e., amorphous water ice.
*Methods.* Atomic beams of oxygen and deuterium are aimed at a porous water ice substrate ($H_2O$) held at 10 K. Products are analyzed by the temperature-programmed desorption technique
*Results.* We observe production of HDO and $D_2O$, indicating that water is formed under conditions of the dense interstellar medium from hydrogen and oxygen atoms. This experiment opens up the field of a little explored complex chemistry that could occur on dust grains, believed to be the site where key processes lead to the molecular diversity and complexity observed in the Universe.

**Key words.** astrochemistry – ISM: molecules – ISM: dust, extinction – methods: laboratory

*Submitted.*

# Gas temperature dependent sticking of $H_2$ on cold amorphous water ice surfaces of interstellar interest

E. Matar,* F. Dulieu, H. Chaabouni, and J. L. Lemaire
*Université de Cergy-Pontoise & Observatoire de Paris, LERMA/LAMAp, UMR 8112 du CNRS, 95000 Cergy-Pontoise, France*

H. Bergeron
*Université Paris-Sud, LCAM, UMR 8625 du CNRS, 91405 Orsay, France*

(Dated: June 24, 2009)

The sticking of molecular hydrogen has been extensively studied theoretically over the years but few experimental works have been carried out. In dense molecular clouds, the presence of molecular hydrogen is of fundamental importance to the evolution of these cosmological objects, since it is a major cooling agent as well as an initiator of the interstellar chemistry leading to the formation of other more complex molecules. In this paper we present experimental data on the dependence of the sticking of molecular hydrogen and deuterium on the gas temperature onto non-porous amorphous solid water (ASW) ice surfaces of interstellar interest. A statistical model was developed by one of us [H.Bergeron] to fit at the same time our experimental results on $H_2$ and $D_2$ and the theoretical ones of V. Buch *et al.* on atomic hydrogen and deuterium [V. Buch and Q. Zhang The Astrophysical Journal, **379**, 647-652, (1991)]. This model highlights a mass-dependence relation between the sticking coefficients of H and D on one hand, and $H_2$ and $D_2$ on the other hand, under a renormalization-dilation transform. The best fit curves of our sticking coefficients of $H_2$ and $D_2$ were obtained with a decaying function: $S(T) = S_0(1 + 2T/T_0)/(1 + T/T_0)^2$ where $S_0 = 0.75$ and $T_0 = 70$ K in the case of $H_2$, $S_0 = 0.82$ and $T_0 = 140$ K in that of $D_2$.

PACS numbers:

*In final stage of preparation.*

# Appendix B

# Resumé français

Parmi les différentes structures de l'univers, existe ce qu'on appelle le milieu interstellaire (MIS). Ce sont les endroits baignés par les gaz et les poussières provenant de l'éjection des couches externes d'étoiles en fin de vie et l'explosion d'autres. Ce mélange de gaz et de poussière co-existe et interagit pour conduire à la formation d'une nouvelle génération d'étoiles et de systèmes solaires comme le notre.

Les grains de poussière sont de petits corps riches en carbone (grains carbonés et PAH), ou oxygène, silicium, fer et magnésium (grains silicatés) comme les grains de sable. Ils ont des tailles variées qui peuvent atteindre quelques $\mu$m en diamètre. Dans les endroits les plus froids et sombres du MIS, ces grains sont couverts d'une couche de glace dont l'eau est le constituant majeur, suivi par CO, $CO_2$, $CH_3OH$ ...

Le gaz interstellaire est constitué de nombreuses espèces, atomiques et moléculaires, parmi lesquelles l'hydrogène est de loin le plus abondant et le plus important. C'est la molécule la plus simple et le constituant principal de trois des quatre molécules les plus essentielles à l'apparition de la vie, l'eau ($H_2O$), le méthane ($CH_4$), l'ammoniaque ($NH_3$) et le monoxyde de carbone (CO). L'hydrogène est principalement sous sa forme atomique dans les milieux diffus et majoritairement moléculaire dans les milieux froids et denses (nuages sombres et coeurs denses).

La physico-chimie du MIS qui mène à la formation de nouvelles molécules, même les plus complexes, peut être divisée en deux classes de réactions: celles qui ont lieu en phase gazeuse et celles qui se produisent sur la surface des grains de poussière interstellaire.

Dans les conditions extrêmes qui dominent le MIS (très basses température et densité, très faible flux), la chimie en phase gazeuse n'est efficace que pour la formation d'un petit nombre de molécules. La majorité des molécules interstellaires détectées jusqu'aujourd'hui, dont l'hydrogène moléculaire, se sont formées à la surface des grains de poussière. Ces derniers jouent le rôle de catalyseur qui aide à évacuer l'excès d'énérgie dégagée lors de

la formation de la molécule. 0 Pour comprendre la réaction de formation de l'hydrogène moléculaire sur les grains de poussière interstellaire, il est nécessaire de bien comprendre l'ensemble des processus physico-chimiques qui conduisent à cette formation.

Ce travail de thèse est une contribution expérimentale à l'étude de l'interaction et de la formation de l'hydrogène moléculaire sur les surfaces de glace d'eau amorphe qui couvrent les grains de poussière dans les nuages denses et sombres du MIS. Dans ce but, en réunissant techniques ultravides, systèmes cryogéniques, jets atomiques et moléculaires et spectrométrie de masse, plusieurs expériences ont été faites en utilisant le dispositif expérimental FORMOLISM (FORmation of MOLecules in the InterStellar Medium). Des modélisations théoriques sont également nécessaires pour interpréter les résultats expérimentaux.

Dans ce travail le collage de $H_2$ et de $D_2$ est étudié en détail et la dépendance du coefficient de collage avec la température et avec la masse du gaz est mesurée et modélisée. Dans les conditions des nuages moléculaires denses (grains couverts de glace et $T_{grain}$=$T_{gaz}$=10 K), on trouve que le collage de $H_2$ est de 74% et celui de $D_2$ de 82%. Une expérience pour mesurer indirectement le coefficient du collage des atomes est décrite et des résultats préliminaires sont présentés.

D'autres expériences mettent en évidence la mobilité des atomes d'hydrogène sur la glace amorphe poreuse à 10 K. Cette mobilité a été longuement sujette à caution et n'a jamais été prouvée expérimentalement jusqu'à aujourd'hui. La barrière de diffusion des atomes H est calculée et trouvée égale à 22±2 meV. Ce résultat concorde avec les calculs théoriques de plusieurs équipes. Cette valeur de barrière de diffusion se traduit par un temps de diffusion d'un site d'adsorption à un site voisin égal à 12 ms.

Un dernier ensemble d'expériences est fait dans le but d'étudier la formation et la désexcitation de $H_2$ sur les glaces d'eau amorphe poreuse et non-poreuse dans les conditions des nuages sombres du MIS. Ces expériences révèlent que plus que 90% de l'énergie dégagée lors de la formation de $H_2$ est transmise à la surface. Cette transmission peut être expliquée par deux phénomènes: (1) la saturation de la surface de glace par les molécules d'hydrogène déjà adsorbées et (2) la porosité de la glace qui aide à retenir plus longtemps les molécules récemment formées. Ces expériences montrent que moins de 10% des molécules sont directement libérées en phase gazeuse dans des états rovibrationnels excités que la glace soit poreuse ou non.

Ce dernier résultat peut expliquer pourquoi les tentatives faites par plusieurs équipes d'astronomes pour observer l'hydrogène moléculaire excité dans les nuages sombres n'ont pas été fructueuses.

## Abstract

The interstellar medium (ISM) is the place surrounding the stars. It is constituted of gas and dust coming from the ejecta of some stars and the explosion of some others.

Interstellar dust grains can be carbonaceous or composed of silicates, iron and magnesium. Over 120 molecular and atomic species are detected so far in the ISM. Molecular hydrogen is the most abundant and by far the most important since it is found in three of four molecules essential for life: water ($H_2O$), methane ($CH_4$), ammonia ($NH_3$) and carbon monoxide (CO).

The physical-chemistry that leads to the formation of molecules and of stars afterwards can be divided in two: the gas phase chemistry and the gas-surface chemistry. In the extreme conditions (very low both temperature and gas density) that exist in some places of the ISM, gas phase reactions are highly inefficient, especially for the formation of molecular hydrogen whose abundance can only be explained by its formation occurring on the surface of dust grains. These grains play the role of catalysts and help evacuating the excess energy released by the molecules formed.

This thesis is mainly an experimental contribution to the study of the interaction and formation of molecular hydrogen on water ice surfaces mimicking the ice mantles that cover dust grains in the dark clouds of the ISM. For this purpose, combining ultra-high vacuum techniques, cryogenic systems, atomic and molecular beams, mass spectrometry as well as theoretical modelling, several experiments is conducted using the FORMOLISM (FORmation of MOLecules in the InterStellar Medium) experimental set-up.

In this thesis work, the sticking of molecular hydrogen and deuterium is studied in detail and the sticking coefficient is found to be highly dependent on the gas temperature and mass. In dark clouds, where grains are covered with ice and $T_{grain}$=$T_{gas}$=10 K, the sticking of $H_2$ is found to be 74% and that of $D_2$ 82%.

Other experiments highlight the mobility of hydrogen atoms on porous water ice at 10 K. This mobility has been questioned for a long time and has never been really proved experimentally. The diffusion barrier of the atoms is found to be equal to 22±2 meV, in agreement with several theoretical calculations. This value is equivalent to a diffusion time of 12 ms from one adsorption site to a neighbour site.

A final set of experiments have been conducted in order to study the formation and de-excitation of nascent hydrogen molecules on porous and non-porous amorphous water ice in the conditions of quiescent dark clouds. These experiments have shown that more than 90% of the formation energy is deposited into the ice in the porous case. This energy transfer can be explained by two phenomena: (1) the saturation coverage of the ice surface by $H_2$, and (2) the porosity of the ice that recaptures the nascent molecule helping it to relax. These experiments show that less than 10% of the newly formed molecules are released in the gas phase in an excited ro-vibrational states both in the porous and the non-porous ice cases. These results may explain why the observations of several teams trying to detect excited molecular hydrogen in dark quiescent clouds were unsuccessful.


(For the **french abstract** please refer to Appendix B)